Winter 12-22-2021

Observation of **Ω** Contribution in the �c1(3872) **→ Π+π**−j/**ψ** Decays

Baasansuren Batsukh

Syracuse University

Abstract

Resonant structure in the dipion mass spectrum produced via $B^+ \to \chi_{c1}(3872)K^+$, $\chi_{c1}(3872) \to J/\psi\pi^+\pi^-$, with $J/\psi \to \mu^+\mu^-$ is analyzed using Run 1 and Run 2 data samples from the LHCb experiment. The spectrum is dominated by $\rho^0 \to \pi^+\pi^-$, but cannot be described by this contribution alone. A significant $\omega \to \pi^+\pi^-$ contribution, interfering with ρ^0, is observed for the first time. This is a more significant observation ($> 7.1\sigma$) of $\chi_{c1}(3872) \to \omega J/\psi$ decays, than previously achieved with $\omega \to \pi^+\pi^-\pi^0$ decays. The relative contribution of ω to the total $\chi_{c1}(3872) \to \pi^+\pi^- J/\psi$ rate is at the level expected from the measured $\chi_{c1}(3872) \to (\omega \to \pi^+\pi^-\pi^0)J/\psi$ rate, if the interference between the ρ^0 and ω amplitudes is neglected, $(1.9 \pm 0.4 \pm 0.3)\%$. The interference enhances the importance of ω contribution by an order of magnitude to $(21.4 \pm 2.3 \pm 2.0)\%$. The results support interpretations of the $\chi_{c1}(3872)$ state as an exotic hadron, since its isospin violating $\rho^0 J/\psi$ decay rate, relative to isospin conserving $\omega J/\psi$ decay, is an order of magnitude larger than expected for an ordinary charmonium state.

Observation of ω contribution in the $\chi_{c1}(3872) \to \pi^+\pi^- J/\psi$ decays

by

Baasansuren Batsukh

B.S., National University of Mongolia, 2015

A DISSERTATION SUBMITTED IN PARTIAL FULFILLMENT
OF THE REQUIREMENTS FOR THE DEGREE OF
DOCTOR OF PHILOSOPHY IN PHYSICS

Syracuse University

December 2021

Acknowledgements

There are a number of people who contributed to this thesis. Foremost, I would like to express my sincere gratitude to professor Tomasz Skwarnicki, my advisor. Since I become his student, he showed me his unwavering support and guided me with great patience when I had difficulties during the physics analysis work. His immense high energy physics knowledge, experience and genuine, caring personality set a standard that I strive to reach.

I also like to thank professor Sheldon Stone. His vast physics analysis and detector construction knowledge make him a great leader of Syracuse University's LHCb group. I also want to extend my thanks to professor Marina Artuso and professor Raymond Mountain. It was great fun to work with them. Professor Marina Artuso was immensely helpful during the silicon sensor study. She was always willing to help when I had questions, and it was easy to communicate with her. Working with professor Raymond Mountain was a delightful experience. His knowledge in detector physics and managing skills made our lab work pleasant, and he was accommodating and open to discussions. Also, thanks to professor Matt Rudolph and professor Steve Blusk for always being approachable.

Many thanks to Mikhail Mikhasenko for providing us with a theoretical model for our dipion mass spectrum analysis. Also, many thanks to Alessandro Pilloni, César Fernánder-Ramirez and Adam Szczepaniak for fruitful discussions on the X(3872) study.

I want to say thank you to my mentor, PhD Orlokh Dorjkhaidav, who sadly passed away. Special thanks to Ivan Polyakov and Xuhao Yuan. They were helpful during the laboratory work. I am also grateful to my friends Arvind, Scott, Michael, Hangyi, Xixin and Andy. Special thanks to my good friend Sagnik who I had great conversations about many different topics.

Finally, I want to mention that I am forever grateful to my mother and grandparents for their love and support. They always stay with me during my difficult times. If my father were still alive, he would be incredibly proud of my achievement.

Dedicated to my mother, father and my grandparents.

Contents

List of Figures

List of Tables

1 Standard Model particles

The Standard Model of particle physics describes the interaction between the fundamental particles in nature and how they behave. The universe is governed by four fundamental forces: gravity, electromagnetic, strong and weak forces. Bosons have integer spins and they are governed by Bose-Einstein statistics. Fermions, or matter particles, are described by Fermi-Dirac statistics and they have non-integer spins. The Standard Model concerns about electromagnetic, strong and weak forces but not gravity. Gravity is too weak to play an important role in particle physics so we can simply ignore it. Quantum field theory tells us that all forces in nature have a force carrier particle which mediates force between fermions when they interact with each other. For example, when two fermions interact electromagnetically, they exchange photos. Photons are the quanta of the electromagnetic force. Likewise, strong and weak forces have their own force carriers and they are gluon and W, Z bosons.

So far, the Standard Model (see Figure1) of particle physics is the most successful theory that we currently have. All particles in the Standard Model have been experimentally proven. An important recent discovery was the famous Higgs boson[1] measured by the ATLAS and CMS collaborations in July 2012 [5,6]. However, there are still unanswered questions about the masses of neutrinos, the generation problem,[2] dark matter etc.

All twelve fermions are grouped into three generations. They only differ by their masses from their corresponding particles from other generations. Heavier the mass, the more unstable the particle will become, so our current matter-dominated universe is only made up of the first generation. High energy accelerators can produce muons, taus, and hadrons made up of charm, bottom, and strange quarks, but these particles are not completely stable.

[1] Higgs bosons give mass to other particles.

[2] The Standard Model has three fermion generations. We don't know why there are three.

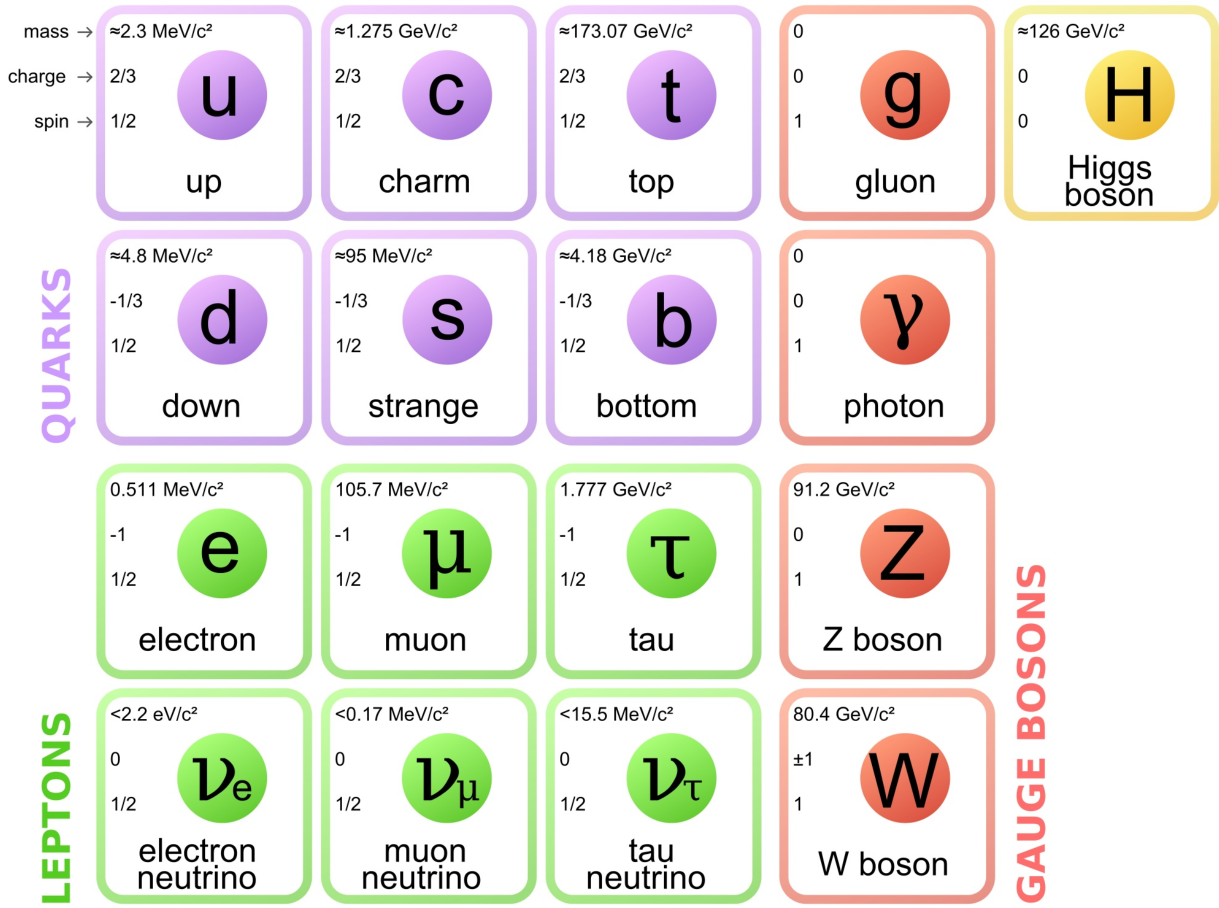

Figure 1: *Standard Model of particle physics.*

Quarks are unique particles, and they possess electric, weak and colour charge, which is an intrinsic property. One can imagine colour as a degree of freedom of a quark, and each quark carries one of three colour charges: red, blue, and green. Anti-quarks have an anti-colour charge. Due to the quark confinement, see Figure.2, no single quark can be observed, and all hadrons, meson and baryon, are colourless. Plus, they form structures like meson and baryon. Quark and anti-quark bounded by gluon forms meson, and three quarks with distinct colours make up baryon. Quarks are subject to all four fundamental forces. Leptons on the other hand, do not participate in strong interaction. They are elementary particles and have integer electric charge. The standard model assumed neutrinos were massless, but experiments showed these particles must have specific masses due to the neutrino oscillation. They only interact via electroweak and gravitational forces, so neutrino detection is enormously difficult. See Table.1 for more details about the properties of the Standard Model particles.

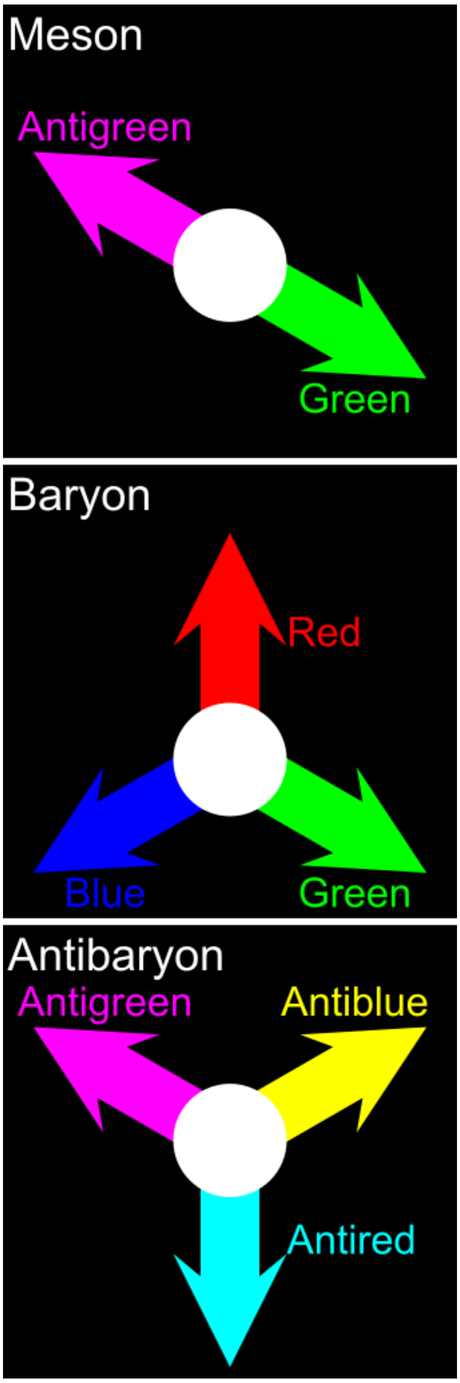

Figure 2: *Illustration of quark confinement. Top: Meson, Middle: Baryon, Bottom: anti-Baryon.*

	Symbol	Name	Mass	Charge
Quarks	u	Up	2.2 MeV	$\frac{2}{3}$
	d	Down	4.7 MeV	$-\frac{1}{3}$
	c	Charm	1.28 GeV	$\frac{2}{3}$
	s	Strange	96 MeV	$-\frac{1}{3}$
	t	Top	173 GeV	$\frac{2}{3}$
	b	Bottom	4.18 GeV	$-\frac{1}{3}$
Leptons	e	Electron	0.511 MeV	-1
	ν_e	Electron neutrino	< 1.0 eV	0
	μ	Muon	105.66 MeV	-1
	ν_μ	Muon neutrino	< 0.17 MeV	0
	τ	Tau	1.7768 GeV	-1
	ν_τ	Tau neutrino	< 18.2 MeV	0

Table 1: *Standard Model fermions and their properties.*

In 1940s, the quantum theory of electrodynamics was formulated by Richard Feynman, Shinichiro Tomonaga, and Julian Schwinger. Quantum Electrodynamics, or QED, is an abelian gauge theory with symmetry group U(1). Quanta (photons) of an abelian gauge field must be massless, uncharged and have integer spin. The fist quantum theory of weak interaction was presented by Enrico Fermi and put into its present form by Sheldon Glashow, Steven Weinberg, and Abdus Salam in the 1960s. The weak interactions, which account for example for beta decay, are mediated by $W^{\pm}$ and Z bosons. These particles are accurately described by an SU(2) gauge theory. In 1983, $W^{\pm}$, Z bosons were discovered in CERN by the UA1 and UA2 collaborations. There was no quantum theory of strong interactions until the development of Quantum Chromodynamics in 1970s. QCD is non-abelian gauge theory with symmetry group SU(3) and gluons are the quanta. The existence of gluons was initially theorized by Gell-Mann and experimentally proven at DESY in 1978. Currently, we have no successful quantum theory for gravity. See Table.2 for more information about the relative strengths of four fundamental forces.

Interaction	Relative Strength (Relative to Gravity)	Force Carrier	Mass(GeV)
Strong	10^{38}	Gluon	0
Electromagnetism	10^{36}	Photon	0
Weak	10^{25}	$W^{\pm}$ and Z bosons	80.4 and 91.2
Gravitation	1	Graviton(hypothetical)	0

Table 2: *Standard Model forces and their relative strengths.*

2 Exotic Hadrons and X(3872) state

The quarks (q) can't exist individually in nature. Instead, they form structures like mesons ($q\overline{q}$) and baryons (qqq). When Gell-Mann proposed quarks, all known hadrons (i.e. particles which can have strong interactions) could be explained as either $q\overline{q}$ or qqq bound states. Theoretically, there is no limit in number of quarks to form a hadron. Hadrons with more than the minimal quark content are often called exotic. Physicists couldn't confirm the existence of exotic hadrons made out of light quark (u, d or s) like tetra- ($qq\overline{q}\overline{q}$) or penta-quarks ($qqqq\overline{q}$) for many years. Fortunately, B-factory experiments have collected huge statistics from e^+e^- collision. An abundant bottom (b) and charm (c) productions brought an ideal playground for the exotic hadrons involving quarks. Top quark (t) is too short-lived to form hadrons.

In 2003, Belle found a very narrow resonance in the $\pi^+\pi^-J/\psi$ invariant mass distribution at $3,872\,\mathrm{MeV}$ in $B^\pm \to \pi^+\pi^-J/\psi K^\pm$ decays [7]. Due to its narrow width, and mass being close to the $D^0\overline{D}^{*0}$ threshold, it was suggested that the $X(3872)$ was not a conventional charmonium state ($c\bar{c}$), but might be a loosely bound $D^0\overline{D}^{*0}$ molecular state (in molecular state two hadrons are bound together by nuclear-type force) or tightly bound tetraquark (direct colour interactions of four quarks). A lot of discussions emerged seeking to give a proper interpretation to this state. Determining its quantum number was crucial. A five-dimensional amplitude analysis was performed by the LHCb collaboration of angular correlations in $B^+ \to X(3872)K^+$, $X(3872) \to \pi^+\pi^-J/\psi$, $J/\psi \to \mu^+\mu^-$ decays and $J^{PC} = 1^{++}$ was determined [8]. Such quantum numbers can be accommodated in both tetraquark and molecular models, as well as in $X(3872)$ interpretation as a charmonium state, $\chi_{c1}(2P)$.

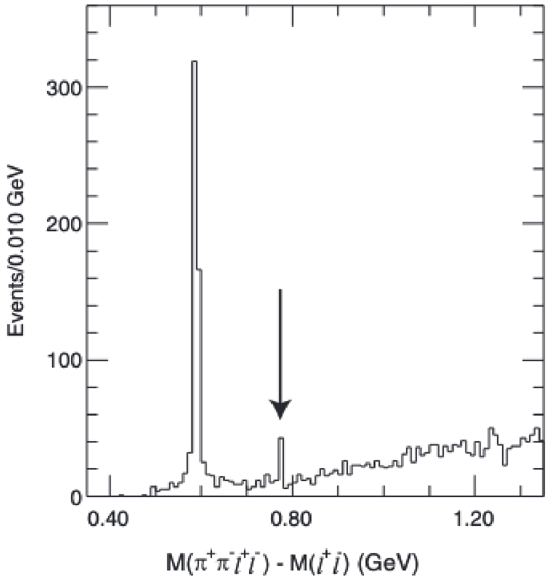

Figure 3: *The distribution of mass difference between* $\pi^+\pi^- J/\psi$ *and* J/ψ *in* $B^\pm \to \pi^+\pi^- J/\psi K^\pm$ *decays. The peak at* $0.59 GeV$ *is due to the* $\psi(2S)$ *charmonium state. The peak corresponding to the* $X(3872)$ *discovery is indicated with an arrow.*

In a tetraquark model, mass splitting due to the mixing between $u\bar{u}c\bar{c}$ and $d\bar{d}c\bar{c}$ was predicted [9], $M(h) - M(l) = (7 \pm 2)/cos\theta \; MeV$, where $M(X_{h,l})$ are the masses of the higher and lower states after the mixing of the two states. The difference is expected to appear as the difference in the $X(3872)$ masses separately measured in $B^\pm \to X(3872)K^\pm$ and $B^0 \to X(3872)K^0$. The Belle result for this difference in the $\pi^+\pi^- J/\psi$ mode is found to be $(-0.71 \pm 0.96(stat) \pm 0.19(syst))MeV$ [10], which disfavors this particular tetraquark model.

A $D^0\overline{D}^{*0}$ molecular interpretation of $X(3872)$ is very plausible, because of its narrow width, $(\Gamma < 1.2MeV)$, and the mass being very close to $(M = 3,871.69 \pm 0.17MeV)$. Both features are expected for loosely bound D^0 and $\overline{D}^{*0}$. Inspired by this argument, $B \to D^0\overline{D}^{*0}K$ decays were reconstructed to examine the $D^0\overline{D}^{*0}$ mass spectrum and a clear overabundance was observed near the threshold. The observed $X(3872)$ mass peak was consistent with that determined by the $\pi^+\pi^- J/\psi$ mode [11,12]. The $\mathcal{BR}(X(3872 \to D^0\overline{D}^{*0}))$ was found to be ten times as large as $\mathcal{BR}(X(3872 \to \pi^+\pi^- J/\psi))$. This was again expected in the molecular model.

The conventional charmonium state, $\chi_{c1}(2P)$, is expected near or above the $D^0\overline{D}^{*0}$

threshold. If its mass coincided with the threshold, such state would also be narrow (decays to $D\bar{D}$ are forbidden), and like to decay to $D^0\overline{D}^{*0}$ above the threshold. Such state would also be expected to have photon and light-hadron transitions to lower charmonium excitations: $\gamma\psi(2S)$, $\gamma J/\psi$, $\pi\pi\chi_{c1}(1P)$ and $\omega J/\psi$. A small fraction of ω decays to $\pi^+\pi^-$, which would give rise to $\pi^+\pi^- J/\psi$ decays, with the dipion mass peaking sharply near its upper kinematic bound reaching the tail of the relatively narrow ω particle. However, the observed dipion mass distribution in $X(3872)$ decays is broadly peaking towards its upper end suggestive of $\rho^0 \to \pi^+\pi^-$ resonance. Large isospin violating $X(3872) \to \rho^0 J/\psi$ decays are not expected for a normal charmonium state. However, the large isospin violation finds natural explanation in the molecular model, because of about 8 MeV difference between the $D^0\overline{D}^{*0}$ and D^+D^{*-} thresholds. This thesis is concerned with the analysis of the dipion mass spectrum in $X(3872) \to \pi^+\pi^- J/\psi$ decays in order to determine relative strength of isospin violating $\rho^0 J/\psi$ and isospin conserving $\omega J/\psi$ decays. This in turn should help us understand the nature of this mysterious resonance.

Recently, the $X(3872)$ state was renamed to $\chi_{c1}(3872)$ by the Particle Data Group. In this thesis, we refer to this particle by its traditional label.

The data were collected with the LHCb detector operating at the Large Hadron Collider (LHC) in 2011-2012 (Run 1) and 2015-2018 (Run 2) periods.

3 Detector Description

3.1 The LHC Machine

The LHC, Large Hadron Collider, is the world's largest hadron colliding machine located on the border between Swiss and France, close to Geneva. The circumference is 27 km, and it sits between 50 to 175 meters beneath the ground (see Figure 4). It is designed to accelerate beams of protons up to an energy of 7 TeV and has two counter-rotating proton beams. These beams must travel in a vacuum environment to avoid collision with gas molecules. The vacuum is cooled to cryogenic temperature — which is at $-271.3°$C — using the liquid helium. To bend the proton beams, LHC uses 1232 dipole magnets and 400 quadrupole magnets to focus the beam in the traverse plane. Each proton beam will have 2808 bunches, and each bunch contains 1.15×10^{11} protons. The LHC accelerates protons to 99.9991% of the speed of light and collides them at four interaction points. There are four detectors in each of these points: ATLAS, CMS, ALICE, and LHCb. ATLAS and CMS are designed to study massive particles like Higgs boson. ALICE is to study heavy-ion collisions and quark-gluon plasma, which is the fifth state of matter in which quarks and gluons are freed. The LHCb detector focuses on the CP violation measurements in b and c meson decays, probing a physics beyond standard model and exploring the exotic hardronic states, which later will be discussed in length.

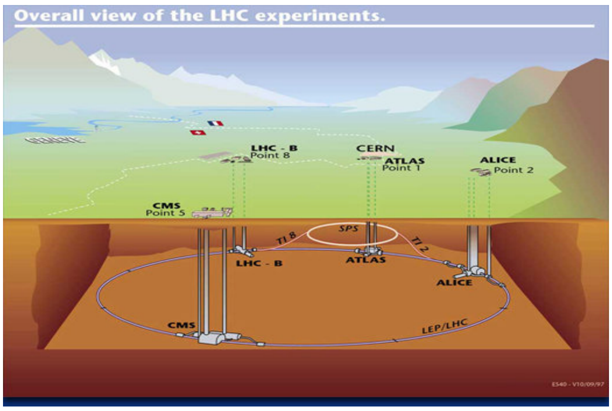

Figure 4: *LHC underground complex.*

In order to accelerate protons to the energy of 7 TeV, several stages of acceleration are applied. The process begins with the extraction of protons by ionazing the hydrogen gas and accelerates them up to 50 MeV in LINAC 2 using radio frequency cavities. After the initial acceleration, protons will be injected into the Proton Synchrotron Booster. With synchrotron rings, the energy of protons will reach 1.4 GeV and start feeding into the Proton Synchrotron(PS)(see Figure 5). The energy will reach 25 GeV in this step. From here, beam will enter Super Proton Synchrotron(SPS) and accelerated to an energy of 450 GeV. Finally, the accelerated protons are injected in the LHC. Proton beams are separated from one another by a time-space of 25 ns corresponding to a bunch crossing rate of 40 MHz. The LHC's luminosity can get to $\mathcal{L} = 10^{34} cm^{-2} s^{-1}$ at the CM(center of mass) energy of $E_{cm} = 14\,\text{TeV}$.

Table 3: *Two main LHC parameters of proton-proton collision.*

Year	2011	2012	2015	2016	2017	2018
$\sqrt{s}$ TeV	7	8	13	13	13	13
Lumi fb^{-1}	1.0	2.0	0.3	1.6	1.7	2.1

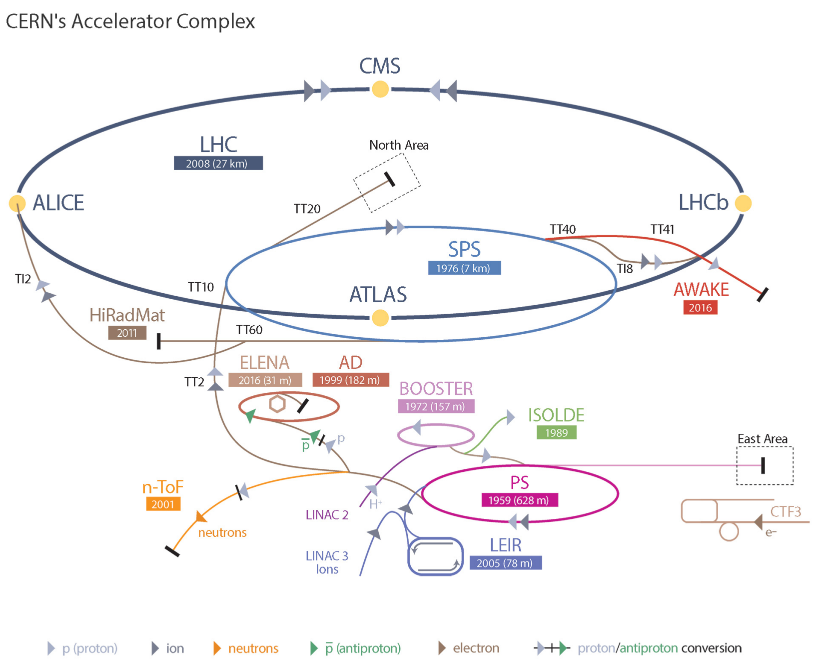

Figure 5: *The LHC accelerator complex.*

3.2 LHCb Detector

The LHCb is a single-arm forward spectrometer with an angular coverage roughly from 10 mrad to 300 mrad. The layout of the detector is show in Figure.6. This corresponds to a pseudorapidity range of $1.8 < \eta < 4.9$. The unique design of the LHCb detector is due to the production of b and $\bar{b}$ quarks at the LHC collision such that their production likely to be along the beam direction and this allows the LHCb to cover optimal amount of the b and $\bar{b}$ quark scattering thus, have a huge quantity of B meson data(see Figure. 7).

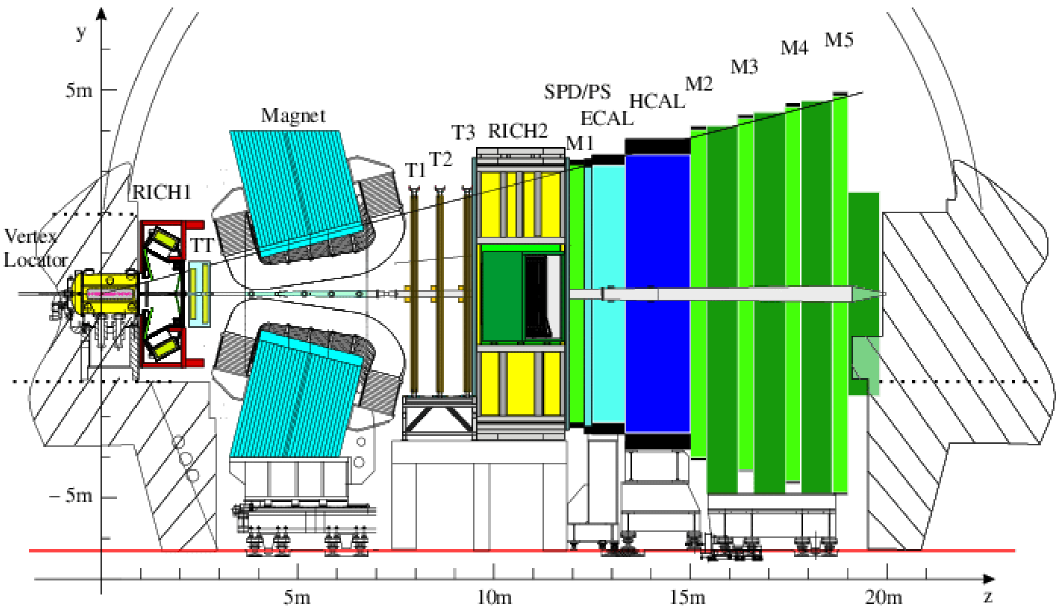

Figure 6: *LHCb Detector.*

The LHCb consists of multiple subdetectors, and each has its specific role in the experiment:

- The Vertex Locator, or VELO, is the silicon vertex tracker built around the beam pipe. Its role is to resolve Primary Vertex with high precision.
- The Ring Imaging Cherenkov (RICH1) is one of the two Cherenkov detectors used for particle identification.
- The Tracker Turicensis (TT), is the first tracking station. It is located before the LHCb's dipole magnet.
- The Outer Tracker (OT) and Inner Tracker (IT) are subsequent detectors right after

the magnet. OT covers the entire magnet. IT covers the high occupancy region close to the beam pipe.

- The RICH2 is the second Cherenkov detector.
- Calorimetry has two subsystems, the Electromagnetic calorimeter(ECAL) and the Hadronic calorimeter(HCAL). These two detectors' purpose is to measure the energy deposited by electromagnetic and hadronic showers, respectively.
- Muon stations are the final part of the LHCb detector. Five of them are located after the ECAL and HCAL.

All of these subdetectors will be discussed briefly in the following sections. A more detailed explanations can be found in [13].

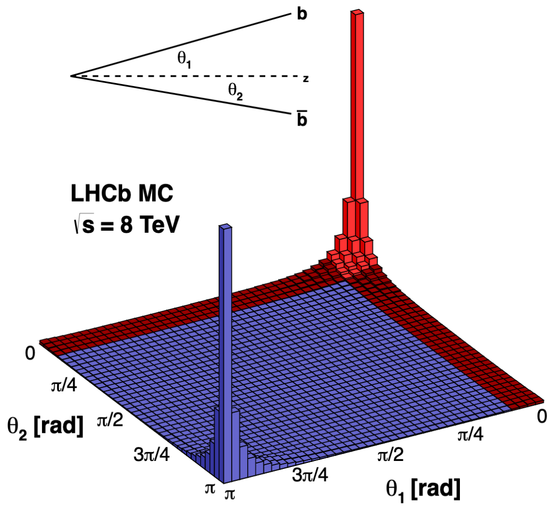

Figure 7: *PYTHIA8 simulation of $b\bar{b}$ production in LHCb. Red region shows the LHCb acceptance.*

3.3 Tracking system

The purpose of the tracking system is the momentum measurement of the charged particle. When charged particles travel through the magnetic field, the particle's trajectory will bend due to the Lorentz force. By measuring the radius of the curvature, one can know the momentum of the particle. The LHCb's tracking system consists of VELO, dipole magnet, and tracking stations(TT, OT, and IT). The TT is placed directly upstream from the magnet, while the rest are down-stream(see Figure. 8). The magnetic field is designed to have a strong y component; therefore, the particles traveling along the z-axis will be bent mostly in the x-z plane.

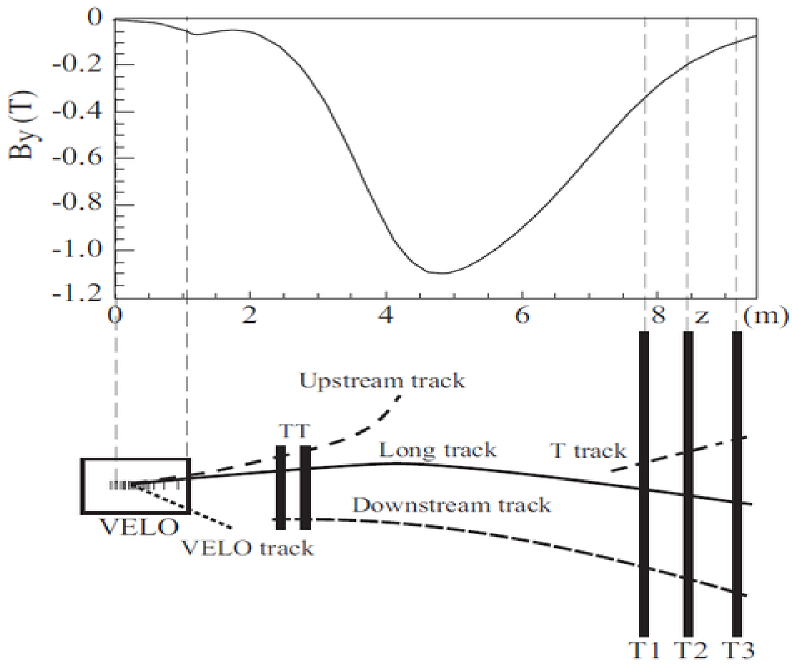

Figure 8: *Schematic of the tracking components with different types of track definitions.The main magnetic component (B_y) as a function of the z coordinate is plotted above.*

3.3.1 Vertex Locator(VELO)

The VELO is located around the *pp* interaction point. It closely wraps the beam pipe to measure the primary interaction and secondary displacement vertices. The VELO operates in intense radiation environment which requires the detector to have high radiation tolerance. The VELO has the full angular acceptance of the pseudorapidity range $1.6 < \eta < 4.9$. At least three VELO station hits are required to reconstruct the tracks. The signal to noise ratio is larger than 14. This certify efficient trigger performance. The spatial resolution of the VELO is 4 µm for 100$mrad$ tracks in the smallest strip pitch region. Pitch is the space between the strips of the sensor. The R sensor of VELO has the pitch range from 40 µm to 102 µm. For the Φ sensor, the range is 38 µm to 96 µm. The VELO consists of 21 stations, with each containing two half-disk-shaped silicon-strip detector modules. They consist of two different types of 300 µm thick sensors mounted back to back. The R sensors measure the radial distance of a particle track to the beam axis and are made of circular strips around the beam. The Φ sensors are made of straight radial strips and measure the polar angle of the tracks(see Figure. 10).

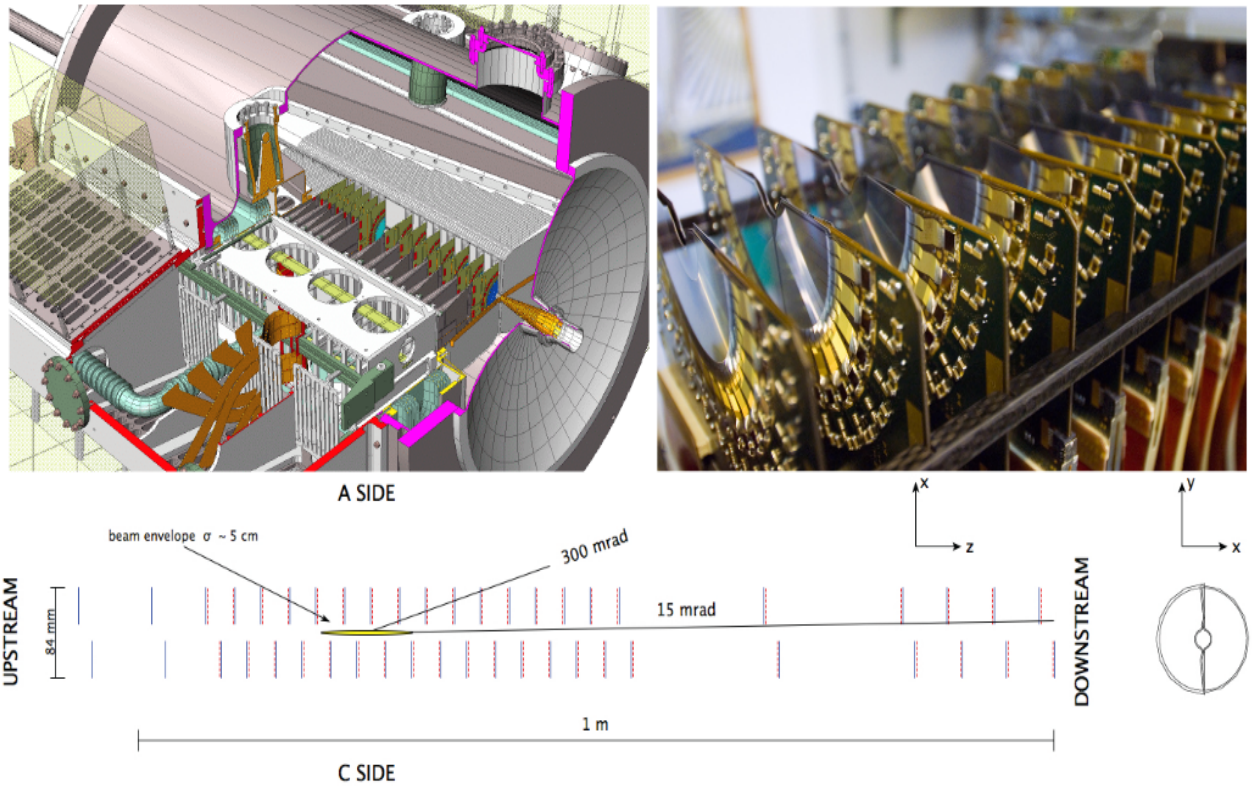

Figure 9: *Top left: The LHCb VELO vacuum tank. The cut-away view allows the VELO sensors, hybrids and module support on the left-hand side to be seen. Top right: A photograph of one side of the VELO during assembly showing the silicon sensors and readout hybrids. Bottom: Cross-section in the x-z plane at y=0 of the sensors and a view of the sensors in the x-y plane.*

Additional two pile-up stations are located upstream of the VELO consisting of two r-sensor modules. They are used in the hardware trigger, Level-0 Trigger will be discussed in section, to detect beam-gas interactions. The precision of the reconstructed vertices

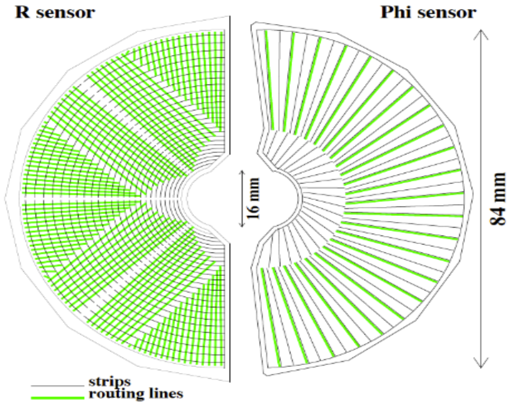

Figure 10: *Representation of an R and ϕ sensor.*

depends on the extrapolation of the measured track positions. Therefore, the VELO modules are placed close to the interaction point. The sensitive regions of the modules starts in $8mm$ distance from the beam line. To protect the sensors from excessive radiation damage during unstable beam conditions, the half modules can be moved away from the beam line.

3.3.2 Dipole Magnet

A dipole magnet consists of of two separate aluminum coils, shaped like a saddle and mounted symmetrically in a window-frame magnetic yoke(see Figure. 11). The magnetic field is vertically oriented (in the y-direction), and covers ± 250 mrad vertically and ± 300 mrad horizontally. The integrated magnetic field for tracks of 10m in length is $4Tm$. In order to obtain the desired momentum resolution, the integrated magnetic field must be with a precision on the order of 10^{-4}.

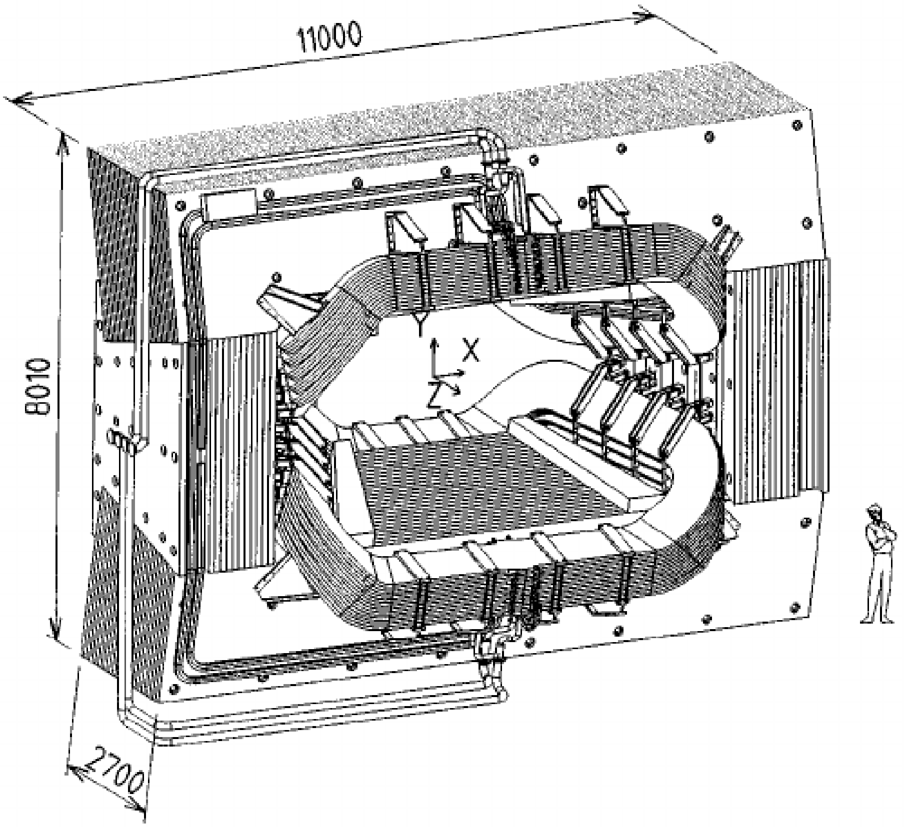

Figure 11: *The LHCb magnet.*

3.3.3 Tracker Turicensis

The Tracker Turicensis (TT) is a silicon strip tracking station. It is located upstream of the dipole magnet(closer to the pp region and the VELO detector). It has two 150cm wide and 130cm high stations with an area of 8.4 m^2. Each station consists of two detection layers with the $x-u$ and $v-x$ arrangement. All four layers are separated from each other by 27cm along the beam axis. The middle two-layer can rotate with a stereo angle of $\pm 5^o$. This orientation provides high precision tracking for the track reconstruction. The TT contains 143,360 readout strips. The strips are 500 μm thick with a pitch of 183 μm. The single hit resolution of the TT is around 50 μm. Each half-module consists of a row of seven silicon sensors positioned as shown in Figure.12. The seven silicon sensors are grouped into two (4-3) or three (4-2-1) readout sectors. 4-3 type and 4-2-1 type half modules have L sector formed by the four sensors closest to the readout. These four sensors are bounded together and directly connected to the lower-most readout hybrid. For4-3 type half module, the remaining sector is M sector which is composed of three sensors.These three sensors are connected to a second readout hybrid mounted on top of a hybrid by a kapton flex cable with a length of 39 cm. The TT sensors are read out with Beetle front-end chips. For the TT sensors, they have 512 readout strips. The sensors are kept below 5°C by aluminium and copper blocks and cooled with C_6F_{14}.

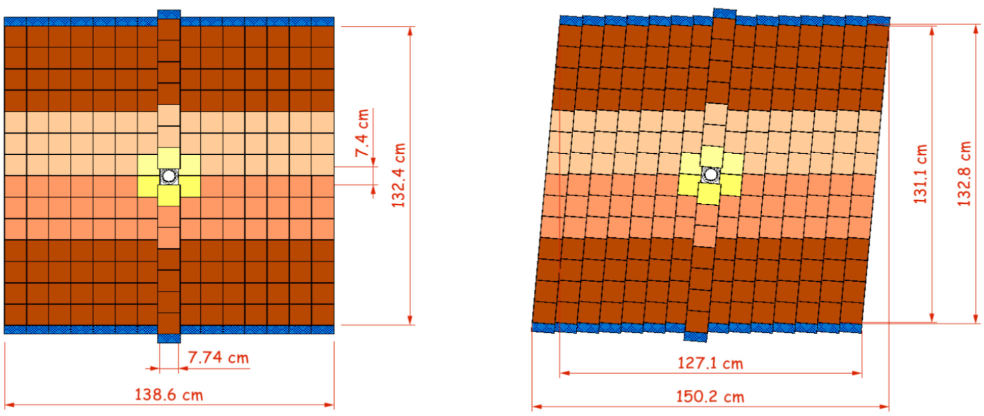

(a) x-layer of TT

(b) u-layer of TT

Figure 12: *Schematics of the TT. Each color corresponds to different readout sections.*

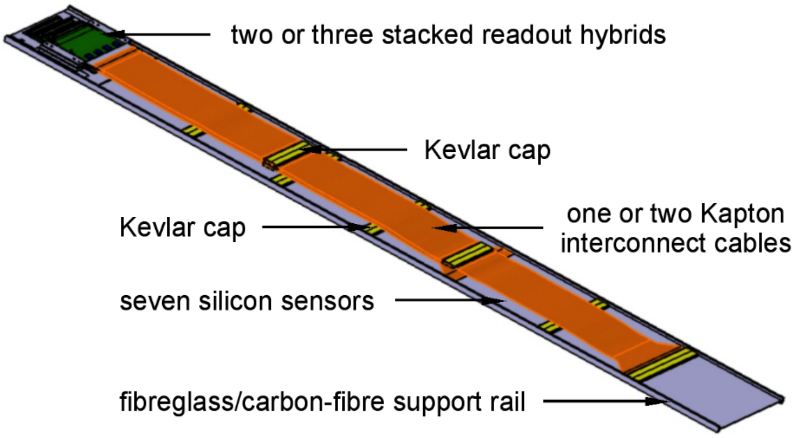

Figure 13: *The TT half module.*

3.3.4 Inner Tracker

The Inner Tracker is a silicon strip detector with four sections: ASide, CSide, Top, and Bottom, located in the center of the three tracking stations after the TT. It covers the region around the beam pipe 120cm wide and 40cm high with an area of around $4\,\mathrm{m}^2$. Similar to the TT, it has four layers with $x - u - v - x$ arrangement, and the middle two-layer are rotated with an angle of $\pm 5^o$. The strip geometry was chosen to limit the maximum hit occupancy per sensor to a few percents. The pitch between the sensors is about 200 µm leading to a single hit resolution about 50 µm, similar to the TT. The IT modules consists of either one or two silicon sensors that are connected via a pitch adapter to a kapton front-end readout hybrid. The IT sensors are read out with Beetle front-end chips. The IT sensors are 7.6cm wide and 11cm long, and carry 384 readout strips. Like the TT, IT sensors are kept below 5°C.

The Beetle chip is connected to 128 readout strips. The Beetle chip sample the detector signals at the 40MHz and store the sampled data in an analog pipline. Then the signals from one front-end readout hybrid are transmitted from the detector boxesto the service boxes via a shielded 68-wire twisted-pair cable. The procedure is illustrated in Figure.15.

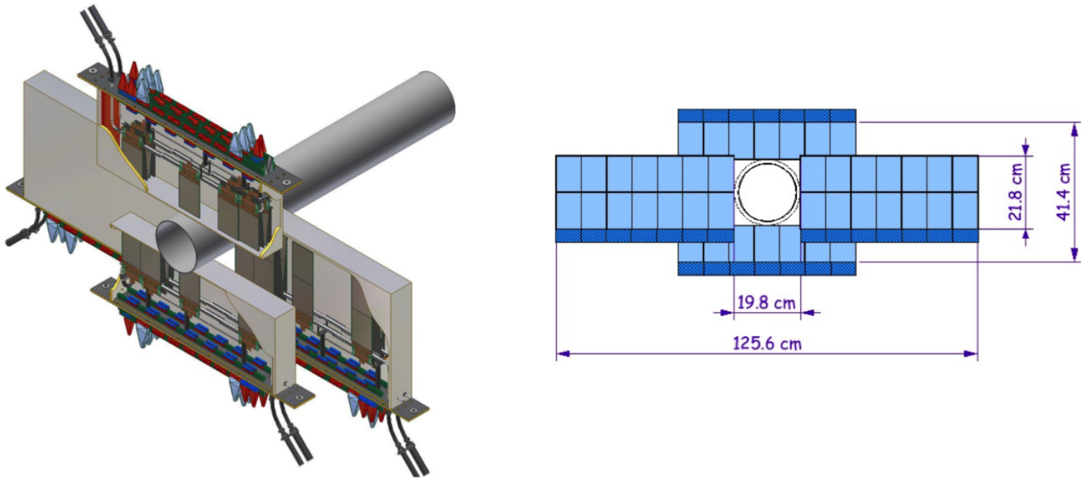

Figure 14: *Left: IT is wrapped around the beam pipe. Right: IT layout.*

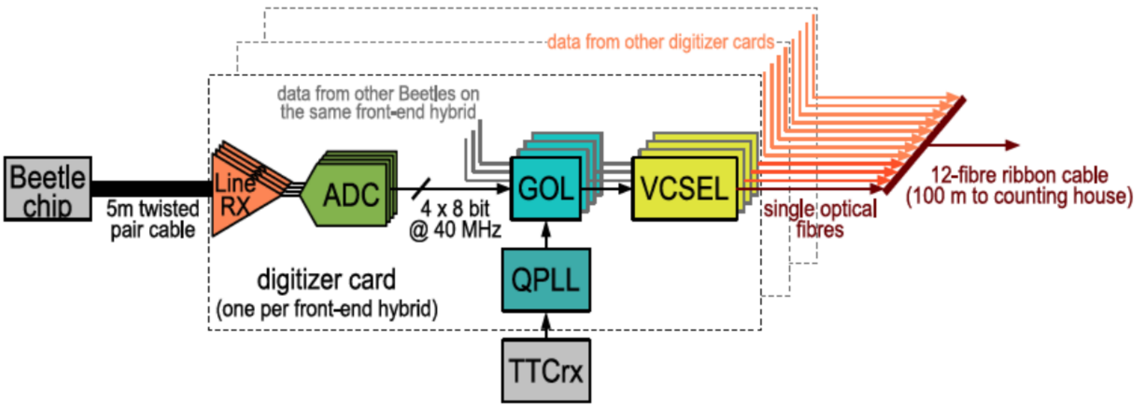

Figure 15: *Signal processing from Beetle chip.*

3.3.5 Outer Tracker

The Outer Tracker(OT) is drift-time detector that include three stations. The design of the OT was based on the need to achieve momentum resolutions δ_p/P of close to 0.4% to resolve the mass of reconstructed B-hadrons to within 10 MeV. The OT cover the IT entirely and it covers $30\,\mathrm{m}^2$ active area. With this coverage, OT is able to measure charged particle with huge acceptance. The OT uses gas-tight straw-tube modules. Each

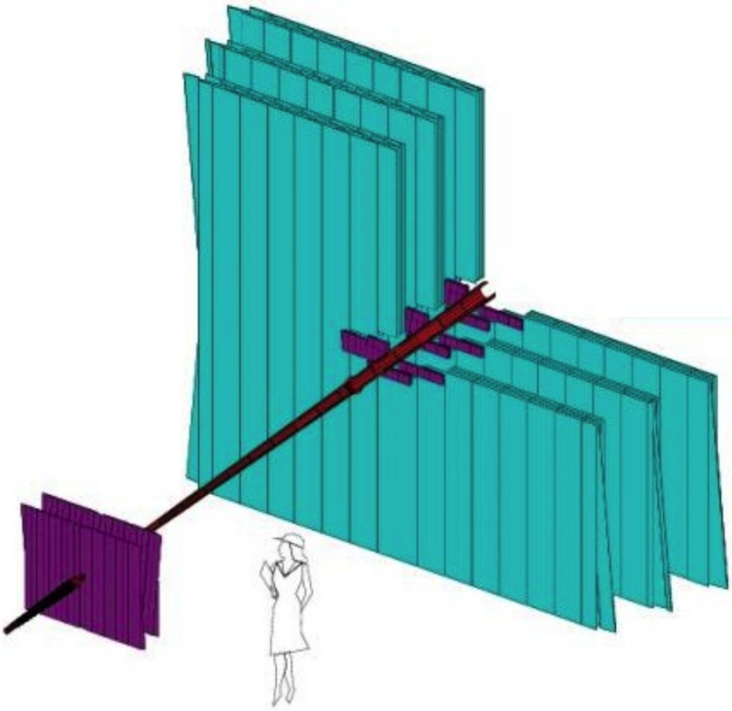

Figure 16: *The Outer Tracker detector.*

module has two stacked layers of drift tubes. The drift tubes are $12m$ long with $4.9mm$ inner diameters. To keep the fast drift time below $50ns$, The tubes are filled with a gas mixture of Argon (70%), CO2(28.5%) and Oxygen (1.5%). Along the center of the drift tube, there is an anode wire which is made of gold plated tungsten of 25 µm diameter and set to +1550 Volts. The outside of the cylinder is made out of cathode and it is grounded. When charged particle traverse through the drift tube, it will ionize the gas inside the chamber. The electrons will drift to the anode wire. Thickness of the cathode material is 40 µm and its is made out of carbon-doped polyamide foil wound simultaneously with a 20 µm thick kapton aminated with aluminum of 12.5 µm thickness. The cross section of the OT module is shown in Figure.17.

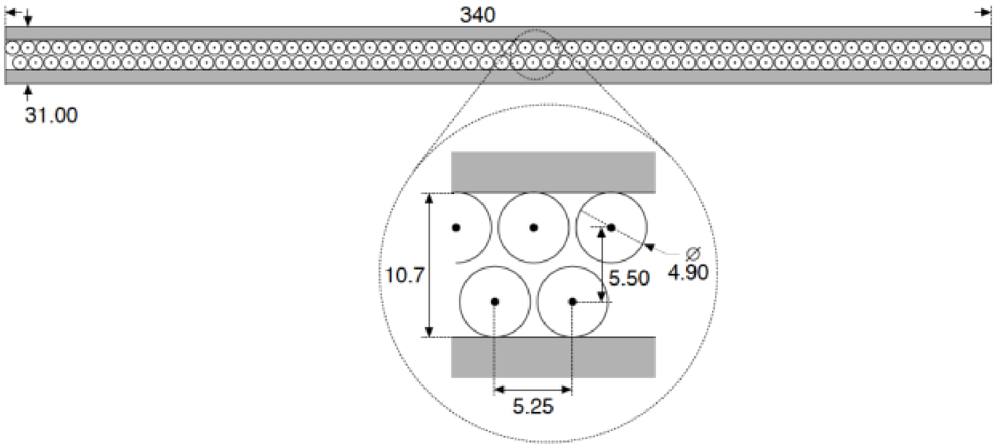

Figure 17: *The Outer Tracker cross section.*

3.4 Particle Identification System

Particle Identification(PID) is crucial for the LHCb analysis. The LHCb's PID system consists of two Ring Imaging Cherenkov Detector(RICH1 and RICH2), Electromagnetic Calorimeter(ECAL), Hadronic Calorimeter(HCAL), and Muon stations. The two RICH detectors will identify charged mesons and baryons in different momentum ranges. The ECAL and HCAL will measure electrons and neutral particles by their energy deposited in the detector. The Muon stations are for identifying the muons.

3.4.1 The Ring Imaging Cherenkov Detectors

The two Ring Imaging Cherenkov (RICH1 and RICH2) detectors distinguish kaons from pions and protons. The first (RICH1) is locatedbetween the VELO and the magnet and occupies the region $990 < z < 2165mm$. The second(RICH2) is placed downstream of the T-stations with its front face positioned at $9500mm$ from the interaction point and with a depth of $2332mm$. The RICH detectors rely on Cherenkov radiation emitted at angle θ_C to the direction of motion of a particle travelling at velocity $v > c/n$ in a medium with refractive index $n > 1$. The Cherenkov angle is given by $cos\theta_C = c/nv$. The ring resolution is proportional to $\sigma_\theta/\sqrt{N}$ where σ_θ is the uncertainty on the Cherenkov's angle and N is the number of photoelectrons in the ring [14]. Figure.19 shows the relation between Cherenkov's angle and particle momentum in different radiators.

The RICH1 detector give particle identification in the momentum range $1 < p < 60\,\text{GeV}$ while RICH2 operates in a reduced acceptance of ± 15 to $\pm 120 mrad$ in the horizontal plane and $\pm 100 mrad$ in the vertical plane, and identifies particles with momenta in the range $15 < p < 100\,\text{GeV}$(see Figure.18). The detector instrumentation is kept out of the detector acceptance region by reflecting the light out of the chamber to hybrid photon detectors(HPDs) with spherical and flat mirrors. HPDs have great spatial resolution and response time. The RICH1 contains aerogel and C_4F_{10} while RICH2 contains CF_4. Aerogel is made up of grains of amorphous silicon dioxide with size ranging from 1 to 10 nm linked together in a three dimensional structure filled by air. These gases are chosen for

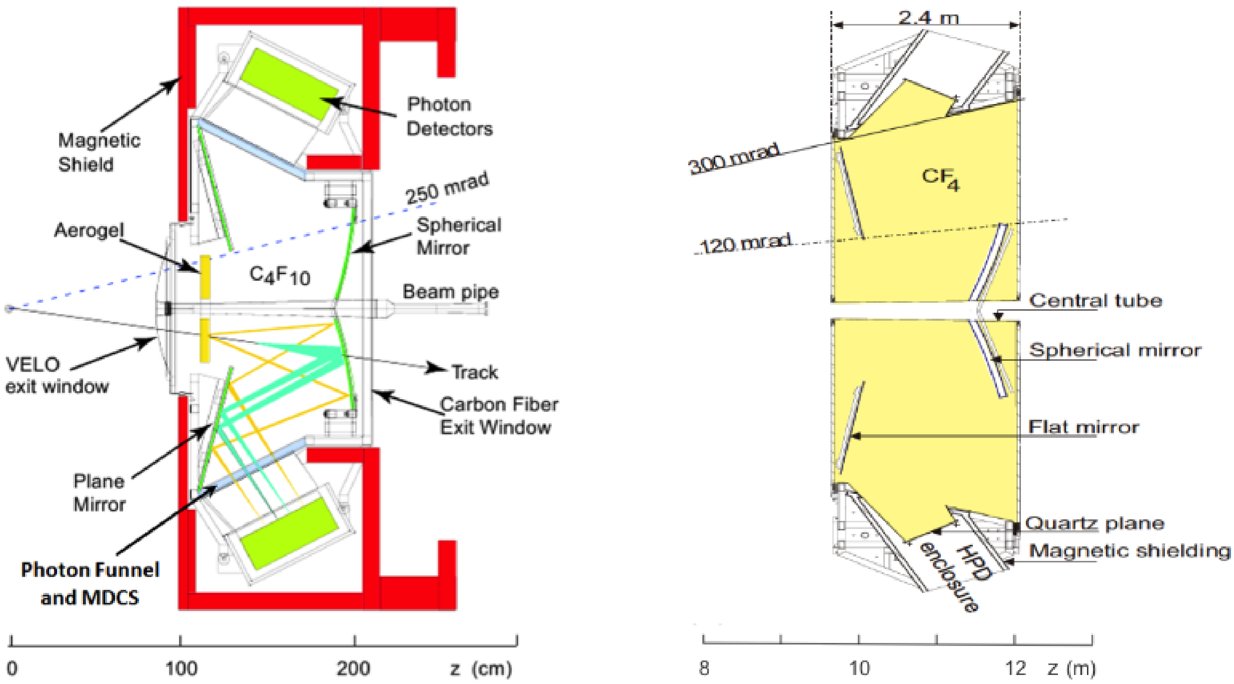

Figure 18: *Left: RICH1, Right: RICH2.*

their refractive indices, n, which are appropriate for the momentum spectrum of the decay products of b and c mesons. A track passing through 5 cm of aerogel with refractive index $n = 1.03$ for light of wavelength 400 nm is expected to yield around 6.5 photoelectrons in a ring from a charged particle. The corresponding yields for 95 cm of C_4F_{10}($n = 1.0014$ at 400 nm), and 180 cm of CF_4($n = 1.0005$ at 400 nm) are 30 and 22 photoelectrons respectively. To determine whether the ring best matches the expectation from a kaon, pion, or proton hypothesis, a likelihood fit is used. The photons are emitted in the shape

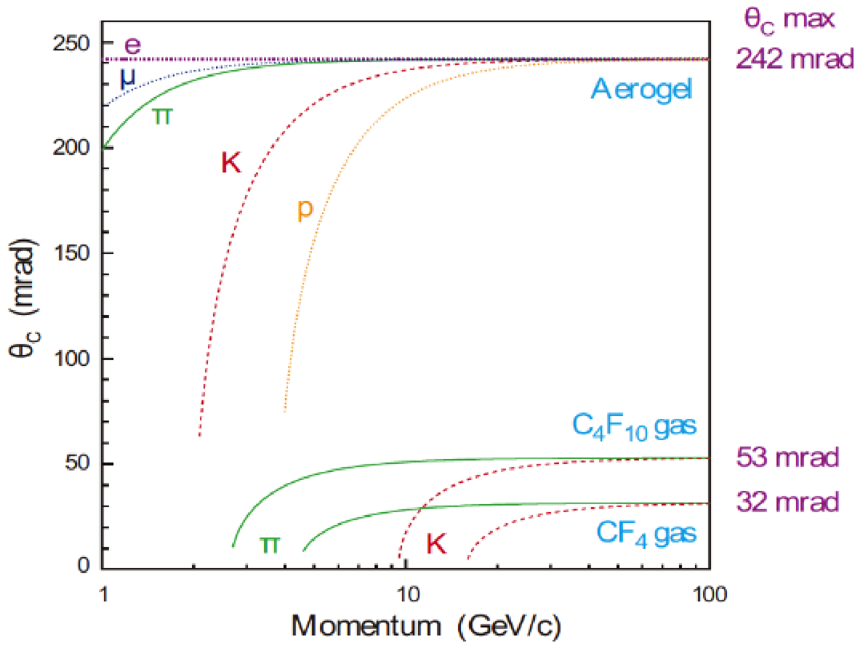

Figure 19: *Cherenkov angles as a function of momentum.*

of a cone along each track in the radiators, and spherical mirrors are used for focusing the light. The spherical mirrors and flat mirrors work together and bring the image to the photon detectors which are mounted out of the acceptance to avoid degrading the tracking. The detection of photons is measured by Hybrid Photon Detectors (HPD) which use silicon detector anode inside the vacuum tube(see Figure.20). Each tube comprises 1024 pixels arranged as a 32×32 matrix, while each pixel has size of $500 \times 500\ \mu m^2$. The HPDs are arranged in a hexagonal pattern outside the RICH detectors. They are shielded from the magnetic field by large iron boxes. The photoelectrons are released in the HPDs during the interaction of incident photons with the photocathode(see Figure.21). The photoelectrons are accelerated by an applied voltage of 10 to 20 kVolts onto a reverse biased silicon anode and this gives the creation of an average of one electron-hole pair for every 3.6 eV of deposited energy. The HPDs are read out by integrated pixel chips. The silicon anodes of the HPD are bump bonded to the LHCbPIX1 binary read out ASIC and thence to the RICH electronics implemented on FPGAs. Specifically designed algorithms converts the rings seen in the RICH detectors to a likelihood for a kaon, pion, or proton mass hypothesis. Combining the information of velocity with the momentum measured

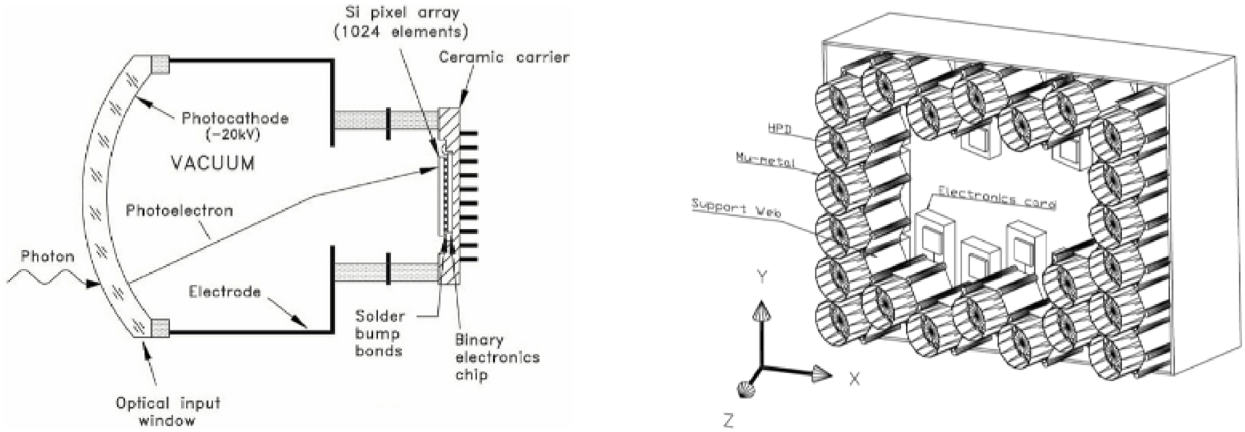

Figure 20: *Left: Hybrid Photon Detector schematics. Right: HPD array of the RICH1 detector.*

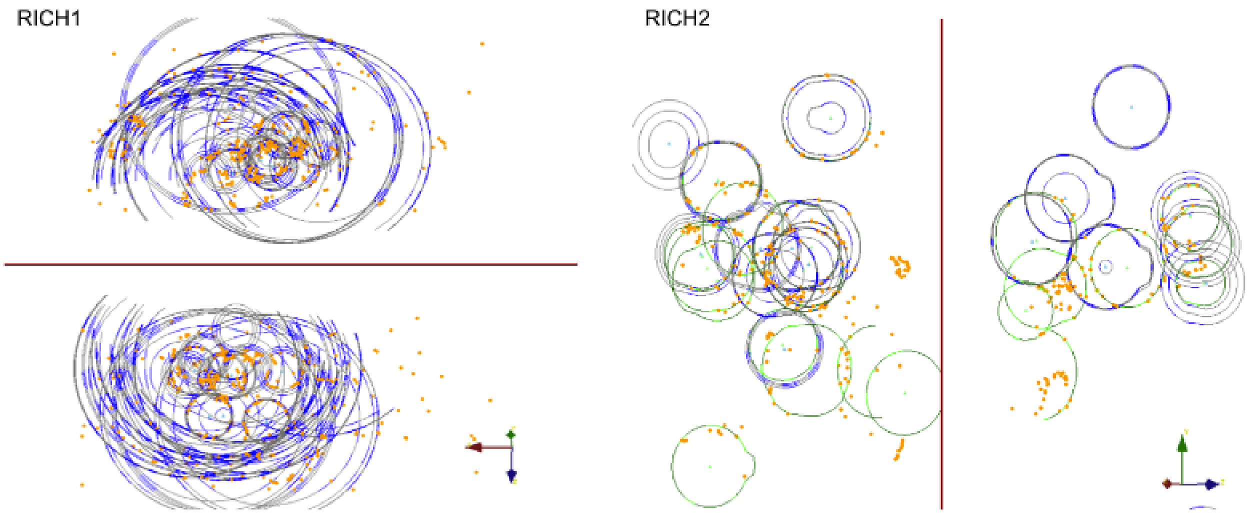

Figure 21: *Event display of detected photoelectrons in RICH1 (left) and RICH2 (right).*

from tracking system,the probability likelihood distribution is determined for each type of particle and compared to a probability likelihood of pions in the RICH detectors. The difference in log-likelihood function is $DLL_{X\pi} = log(P_X/P_\pi)$. Here P is the momentum and X is the particle to be defined. A plot of difference in log-likelihood is shown in Figure.22 for tracks that have been matched to true kaons and pions [15]. In Figure.22, DLL value for kaons tends to be positive but orpions tends to be negative. A data-driven approach is used to check the PID performance of RICH detector. This requires large pure

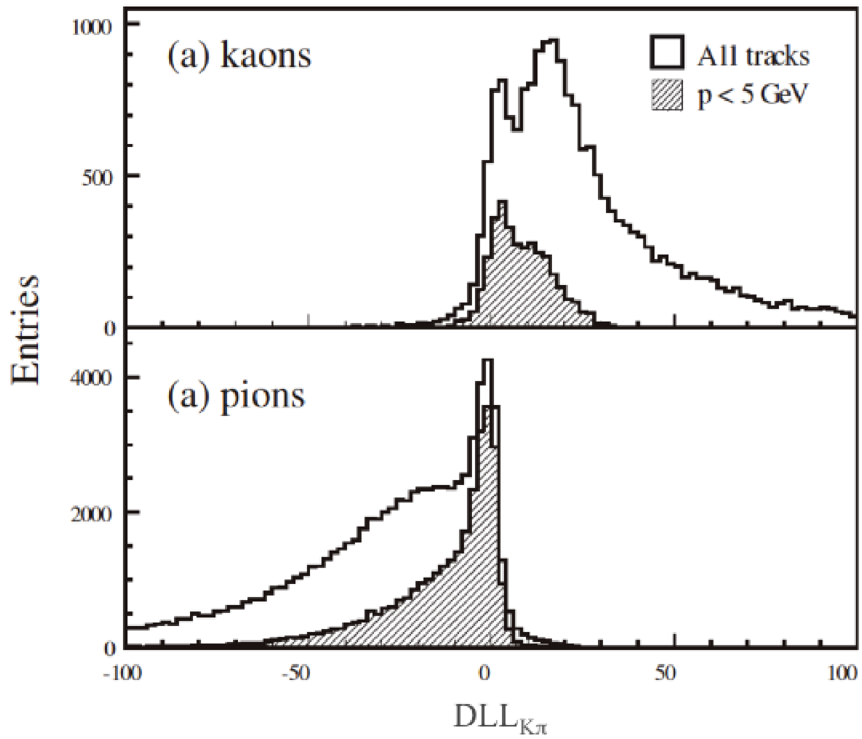

Figure 22: *Difference in log-likelihood between kaon and pion hypotheses for kaons (top) and pions (bottom).*

samples. Each sample covers the full momentum range of 2 to 100 GeV. Furthermore, the selection of such control samples has to be independent of PID information. Kaon and pion samples are reconstructed from $K^0_S \to \pi^+\pi^-$, $\Lambda \to p\pi^-$, and $D^{*+} \to D(K^-\pi^+)\pi^+$. The Figure.23, the kaon efficiency, pion misidentification rate as a function of momentum.

3.4.2 The Calorimeters

The calorimeters have dual role of identifying and reconstructing neutral particles like photons, π^0, and electrons, and measuring the transverse energy of electron, photon and charged hadron showers for the hardware trigger. They operate by collecting scintillation light from particle interactions with dense material through optical fibres. The LHCb's calorimeter system consists of three parts: the preshower/scintillator pad detector(PS/SPD), the electromagnetic calorimeter(ECAL) and the hadronic calorimeter(HCAL). The PS/SPD is to distinguish electrons from charged hadrons and neutral

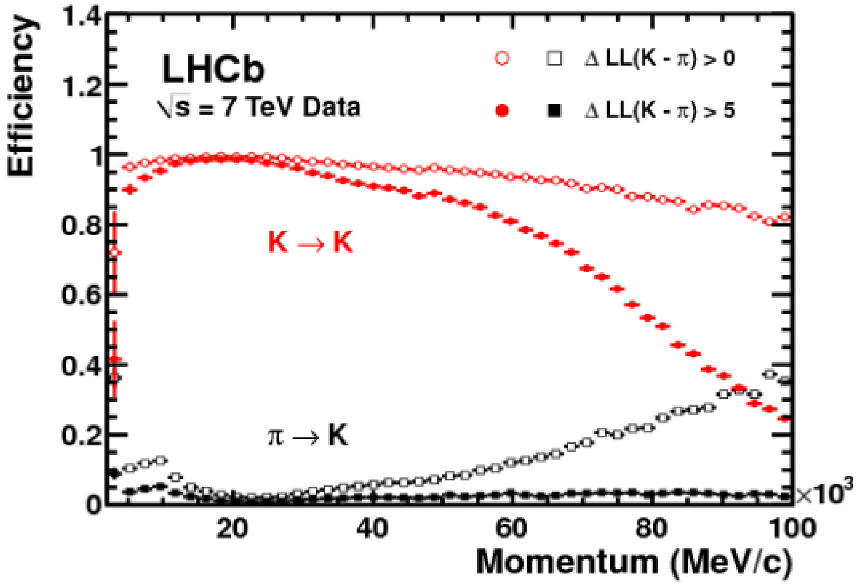

Figure 23: *The kaon identification efficiency and the rate of muon misidentification as a function of momentum.*

pions. It consists of a 15 mm thick lead plate sandwiched between two layers of scintillator pads, before ECAL(see Figure.24). Charged particles like electrons deposit energy in the first scintillator and can be differentiate from neutral particles, such as photons. The SPD/PS detectors use scintillator pad readout by wavelength-shifting (WLS) fibers coupled to multi-anode photo-multiplier tubes (MAPMT)via clear plastic fibers, and cover $7.6 \times 6.2\,\mathrm{m}^2$ active area [16]. The SPD/PS detectors consist of two almost identical rectangular scintillator planes with 12032 channels(cells) of scintillator pads, while a lead converter of 15mm thickness is between the two planes. Each plane is made of two halves which can slide independently on horizontal rails. Furthermore, each plane is divided into three sections:inner(3072 cells), middle(3584 cells) and outer (5376 cells). Hadrons have a longer interaction length and therefore they pass through without depositing not much energy. Around 99.6% of pions don't deposit sufficient energy to meet the threshold to be identified as an electron, while at least 90% of electrons with momenta above 10 GeV pass the threshold and can be detected.

The ECAL is a lead sampling scintillator. It is subdivided into inner, middle, and outer sections of increasing cell size, a scheme also adopted in the PS/SPD. The dimensions of the ECAL are $7.76 \times 6.30\,\mathrm{m}^2$ with angular coverage of ± 25 mrad to ± 300 mrad horizontally

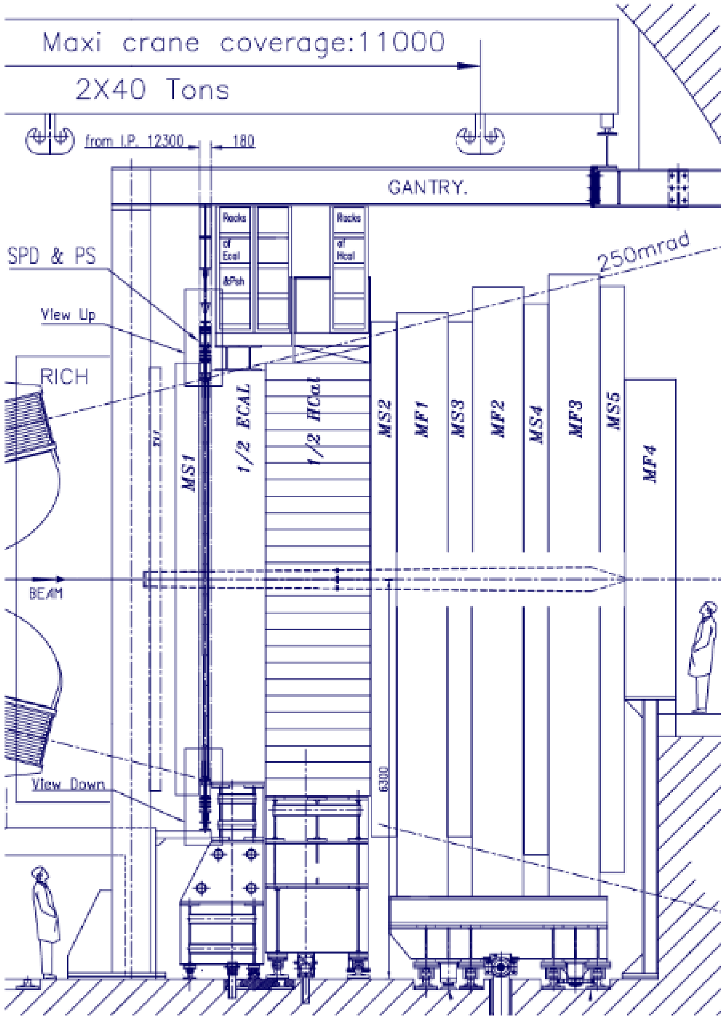

Figure 24: *View of the SPD/PS detectors.*

and ±250 mrad vertically. The purpose of the ECAL is to identify neutral particles like photons and π^0 for trigger and offline analysis. The total thickness of the ECAL layers is 42 cm and it is enough for all energy in an electromagnetic shower to be captured. This required for good energy resolution. Each module is constructed from alternating layers of 2 mm thick lead, 120 µm thick reflecting paper and 4 mm thick scintillator tiles. When excited by the passage of a charged particle, the polystyrene scintillator molecules release a small fraction of the excitation energy as photons. The Molière radius(transverse shower size) of the stack of modules is 3.5 cm. The energy resolution $\sigma(E)/E$ was determined using a test beam and improves from 3% to 1% as the momentum increase from 15 to 100 GeV [17].

The HCAL has similar structure but the absorber is iron rather than lead. It is divided into square cells of length 131.3 mm in the inner section and 262.2 mm in the outer section. Hadronic triggering does not require such good energy resolution, so to save space for the muon stations the thickness of the HCAL is 5.6 interaction lengths. The resolution is much worse than the resolution of the ECAL. The $\sigma(E)/E$ varying as a function of momentum from 23% at 15 GeV to 12% at 100 GeV.

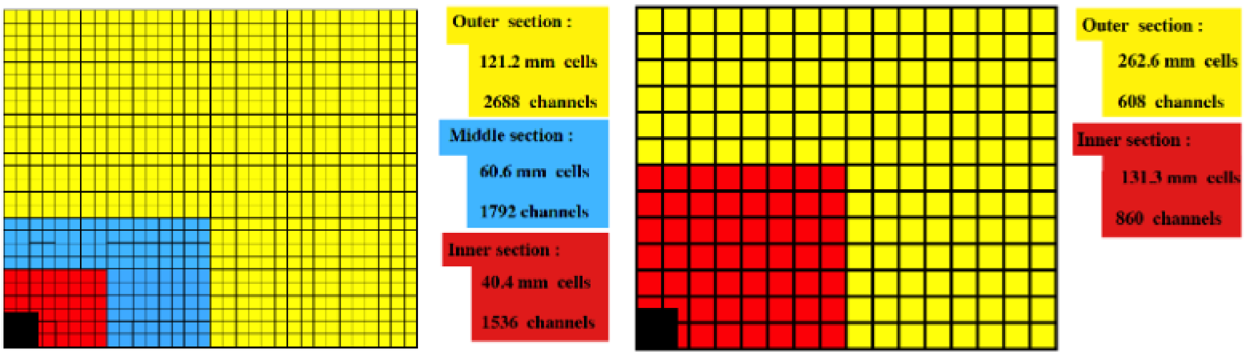

Figure 25: *Segmentations of the SPD/PS and ECAL(left) and HCAL(right).*

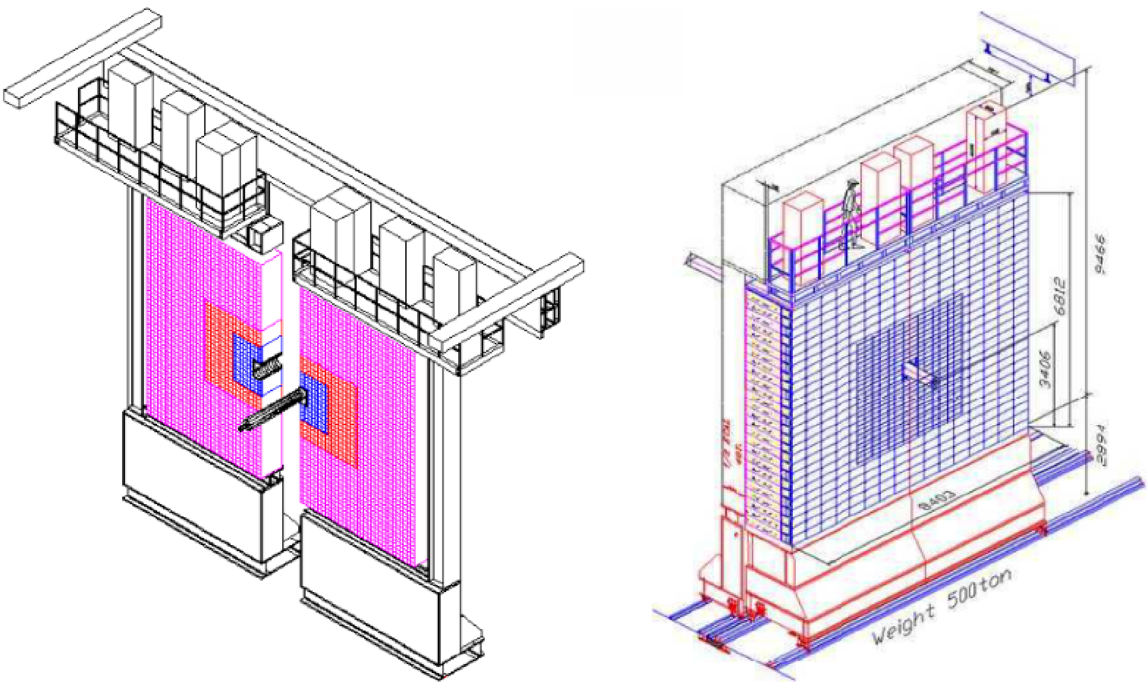

Figure 26: *Overview of the ECAL and HCAL. Left: ECAL and Right: HCAL.*

The cells in ECAL and HCAL(see Figure.25) are read out to photomultiplier tubes by plastic wavelength-shifting fibers. The PS/SPD photomultipliers have multiple anodes, each of which covers several cells. The photomultiplier tubes are encased in iron to shield them from stray magnetic fields. A pulse shaper takes the output of photomultiplier tubes and removes the tail of pulses that are extending beyond 25 ns, so that every LHC bunch crossing can be measured and potentially activate the trigger. The front end board receives the resulting pulses and digitises them.

3.4.3 The Muon System

Muons are important for LHCb analysis because they are present in many b meson decays. Plus, the easiest way to trigger the detector is on muons with high transverse momentum p_{T}. There are five muon stations in LHCb. First muon station(M1) is located between RICH2 and ECAL. The remaining four stations (M2-M5) are placed downstream of the HCAL. The muon stations covers an angular acceptance of ± 20 mrad to ± 306 mrad horizontally and ± 16 mrad to ± 258 mrad vertically(see Figure.27). Muons play crucial role for determining the ω contribution in $B^+ \to X(3872)K^+$, $X(3872) \to J/\psi\rho^0$, $J/\psi \to \mu^+\mu^-$, and $\rho^0 \to \pi^+\pi^-$ decays, which will be discussed in later chapter. The whole muon system consists of 1368 multi-wire proportional chambers and 12 sets of three gas electron multiplier foils in the region closet to the beam pipe in the most upstream station where the particle flux is highest. Each station of the muon system is divided into four regions, R1 to R4 with different logical pad dimensions. Their pad segmentations scale in the ratio 1:2:4:8 (see Figure.28). The stations are divided into cells. Each cell gives a binary decision to trigger, which requires aligned hits above the discriminator threshold in all five stations to fire. The efficiency of each station must be above 95%. The spatial resolution is determined by the cell size. The timing resolution is adequate to distinguish LHC bunch crossing at $40MHz$. The multi-wire proportional chamber is a kind of proportional counter constructed with changing planes of high voltage wires and sense wires grounded or connected to a negative voltage. The chamber is filled with fast, non-flammable gas mixtures of Ar,CO2, and CF4. The studies show that a time resolution of around 5 ns can be achieved in a gas gap with 2 mm wire spacing and 5 mm gas gap.

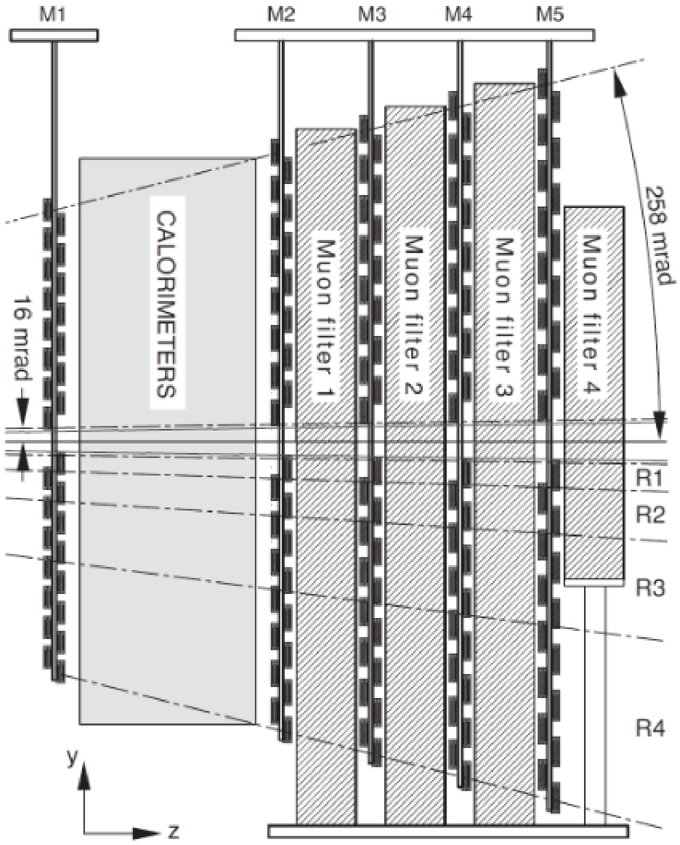

Figure 27: *Overview of the LHCb muon stations.*

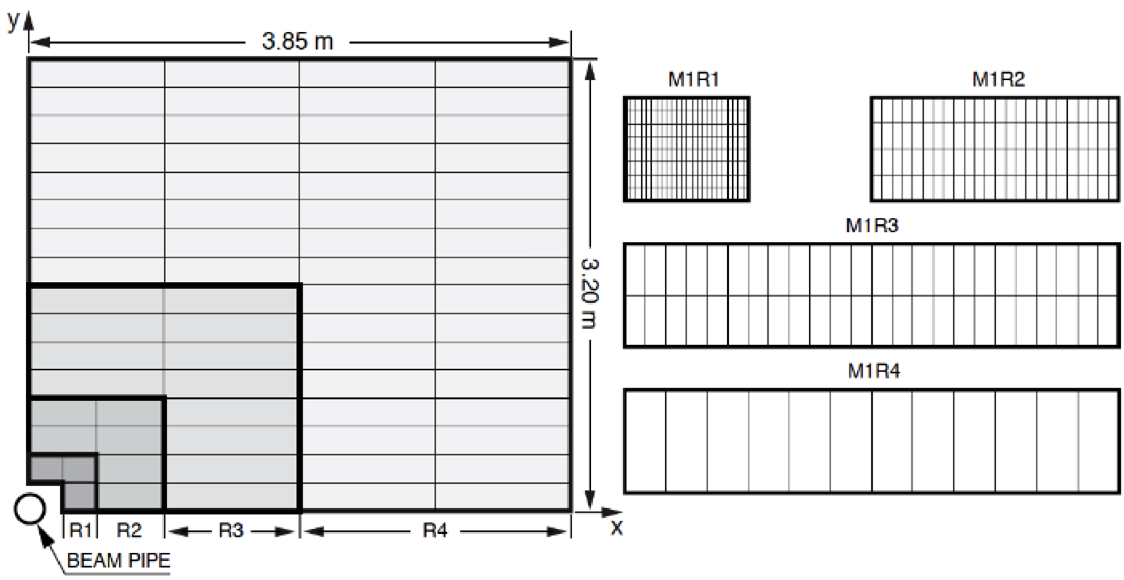

Figure 28: *Front view of one quadrant of the first muon station.*

4 Introduction

Nearly twenty years have passed since the Belle experiment discovered the narrow $X(3872)$ peak in the $\pi^+\pi^- J/\psi$ mass distribution, from $B^{\pm,0} \to K^{\pm,0}\pi^+\pi^- J/\psi$ decays, right at the $D^0\overline{D}^{*0}$ mass threshold [7]. Its narrow width and the coincidence with this threshold have fueled speculations that the $X(3872)$ is not a normal charmonium state but a $D^0\overline{D}^{*0}$ molecule. The $X(3872)$ was later confirmed by the other experiments, produced either in B decays or in prompt production in hadron collisions [18–20]. Its spin and parities were determined to be $J^{PC} = 1^{++}$ [3, 21]. Since no isospin partners are observed, the state is believed to be iso-singlet. As it necessarily contains $c\bar{c}$ among its valence quarks, a state with such quantum numbers is labeled $\chi_{c1}(3872)$, according to the recent PDG naming convention. In this note, we use $\chi_{c1}(3872)$ and $X(3872)$ interchangeably. The first radial excitation of axial vector spin-triplet $c\bar{c}$ state, $\chi_{c1}(2^3P_1)$, is expected with these quantum numbers in this mass range. However, such interpretation is challenged not only by the coincidence with the $D^0\overline{D}^{*0}$ threshold, but also by non-observation of $\pi^0\pi^0 J/\psi$ decays, indicating that the $\pi^+\pi^-$ system in the discovery mode is in isovector state. In fact, from early on, peaking of the $\pi^+\pi^-$ mass distribution towards its upper kinematic limit near 776 MeV, has been suggestive of being dominated by the $\rho^0(770)$ resonance. While it is rare to discover a new state in an isospin violating strong decay, such decays have been observed among charmonium states, with appropriately small rates. For example, the $\psi(2S)$ state decays via isospin conserving $\pi^+\pi^-$ and $\pi^0\pi^0$ transitions to $J/\psi(1S)$ with a total rate of $(54.9 \pm 0.4)\%$, while its rate for the isospin violating decays $\pi^0 J/\psi(1S)$ is more than two-orders of magnitude smaller, $(0.13 \pm 0.03)\%$ [22]. Therefore, it is of key importance to relate $X(3872) \to \pi^+\pi^- J/\psi$ rate to an isospin conserving decay, such as $X(3872) \to \omega J/\psi$. In fact, a well established $\chi_{b1}(2^3P_1)$ state in the bottomonium system is observed to decay to $\omega\Upsilon(1^3S_1)$ with a total rate of $(1.6^{+0.4}_{-0.3})/\%$, but its isospin violating decays have not been observed yet. Its isospin conserving $\pi\pi$ transition rate to $\chi_{b1}(1^3P_1)$ is only $(0.9 \pm 0.1)\%$ [22]. The $\omega(782)$ resonance decays $(89.3 \pm 0.6)\%$ of the time to isospin conserving $\pi^+\pi^-\pi^0$ channel, and $(1.53 \pm 0.06)\%$ of the time to isospin violating $\pi^+\pi^-$. Only the low-mass tail of the relatively narrow ω ($\Gamma = 8.49 \pm 0.08$ MeV) can contribute to the $X(3872)$ decays in the phase-space suppressed region. Nevertheless, the evidence for $X(3872) \to \omega J/\psi$, $\omega \to \pi^+\pi^-\pi^0$ decays was observed a while ago by Belle [23], with a rate of $\mathcal{R}_{\omega/\pi\pi} \equiv \mathcal{BR}(X(3872) \to \omega J/\psi)/\mathcal{BR}(X(3872) \to \pi^+\pi^- J/\psi) = 1.12 \pm 0.45 \pm 0.34$, and by BaBar [24], $\mathcal{R}_{\omega/\pi\pi} = 0.8 \pm 0.3$. More recently BESIII has established $X(3872) \to \omega J/\psi$ decays with $> 5\sigma$ significance at the rate of $\mathcal{R}_{\omega/\pi\pi} = 1.6^{+0.4}_{-0.3} \pm 0.2$ [25]. Averaging the three determinations we obtain $\mathcal{R}_{\omega/\pi\pi} = 1.35 \pm 0.26$. The phase-space suppresses ω relative to ρ^0, assumed to dominate the $\pi^+\pi^- J/\psi$ decays, by about an order of magnitude [26], Thus, leaving the isospin violation in $X(3872) \to \pi^+\pi^- J/\psi$ rate still an order of magnitude too large for X to be an ordinary charmonium state. As pointed out by many authors, such large isospin violation finds a natural explanation in stronger coupling of $X(3872)$ to the $D^0\overline{D}^{*0}$ pairs, than to the D^+D^{*-} pairs which are heavier by 8 MeV, for example via molecular model, making the $\mathcal{R}_{\omega/\pi\pi}$ ratio very important for $X(3872)$ interpretations [27–36].

Naively, from the $X(3872) \to \omega J/\psi$, $\omega \to \pi^+\pi^-\pi^0$ measurements, we can expect ω to be present in $X(3872) \to \pi^+\pi^- J/\psi$ decays at $R_\omega \equiv \mathcal{R}_{\omega/\pi\pi} \cdot \mathcal{BR}(\omega \to \pi^+\pi^-) = 0.021 \pm 0.004$ level. However, the interference with ρ^0 can enhance its overall importance, thus complicating translation of R_ω value to the ratio of isospin violating $(\rho^0 J/\psi)$ to isospin conserving $(\omega J/\psi)$ rates.

The CDF collaboration analyzed dipion mass spectrum with 1260 ± 130 X(3872) candidates from prompt production at the Tevatron [37]. They used Breit-Wigner sum to model the ρ^0-ω interference and found that the ω fit fraction was insignificant, $< 10\%$, but $\rho^0 - \omega$ interference was producing $R_\omega \sim 23\%$ (no errors given). The Belle collaboration also performed the same type of analysis, with 159 ± 15 $X(3872) \to \pi^+\pi^- J/\psi$ candidates reconstructed in the $B^\pm \to X(3872)K^\pm$ decay mode [38]. Since the backgrounds under the $X(3872)$ peak in such exclusive reconstruction are small, sensitivity of Belle's analysis was competitive to the CDF analysis in spite of the smaller $X(3872)$ yield. The ω contribution was insignificant[3] (1.3σ). Including the interference effects[4], $R_\omega \sim (12 \pm 8)\%$.

The LHCb experiment is well suited to look for ω contribution to $X(3872) \to \pi^+\pi^- J/\psi$ decays, because it has the largest sample of exclusively reconstructed $B^\pm \to X(3872)K^\pm$, $X(3872) \to \pi^+\pi^- J/\psi$ decays. Such exclusive reconstruction keeps the backgrounds in check. It also has an excellent mass resolution which becomes important when probing

[3]Estimated by us from the χ^2 difference between the S-wave fits without and with the ω term.

[4]Estimated by us from the event yields given in Table VI in Ref. [38] for the S-wave fit, as $(0.6 + 17.8)/159 \pm \sqrt{0.5^2 + (17.8\,\Delta r_\omega/r_\omega)^2}/159$. The statistical error only.

for the ω tail in the sharply falling $\pi^+\pi^-$ mass spectrum when approaching the upper kinematic bound.

5 Data Selection

The B2XMuMu stripping line[5] is used as a starting point for selection of $B^+ \to J/\psi K^+\pi^+\pi^-$, $J/\psi \to \mu^+\mu^-$ candidates from Run1 and Run2 running periods.[6] The stripping line cuts for this final state, selected as $B^+ \to \mu^+\mu^- K_1^+$, $K_1^+ \to \pi^+\pi^- K^+$ candidates, are summarized in Table 4. We impose additional selection criteria as listed in Table 5. All charged tracks are required to be good quality ($\chi^2_{track} < 4.0$), not clone candidates, and have a low ghost probability ($TRGHP < 0.45$). In addition to muons, also hadron candidates are required to miss the primary pp interaction vertex by three standard deviations ($\chi^2_{\rm IP} > 9.0$). The two oppositely charged muons must form a good secondary vertex ($\chi^2_{\rm vtx}/{\rm ndf}(\mu^+\mu^-) < 9.0$), and must be in the J/ψ mass window ($3040\,\text{MeV} < m_{\mu\mu} < 3140\,\text{MeV}$). Since the stripping lines does not impose hadron ID criteria, we require pion (kaon) candidates to satisfy loose hadron identification criteria, $PIDK < 5$ ($PIDK > -5$). We also require that the kaon candidate is more likely to be a kaon than the two pion candidates ($K\_PIDK > max(Pi1\_PIDK, Pi2\_PIDK)$). In addition to the vertex requirements on the B^+ candidate in the stripping line, we demand that its proper decay time (τ) is larger than 0.25 ps. DecayTreeFitter algorithm is applied to the B^+ candidate to implement the J/ψ mass, which improves the B^+ candidate mass resolution. After the candidate passes B^+ mass cut, we also implement B^+ mass and pointing to PV constraints, to improve sub-system mass resolutions.

Our initial analysis was performed without specific trigger requirements. In this version of the analysis, we have added TOS requirements on Hlt1 and Hlt2 trigger lines, listed in Tab. 6, which has reduced the $X(3872)$ signal yield in the data by only 0.7%.

When there is more than one B^+ candidate in the event, we choose the one with the highest sum of p_T over the two pions, the kaon and the J/ψ. This reduces the $X(3872)$ signal yield in the data by 2.4%. The background under the $X(3872)$ mass peak is reduced by 13%.

The $J/\psi\pi^+\pi^-K^+$ mass distribution for the selected candidates is fitted with double-

[5] The following stripping versions were used v21, v21r1, v24r1, v28r1, v29r2, and v34 for 2011, 2012, 2015, 2016, 2017 and 2018 data, respectively.

[6] We have also investigated FullDSTDiMuonJpsi2MuMuDetached stripping line as a starting point for our data selection, but the gain in $X(3872)$ signal yield was only 14%, on expense of much larger background after simple preselection cuts.

sided Crystal Ball (DSCB) line shape for the signal and a second-order polynomial background. The power-law tail parameters of the DSCB shape, n_1 and n_2 are fixed at 10 (the choice motivated by the simulations). The α_1, α_2, mean, σ and the polynomial coefficients are floating parameters. This leads to $878,186 \pm 1,279$ B^+ signal yield (see Figure.29). After 2σ cut around the B^+ mass, we fit the $J/\psi\pi^+\pi^-$ mass distribution for the $X(3872)$ signal using the same signal and background parameterization and obtain a yield of $6,788 \pm 115$ (see Fig. 30), which is 43 times larger than analyzed by the Belle collaboration in this B^+ decay channel [38]. The α_1, α_2, mean, and σ parameter values from this fit are later used when fitting $X(3872)$ signal in slices of the $\pi^+\pi^-$ mass.

The background under the $X(3872)$ peak (Fig. 30) is about 23% in the $\pm 2\sigma$ mass window. However, a large part of it is the irreducible background from B^+ decays to J/ψ and kaon excitations, with latter decaying to $K^+\pi^+\pi^-$. The background from false B^+ candidates is only about 9.4% as estimated from the fit to B^+ mass distribution after the $X(3872)$ mass cut (see Fig. 31). Since further reduction of the latter background is hardly worth complicating the data selection, especially since the both types of background are subtracted by the fits to $J/\psi\pi^+\pi^-$ mass spectrum, this sample is used in our default analysis. We later pursue multivariate data selection among systematic variations (Sec. 17).

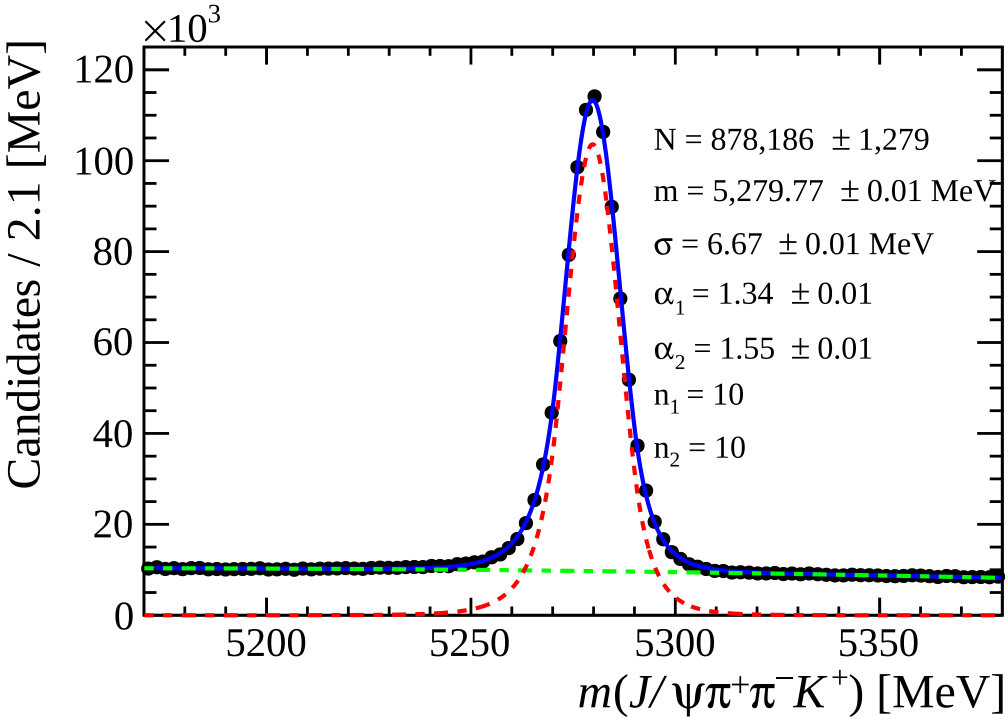

Figure 29: *Fitted $M(J/\psi\pi^+\pi^-K^+)$ mass distribution for $B^+ \rightarrow J/\psi K^+\pi^+\pi^-$ decay with the PV and J/ψ mass constraints. We used DSCB for the signal peak and quadratic polynomial for the background. The blue line represents the total fit, red is the signal component, and the dashed-green is the background.*

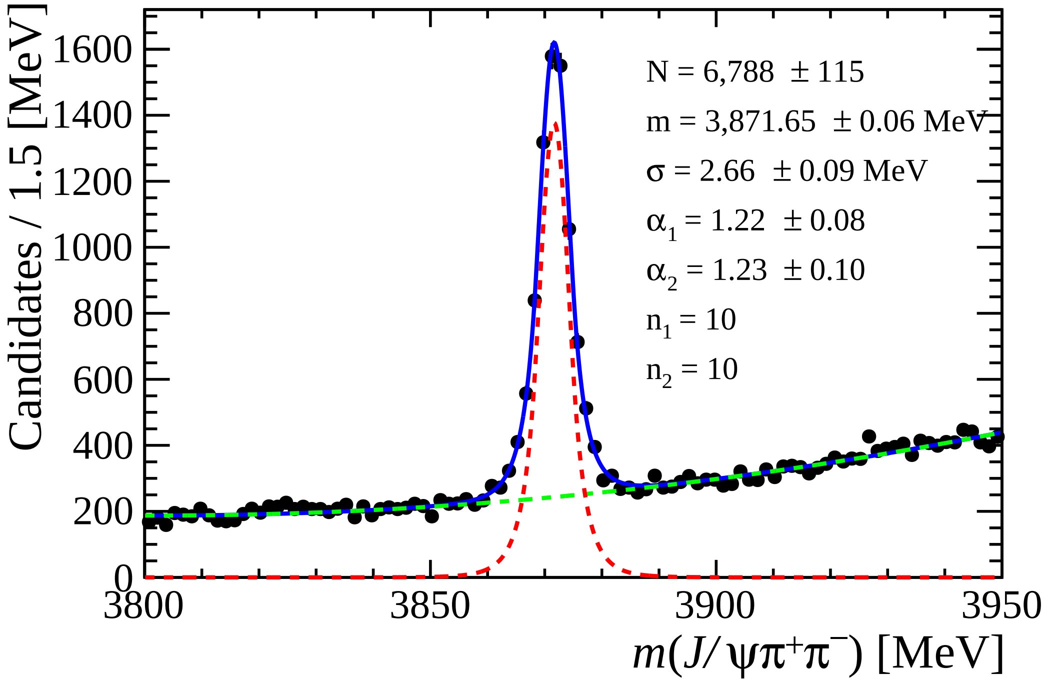

Figure 30: *$M(J/\psi\pi^+\pi^-)$ mass fit with the 2σ B^+ mass signal cut, with the PV, J/ψ and B^+ mass constraints. We used DSCB for the signal peak and quadratic polynomial for the background. The blue line represents the total fit, red is the signal component, and the dashed-green is the background.*

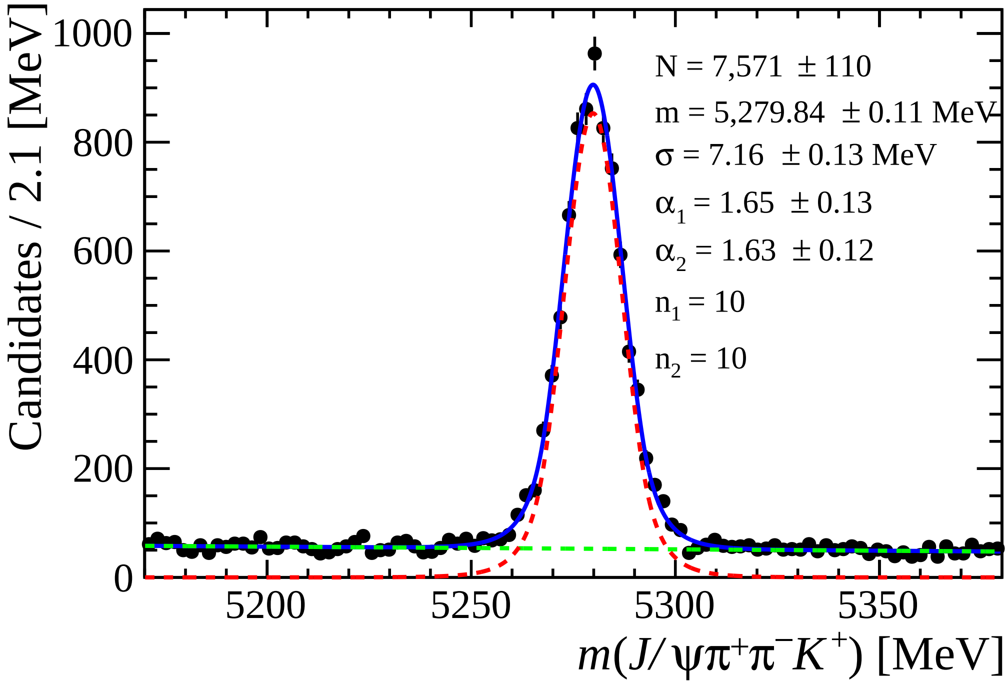

Figure 31: *Fitted $M(J/\psi\pi^+\pi^-K^+)$ mass distribution for $B^+ \to J/\psi K^+\pi^+\pi^-$ decay with the PV, J/ψ mass constraint, and the 2σ $X(3872)$ mass cut. The line blue represents the total fit, red is the signal component, and the dashed-green is the background.*

Table 4: *Stripping line selection (v34).*

Particle	Quantity	Cuts
μ	TRGHP	< 0.5
	MIPCHI2DV(PRIMARY)	> 9.0
	PIDmu	> -3.0
$\mu\mu$	VFASPF(VCHI2/VDOF)	< 12.0
	BPVDIRA	> -0.9
	BPVVDCHI2	> 9.0
Kaon	TRGHP	< 0.5
	MIPCHI2DV(PRIMARY)	> 6.0
	HASRICH	
Pion	TRGHP	< 0.5
	MIPCHI2DV(PRIMARY)	> 6.0
	HASRICH	
Combination12Cut($\pi^+\pi^-K$)	AM	$< 4200.0\,\mathrm{MeV}$
Combination12Cut($\pi^+\pi^-K$)	ACHI2DOCA(1,2)	< 8
K1 i.e. $\pi^+\pi^-K$	(AHASCHILD(MIPCHI2DV(PRIMARY)	> 16.0
K1	ADOCACHI2CUT(20.,”)	
K1	AM	$< 4200\,\mathrm{MeV}$
K1	M	$< 4000\,\mathrm{MeV}$
K1	VFASPF(VCHI2PDOF)	< 8.0
K1	BPVVDCHI2	> 36.0
K1	MIPCHI2DV(PV)	> 4.0
B	AM	$[4800, 7100]\,\mathrm{MeV}$
B	abs(SUMQ)	< 3
B	VFASPF(VCHI2/VDOF)	< 8.0
B	BPVIPCHI2	< 16.0
B	BPVDIRA	> 0.9999
B	BPVVDCHI2	> 121.0
B	MAXTREE(ISBASIC,MIPCHI2DV(PV)	> 9.0

Table 5: *Additional selection criteria. The CloneDist cut listed in the table means that Kullback-Liebler track-clone distance must be greater than* 5000.

Partice	Quantity	Cuts
tracks	$\sim$THASINFO(LHCb.Track.CloneDist)	
	χ^2_{track}/ndf	< 4.0
	TRGHP	< 0.47
	MIPCHI2DV(PRIMARY)	> 9
$\mu^+\mu^-$	VFASPF(VCHI2PDOF)	< 9
	MM	< 3040 MeV
	MM	> 3140 MeV
Pions	χ^2_{track}/ndf	< 4.0
	MIPCHI2DV(PRIMARY)	> 9
	PIDK	< 5
Kaon	χ^2_{track}/ndf	< 4.0
	PIDK	> -5
	PIDK	>PIDK for the π^+, π^-
B	MM	$[5050, 5450]$ MeV
	τ	> 0.25ps

6 Extraction of the dipion mass spectrum

To extract $dN_X/dm_{\pi\pi}$ distribution (N_X is the $X(3872)$ signal yield), we perform a two-dimensional, unbinned fit to $[m_{J/\psi\pi\pi}, m_{\pi\pi}]$ masses in $m_{\pi\pi}$ slices. The $m_{\pi\pi}$ dependence within its slice is needed for an accurate description of the phase-space factor, which becomes important near the upper kinematic boundary.

The $X(3872)$ signal shape is described using Double Sided Crystal Ball function (DSCB). The DSCB the power-law tail parameters, n_1 and n_2, are fixed to 10, as motivated by the fit to the simulated data (Fig. 42). The other parameters of the DSCB function are fixed by a fit to the total $m_{J/\psi\pi\pi}$ distribution with 2σ B^+ mass signal cut (see Figure 30). There is no evidence for variation of the $X(3872)$ mass resolution with the $m_{\pi\pi}$ as

Table 6: *Tigger requirements on B^+ candidates.*

	Run 1	Run 2
L0	Global_DecDecision	
Hlt1 TOS	TrackMuon	
	DiMuonHighMass	
	TrackAllL0	TrackMVA
		TwoTrackMVA
Hlt2 TOS	TopoMu2,3,4Body	
	DiMuonDetachedJPsi	
	DiMuonDetachedHeavy	

illustrated in MC in Fig. 32.

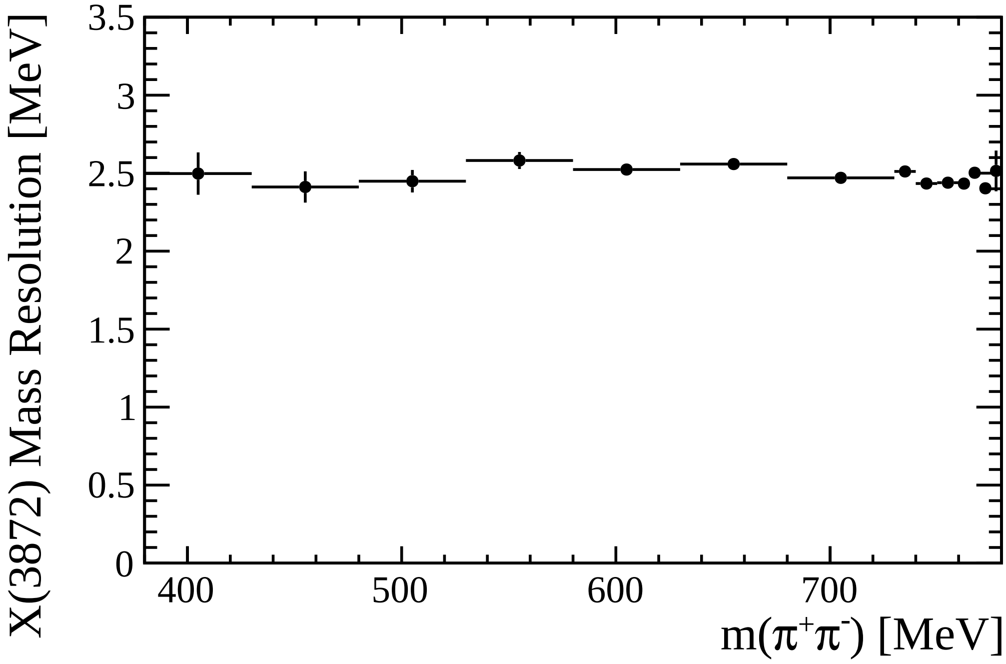

Figure 32: *The $X(3872)$ mass resolution (σ) as obtained by fitting the $J/\psi\pi^+\pi^-$ mass in the signal simulations with the DSCB shape in various $m_{\pi\pi}$ bins.*

The background under the X peak is described with a quadratic function (free parameters in each $m_{\pi\pi}$ bin). Both are multiplied by the phase-space factor, $P_{J/\psi}$, i.e. the momentum of J/ψ in the X(3872) rest frame.[7] The total PDF has the following form:

$$\begin{aligned} PDF(m_{J/\psi\pi\pi}, m_{\pi\pi}) = P_{J/\psi}(m_{J/\psi\pi\pi}, m_{\pi\pi})[N_X DSCB(m_{J/\psi\pi\pi})+ \\ + b_0 + b_1(m_{J/\psi\pi\pi} - m_{X(3872)}) + b_2(m_{J/\psi\pi\pi} - m_{X(3872)})^2] \end{aligned} \tag{1}$$

The signal shape, $P_{J/\psi}(m_{J/\psi\pi\pi}, m_{\pi\pi})\, DSCB(m_{J/\psi\pi\pi})$, is normalized by numerical two-dimensional integration in the fitted phase-space region. We divide the data sample into thirty-five $m_{\pi\pi}$ slices in the interval of [380,780] MeV. To match the rising signal statistics, the $m_{\pi\pi}$-slice width ($\Delta m_{\pi\pi}$) varies from 40 to 5 MeV. We display fit results in the units of signal yield per 5 MeV, thus rescale the fit results via:

$$dN_{X\,i} = \frac{N_{X\,i}}{\Delta m_{\pi\pi i}} \times 5MeV \tag{2}$$

Projections of the 2D fits onto $m_{J/\psi\pi\pi}$ distributions in a sample of various $m_{\pi\pi}$ slices are shown in Fig. 33 (all slices are shown in Appendix B, Figs. 100-102). The obtained $dN_X/dm_{\pi\pi}$ distribution is displayed in Fig. 34.

[7]The momentum of J/ψ in $X(3872)$ rest frame is a function of both $m_{J/\psi\pi\pi}$ and $m_{\pi\pi}$,:

$$P_{J/\psi} = \frac{\sqrt{(m_{J/\psi\pi\pi} - m_{J/\psi} - m_{\pi\pi})(m_{J/\psi\pi\pi} + m_{J/\psi} - m_{\pi\pi})(m_{J/\psi\pi\pi} - m_{J/\psi} + m_{\pi\pi})(m_{J/\psi\pi\pi} + m_{J/\psi} + m_{\pi\pi})}}{2m_{J/\psi\pi\pi}},$$

where $m_{J/\psi}$ is fixed to its PDG value.

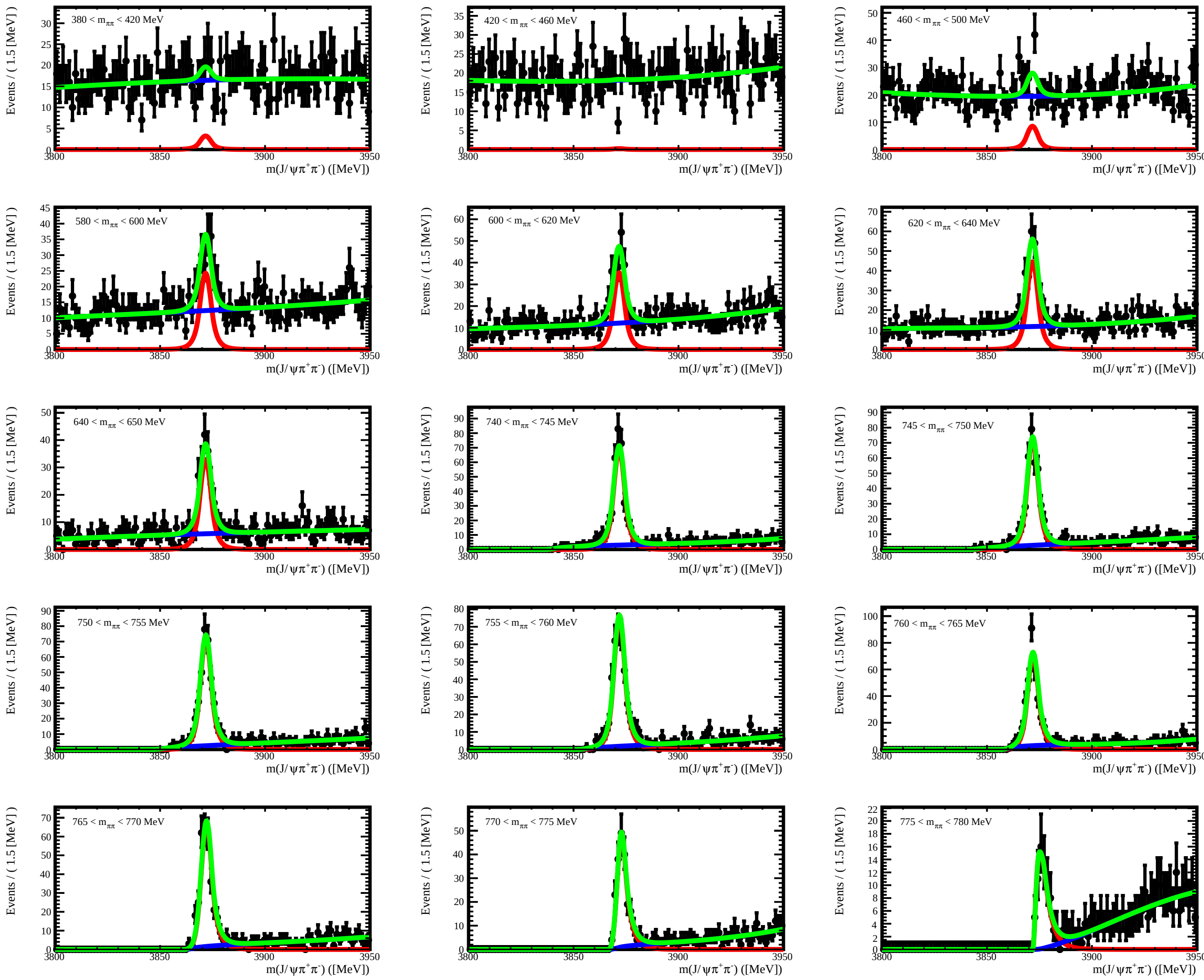

Figure 33: *Projections of unbinned fits to $m_{J/\psi\pi\pi}$ vs. $m_{\pi\pi}$, in different $m_{\pi\pi}$ bins, onto the $m_{J/\psi\pi\pi}$ axis. The total fit, the $X(3872)$ signal and the background components are shown by the green, red and blue lines, respectively.*

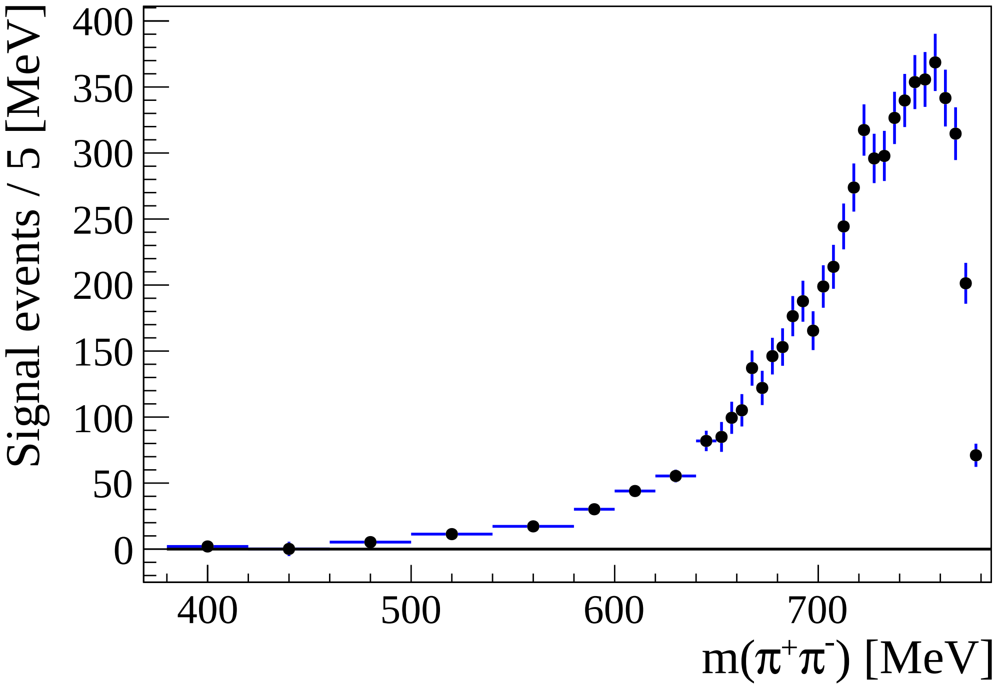

Figure 34: *Extracted dipion mass distribution in* $X(3872) \to \pi^+\pi^- J/\psi$ *decays.*

7 Monte Carlo simulations

To interpret dipion mass spectrum from the $X(3872)$ decays, it is necessary to understand the dipion mass resolution and relative efficiency variation with this mass. We use Monte Carlo (MC) simulations to study these effects.

In total, we used 0.346×10^6 MC events generated for Run 1 and 1.279×10^6 MC events generated for Run 2. The events were generated according to EventType 12145003, in which $B^+ \to K^+X(3872)$, $X(3872) \to J/\psi\rho^0$, $\rho^0 \to \pi^+\pi^-$, $J/\psi \to \mu^+\mu^-$ decays are simulated using the helicity model in which 1^{++} $X(3872)$ decays in S-wave, which describes the angular distributions in the data well [3]. The EvtGen generator handling this EventType does not implement right phase-space factor for broad ρ^0 reaching the kinematic boundaries, and as a consequence, overpopulates dipion mass entries close to the upper mass bound (see Appendix A for more details). This is actually advantageous for this analysis, since we gain more statistics in the dipion mass range, where ω contribution becomes important. As we use simulations only for variation of the resolution and efficiency with dipion mass, we do not depend on the generated dipion mass distribution, thus it does not matter that the MC model does not include ω contribution. When comparing the simulations and data on distributions integrated over the dipion masses, we reweight the MC to the dipion mass distribution as described in Appendix A.

To properly weight different running conditions, we determined the number of reconstructed $X(3872)$ events in the data and in the simulated samples for various running conditions as documented in Table 7. For overall simulation sample, we assign a relative weight to each run period given by the ratio of the reconstructed signal events in the data and in the Monte Carlo. We did not have a dedicated 2011 Monte Carlo sample, thus we assumed that the 2012 Monte Carlo sample adequately represents the combined data set of 2011-2012 data. This is a safe assumption since the difference in 2011 and 2012 pp collision energy ($\sqrt{s}$) is small (7 vs. 8 TeV), and the luminosity ratio is $1:2$. It should be also stressed that we rely on the simulations only for a relative change of the efficiency with dipion mass and not on absolute efficiency values. The dipion mass resolution does not change between 8 and 13 TeV collision energies, as discussed in Sec. 8. The last, but not least, the 2011 data constitutes only 5.5% of the total data sample.

Even though it is not an aim of this analysis to determine any absolute cross-sections, the information given in Table 7 can be used to perform a crude check on how well the simulations track the real data for changes in absolute efficiency with a run period. For that purpose, we calculate efficiency as a ratio of the reconstructed and generated events in the MC. This is not a true absolute reconstruction efficiency, since we do not fold in efficiency of generator level cuts, which may vary slightly with the collision energy. We then calculate visible cross-section (σ_{vis}) for $B^{\pm} \to K^{\pm}X(3872)$, $X(3872) \to J/\psi\rho^0$, $\rho^0 \to \pi^+\pi^-$, $J/\psi \to \mu^+\mu^-$ decays, by dividing the signal yield in the data, by the integral luminosity and such determined efficiency. Within the four 13 TeV data sets, the values are consistent with each other at a p-value of 18%, and average to 22.7 ± 0.4 pb. The ratio of b-quark cross-sections was determined by LHCb to be $R_{\sigma} = 2.14 \pm 0.13$ between 13 TeV and 7 TeV collisions [39]. Assuming that the 2011 and 2012 efficiencies are the same, we calculate 7 TeV visible cross-section in our analysis, and determine this ratio to be 2.04 ± 0.17, in excellent agreement with the proper LHCb measurement quoted above.[8] Assuming that the b-quark cross-section scales linearly with the collision energy between 7 and 13 TeV, we can estimate from R_{σ}, that the expected ratio between visible cross-sections in 2012 (8 TeV) and 2011 (7 TeV) data should be 1.19 ± 0.02, which is again in excellent agreement with 1.18 ± 0.11 determined in our analysis. To summarize this paragraph, the simulations reproduce within the statistical errors, the dependence of overall detection efficiency on running conditions, including the assumption that the efficiency does not change between 2011 and 2012 data.

The reconstructed p_T distribution of B^+ is somewhat harder in the Monte Carlo than in the data, as illustrated in Fig. 35. To extract such distribution in the data we fitted the $X(3872)$ peak in $J/\psi\pi^+\pi^-$ mass distributions for various p_T bins. We fit a smooth correction function to the ratio of the data and MC $p_T(B^+)$ distributions, and apply it as a weight for further use of the simulated events (see Fig. 36). After this correction, agreement between the data and the MC is fairly good for p_T distributions of all final state particles and for the $X(3872)$ helicity angle (Fig. 37).

[8]Our error is statistical only, while the error on R_{σ} is essentially all systematic.

Table 7: *Different LHCb run periods. Number of reconstructed $X(3872)$ signal events in the data and in the MC are given as determined by fits to the reconstructed $J/\psi\pi^+\pi^-$ mass distributions (see Fig. 30 for an example). Efficiency is calculate as a simple ratio between the reconstructed and generated $X(3872)$ events in the MC, and does not include efficiency of generator level cuts. The visible cross-section (σ_{vis}) is calculated by dividing the signal yield in the data, by the integral luminosity and such determined efficiency.*

Year	2011	2012	2015	2016	2017	2018
$\sqrt{s}$ TeV	7	8	13	13	13	13
Lumi fb^{-1}	1.0	2.0	0.3	1.6	1.7	2.1
Data rec.	362 ± 28	851 ± 43	253 ± 21	$1,612 \pm 58$	$1,771 \pm 56$	$1,900 \pm 59$
MC rec.	-	$11,216 \pm 106$	$13,210 \pm 114$	$12,397 \pm 110$	$14,303 \pm 117$	$14,636 \pm 120$
MC gen.	-	346k	313k	280k	327k	359k
eff. (%)	-	3.24 ± 0.01	4.22 ± 0.01	4.43 ± 0.01	4.37 ± 0.01	4.08 ± 0.01
σ_{vis} pb	11.1 ± 0.9	13.1 ± 0.7	20.0 ± 1.7	22.7 ± 0.8	23.8 ± 0.8	22.2 ± 0.7

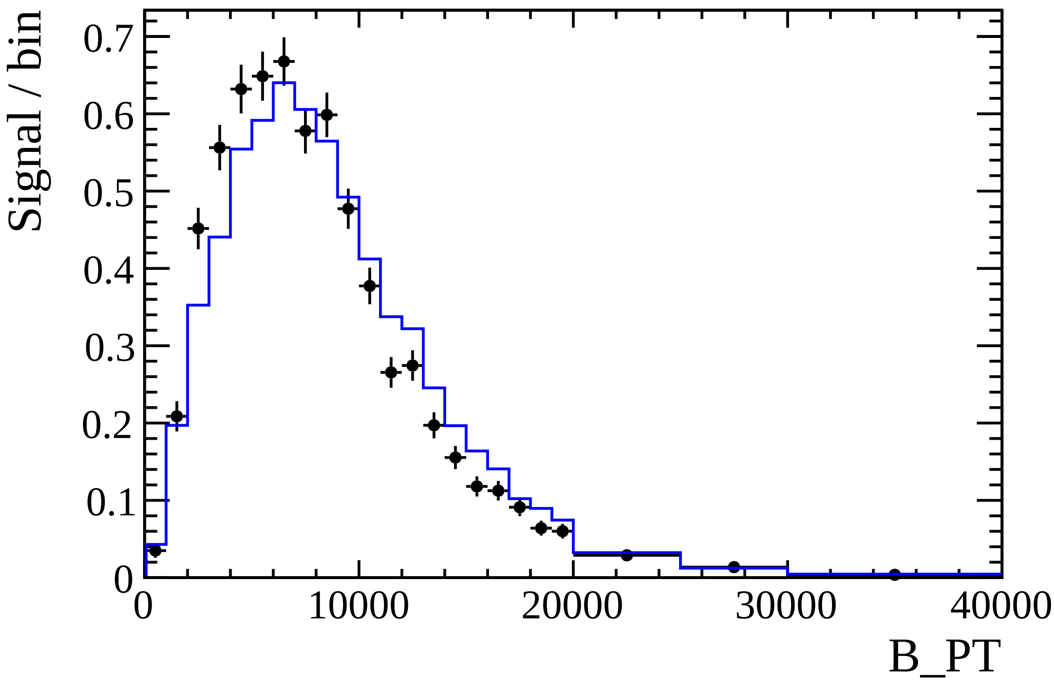

Figure 35: *The distribution of $p_T(B^+)$ for the data (points with error bars) and for the MC (histogram). The distributions were corrected for the varying bin width. The data points were obtained by fitting the $X(3872)$ peak in the $J/\psi\pi^+\pi^-$ mass distributions for various bins. The MC events were weighted by the run-dependent and dipion-mass dependent weights. The MC distribution was normalized to the same number of entries as the data.*

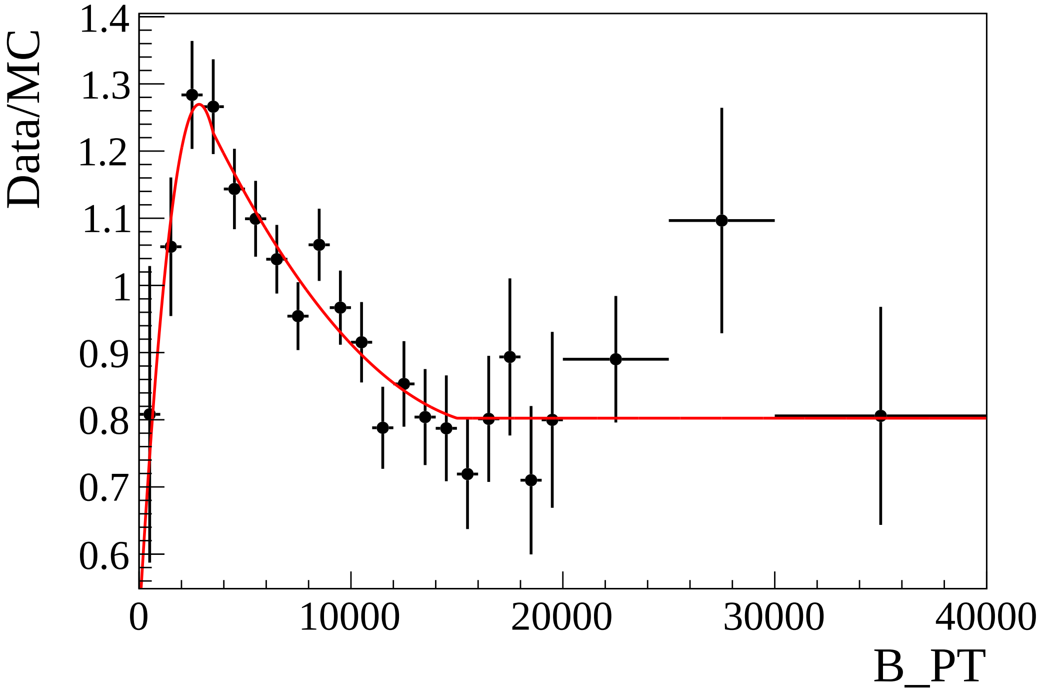

Figure 36: *The ratio of the data and MC distributions of* $p_T(B^+)$ *(Fig. 35), fit with a smooth function used as a correction weight for simulated events.*

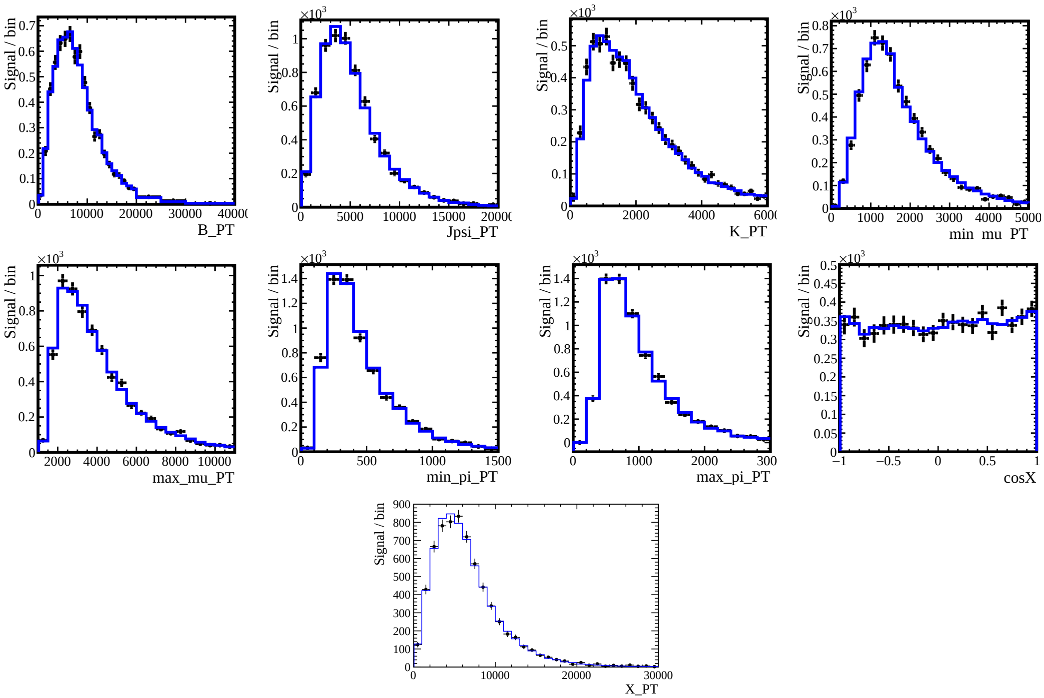

Figure 37: *The distributions of p_T of various reconstructed particles, and of $X(3872)$ helicity angle, for the data (points with error bars) and for the MC (histogram). The distributions were corrected for the varying bin width. The data points were obtained by fitting the $X(3872)$ peak in the $J/\psi\pi^+\pi^-$ mass distributions for various bins. The MC events were weighted by the run-dependent, dipion-mass-dependent and $p_T(B^+)$-dependent weights. The MC distributions were normalized to the same number of entries as the data.*

8 Dipion mass resolution

Using MC truth information, we get $m_{\pi\pi}^{true}$ for reconstructed signal events. For different slices of $m_{\pi\pi}^{true}$, we obtain $m_{\pi\pi}^{reco} - m_{\pi\pi}^{true}$ distribution and fit them with a Gaussian function as shown in Figure 38. Monte Carlo events for different run periods were weighted to properly represent the distribution of the signal yield in real data over these run periods. They were also weighted in $p_T(B^+)$ distribution, as discussed in Sec. 7. The mass slices have different widths to follow increase of the simulation statistics with the mass. The Gaussian σ from each fit is an entry to a distribution of mass resolution shown in Figure 39. The mass resolution increases as the $m_{\pi\pi}$ gets further away from the $2m_\pi$ threshold (279 MeV). It is about 2.2 MeV near the upper kinematic bound, where it plays an important role due to the steep drop in $PDF(m_{\pi\pi})$ imposed by the phase-space factor ($p_{J/\psi} \to 0$). This is also a crucial region for searching for effects due to the tail of the ω resonance, which peaks slightly above the kinematic limit.

To interpolate between bins we fit the obtained mass resolution with the following function,

$$\sigma_m(m) = a_1\,(1 - e^{-\frac{m}{\lambda}}) + a_2\,e^{-\frac{m}{\lambda}}, \tag{3}$$

and obtain $a_1 = 2.39 \pm 0.04$ MeV, $a_2 = -5.4 \pm 1.0$ MeV, and $\lambda = 220.3 \pm 17.2$ MeV. With $\chi^2 = 38.3$ per 39 degrees of the freedom, and a $p-$value of 50%, this function provides excellent description of the simulation results (Fig. 39) and is used in the fits to the dipion mass resolution by smearing theoretical fit functions.

We also show in Figure 40, a comparison between the mass resolution determined in 8 TeV (2012) and 13 TeV (2015-2018) simulation samples. There is essentially no difference.

Monte Carlo is known to underestimate mass resolution somewhat. The B^+ mass resolution in the data is 7.16 ± 0.13 MeV (see Fig. 31), while in MC simulations (Fig. 41) is 6.30 ± 0.04 MeV (14% smaller). The $X(3872) \to J/\psi\pi^+\pi^-$ mass resolution is a better proxy for how well dipion mass resolution is simulated, since the events are constrained to the known J/ψ mass. The fit to the data gives $\sigma_m^{data} = 2.66 \pm 0.09$ MeV (Fig. 30). The fit to the MC gives $\sigma_m^{MC} = 2.47 \pm 0.02$ MeV (Fig. 42). Both are dominated by the resolution, but the natural width can affect them at a couple of percent level. From the average over the two LHCb width determinations, $\Gamma_X^{data} = 1.19 \pm 0.21$ MeV [22]. From the MC truth information, we see that the simulations were performed with the width of $\Gamma_X^{MC} = 0.33$ MeV. Unfolding

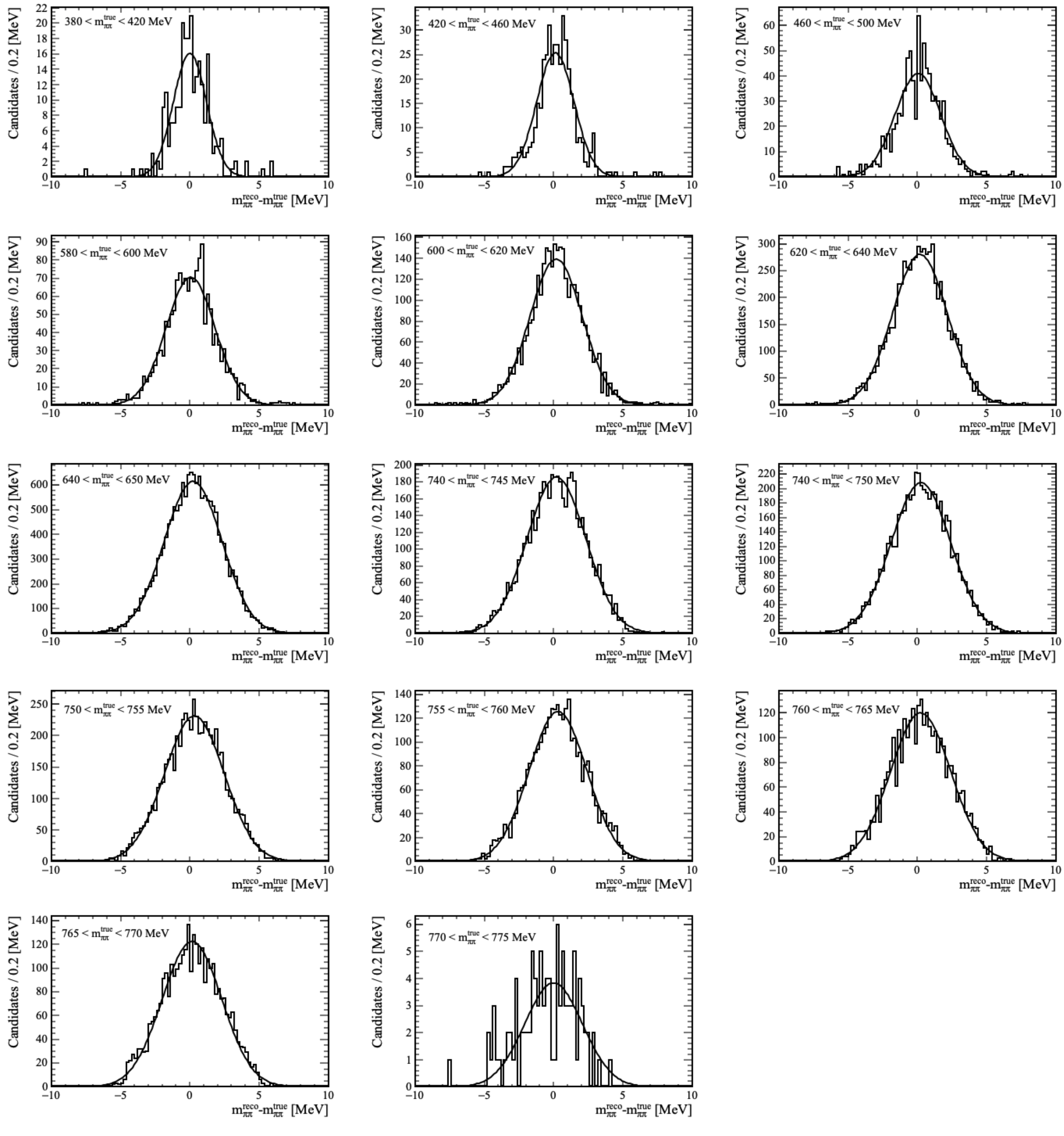

Figure 38: *Fits of Gaussian function to* $m_{\pi\pi}^{reco} - m_{\pi\pi}^{true}$ *distributions in different slices of* $m_{\pi\pi}^{true}$.

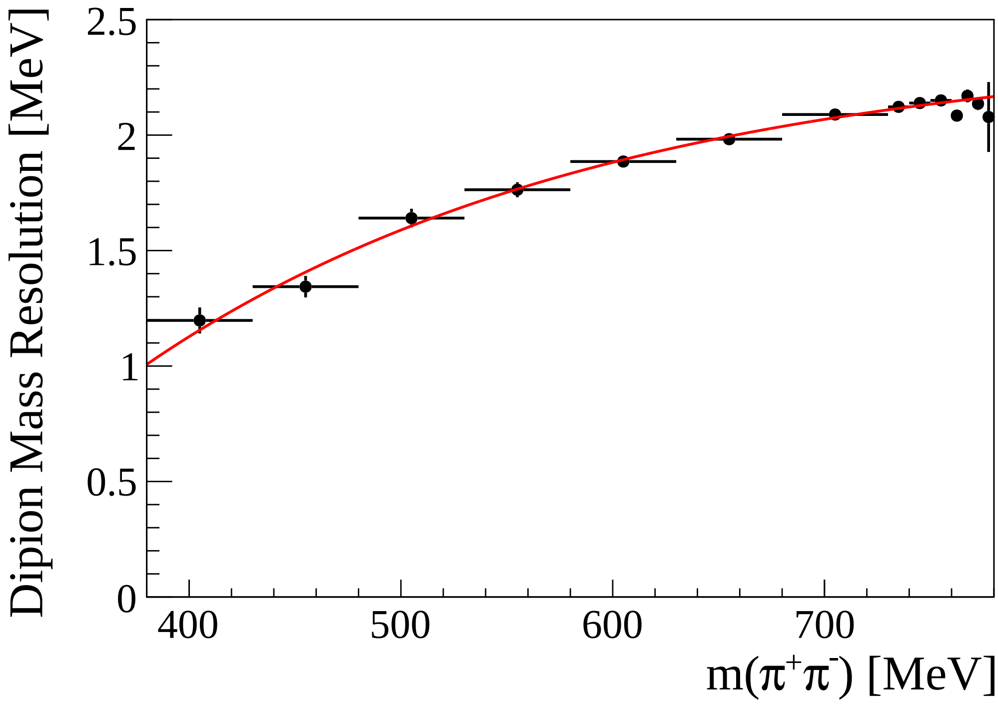

Figure 39: *Dipion mass resolution extracted from the simulations. The red curve is a fit of a smooth function described in the text.*

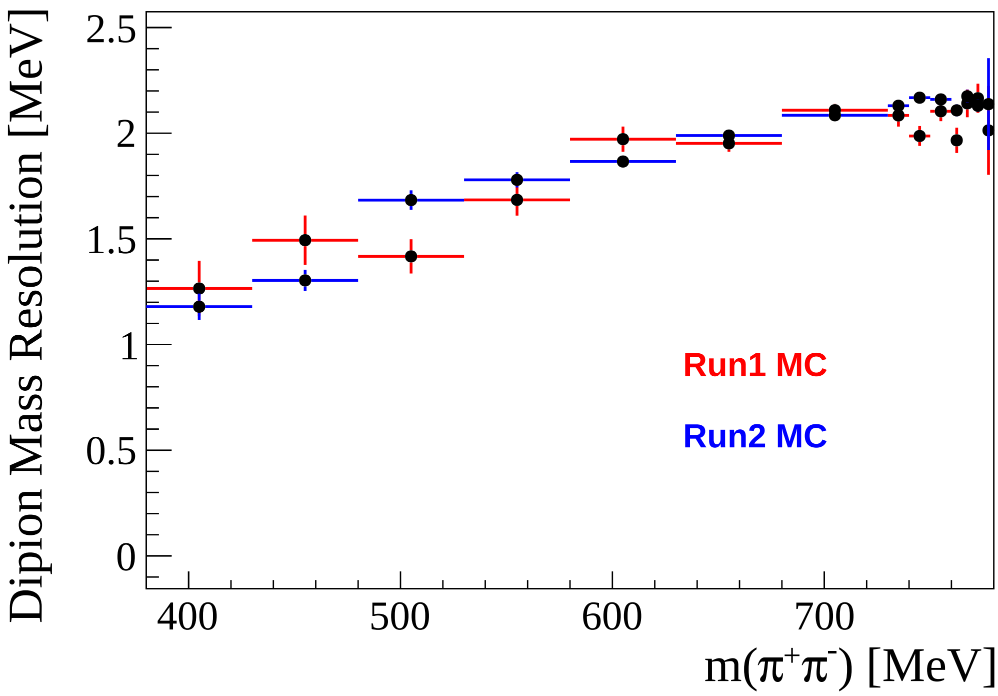

Figure 40: *Dipion mass resolution comparison between 8 TeV (labeled as Run 1) and 13 TeV (Run 2) simulations.*

the natural width effects from the data and MC we obtain the ratio: $\sigma_m^{data\ corr.}/\sigma_m^{MC\ corr.} = \sqrt{\sigma_m^{data\,2} - (\Gamma_X^{data}/2.35)^2}/\sqrt{\sigma_m^{MC\,2} - (\Gamma_X^{MC}/2.35)^2} = (2.61\pm0.10)/(2.47\pm0.02) = 1.06\pm0.04$. We scale the $\pi^+\pi^-$ mass resolution obtained from the simulations up by 1.06. We explore uncertainty in this factor among systematics, by varying it between 1.00 and 1.14.

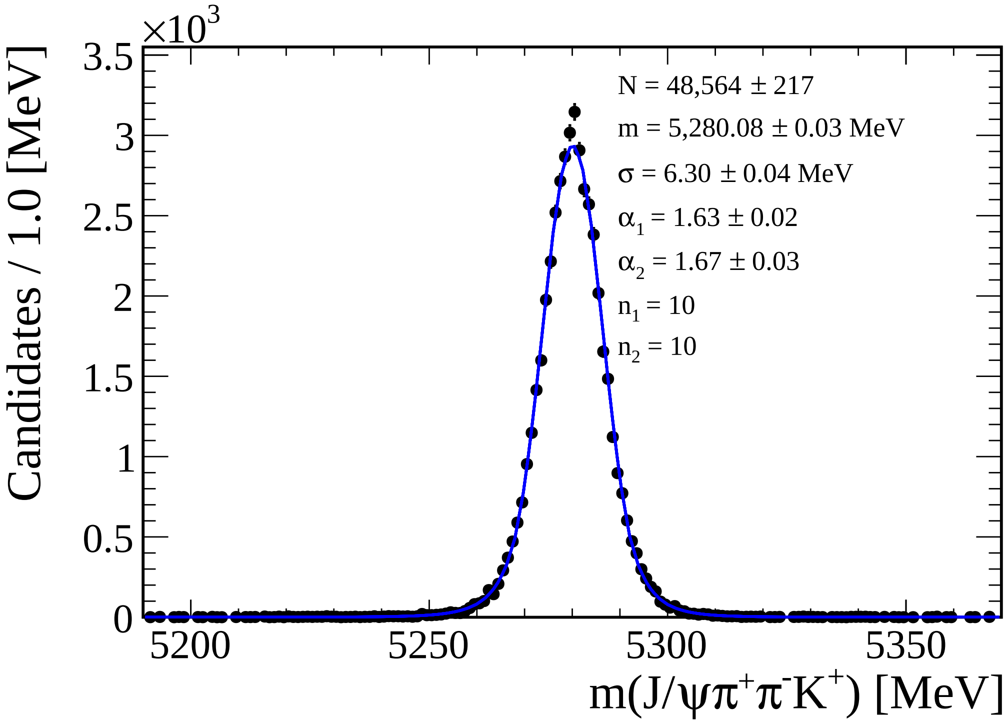

Figure 41: *Fit to the B^+ mass peak (double sided Crystal Ball function) plus a flat background in the simulated $X(3872)$ sample.*

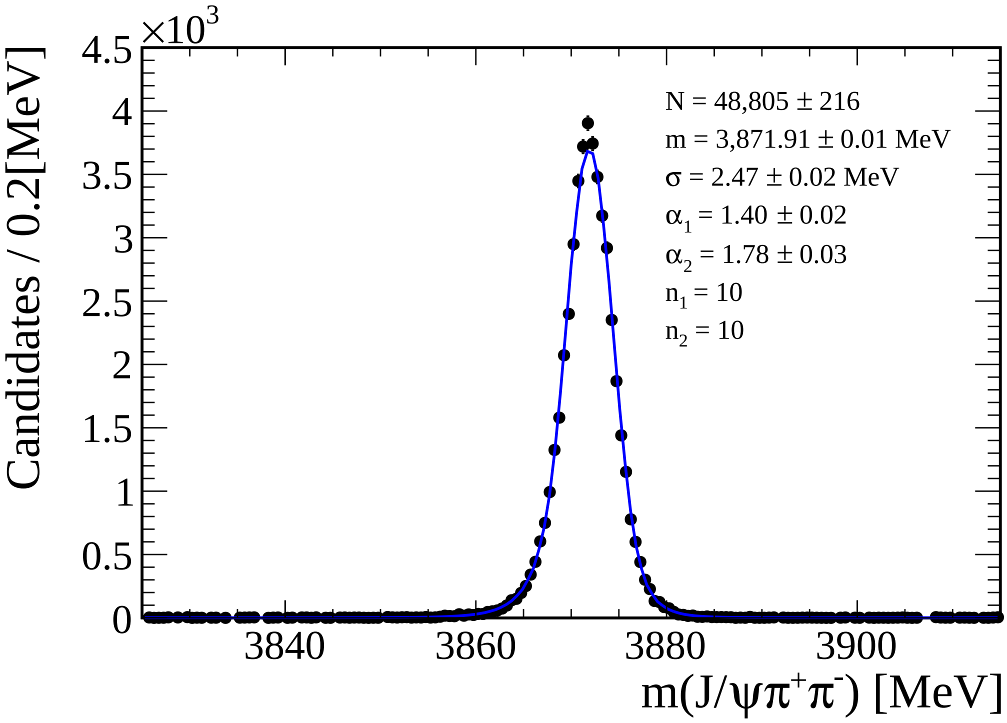

Figure 42: *Fit to the* $J/\psi\pi^+\pi^-$ *distribution in the signal simulations, after the* 2σ B^+ *mass cut, and with the PV,* J/ψ *and* B^+ *mass constraints. We used DSCB for the signal peak and flat background. The blue line represents the total fit. The fitted background level is only* 2.8 ± 0.5 *events per bin. The signal shape parameters are:* $48,805 \pm 216$ *signal events,* $m = 3,871.91 \pm 0.01$ *MeV,* $\sigma = 2.47 \pm 0.02$ *MeV,* $n_1 = n_2 = 10$ *(fixed),* $\alpha_1 = 1.40 \pm 0.02$*, and* $\alpha_2 = 1.78 \pm 0.03$*.*

9 Efficiency variation with the dipion mass

For relative variation of reconstruction efficiency with the dipion mass, we divided the distribution of reconstructed mass in simulations, by the generated one, after we had smeared the generated mass with the mass resolution determined as described in the previous section. The result is shown in Fig. 43. We parameterize this variation with a quadratic function (also shown), which multiplies any theoretical function fit to the dipion mass distribution in the data. In evaluation of systematic uncertainties, we use cubic polynomial instead (Fig. 44).

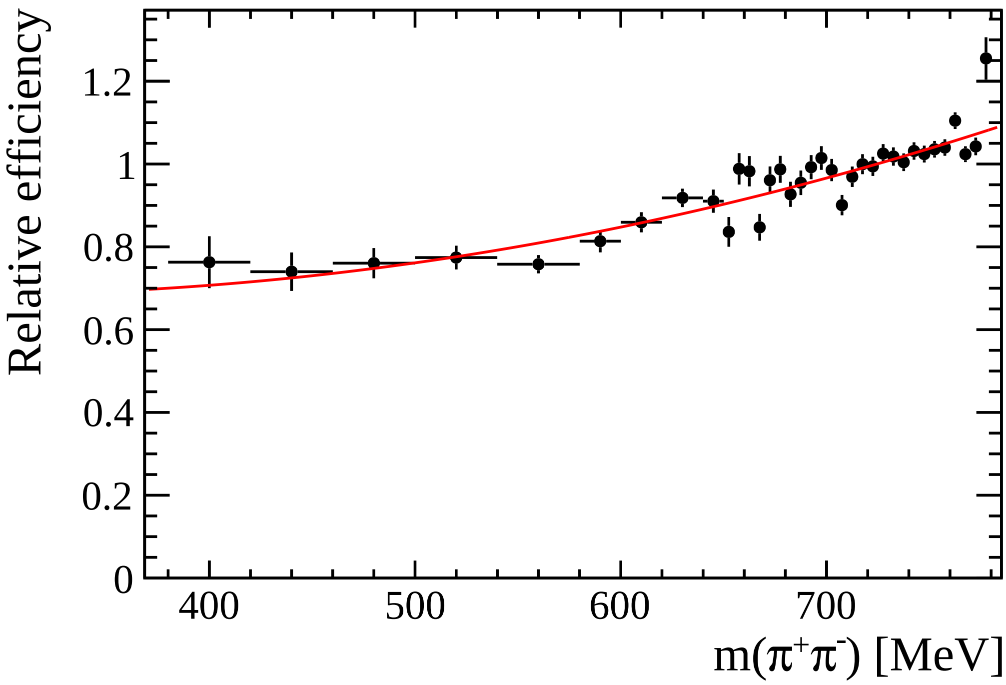

Figure 43: *Variation of the reconstruction efficiency with dipion mass. Units of efficiency are arbitrarily chosen to be close to 1 near 700 MeV, as only the relative variation matters in this analysis. Quadratic fit function is superimposed:* $\epsilon(m_{\pi\pi}) = 0.966 + 1.345 \cdot 10^{-3}\,(m_{\pi\pi} - 700\,MeV) + 1.607 \cdot 10^{-6}\,(m_{\pi\pi} - 700\,MeV)^2$*, where* $m_{\pi\pi}$ *is in MeV.*

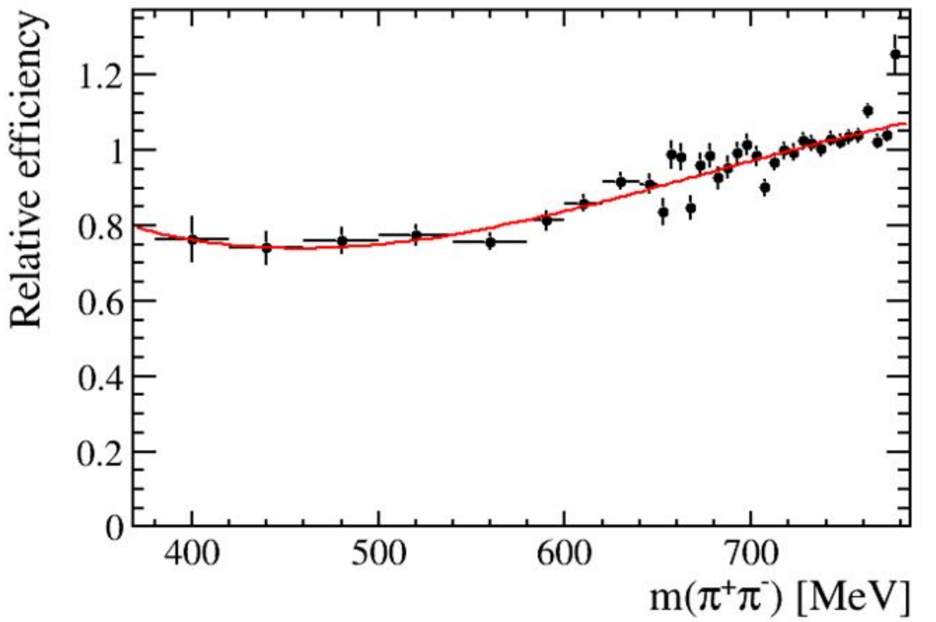

Figure 44: *Variation of the reconstruction efficiency with dipion mass fit to a cubic polynomial.*

10 Fits of Breit-Wigner amplitudes to the $\pi^+\pi^-$ mass distribution

Any theoretical probability density function to be fit to the data, $PDF(m_{\pi\pi})$, is multiplied by the relative efficiency variation with the mass (Sec. 9) and smeared with the mass resolution (Sec. 8).

A relation of a theoretical matrix element, M, to the PDF fit to the data is,

$$PDF(m_{\pi\pi}) = S\, p_{J/\psi}\, p\, |M|^2 \,, \tag{4}$$

where $p_{J/\psi}$ is the J/ψ momentum in the $X(3872)$ rest frame, p is the pion momentum in the ρ^0 rest frame, and S is a scale factor between the unnormalized PDF and the data. The scaling factor is always a free parameter in fits to the data, and its value is not of physics interest.

All fits to the data are minimal χ^2 fits. While some mass bins have very low signal yield, the errors on these yields are Gaussian, since they come from the fits subtracting the backgrounds under the $X(3872)$ peak in the $\pi^+\pi^- J/\psi$ distributions (Sec. 6).

We first attempt to fit ρ^0 resonance alone, represented by a following Breit-Wigner amplitude,

$$\begin{aligned}
M = BW_\rho(m_{\pi\pi}|m_\rho, \Gamma_\rho) &= \frac{m_\rho \Gamma_\rho F_1(p, p_\rho)}{{m_\rho}^2 - m_{\pi\pi}^2 - i\, m_\rho \Gamma_\rho(m_{\pi\pi})}, && (5)\\
\Gamma_\rho(m_{\pi\pi}) &= \Gamma_\rho \frac{p}{p_\rho} \frac{m_\rho}{m_{\pi\pi}} F_1(p, p_\rho)^2, && (6)\\
F_1(p, p_\rho) &= \sqrt{\frac{B_1(p)}{B_1(p_\rho)}}, && (7)\\
B_1(p) &= p^2 \frac{1}{1 + (R\, p)^2}, && (8)\\
p_\rho &= p(m_\rho), && (9)
\end{aligned}$$

where m_ρ and Γ_ρ, are ρ^0 mass and width, which are fixed to the PDG values: 775.26 ($\pm$0.23) MeV and 147.4 ($\pm$0.8) MeV, respectively [22]). This form assumes the $S-$wave $\chi_{c1}(3872) \to \rho^0 J/\psi$ decay, as well motivated by the previous analysis of the angular correlations [3]. The $B_1(p)$ is the Blatt-Weisskopf barrier factor for P-wave decay of a vector particle (here ρ^0) to $\pi^+\pi^-$, and contains an effective hadron-size parameter R, which we fix to a value motivated by the $\pi\pi$ scattering data, 1.45 GeV $^{-1}$ (see Sec. 12).

The scaling factor S (Eq. 4) is the only free parameter in the fit. The fit fails miserably, with a χ^2 per number of degrees of freedom (χ^2/NDoF) equal to 366.6/34, which has p-value (pV) of 2×10^{-57}. The fit is displayed in Fig. 45.

Fitting the mass and width of the ρ^0 resonance, improves the fit ($\chi^2/\mathrm{NDoF} = 48.9/32$, $pV = 0.028$), however gives the mass and width values which are way outside what can be considered reasonable: $m_\rho = 782.9 \pm 3.5$ MeV, $\Gamma_\rho = 96.4 \pm 2.5$ MeV.

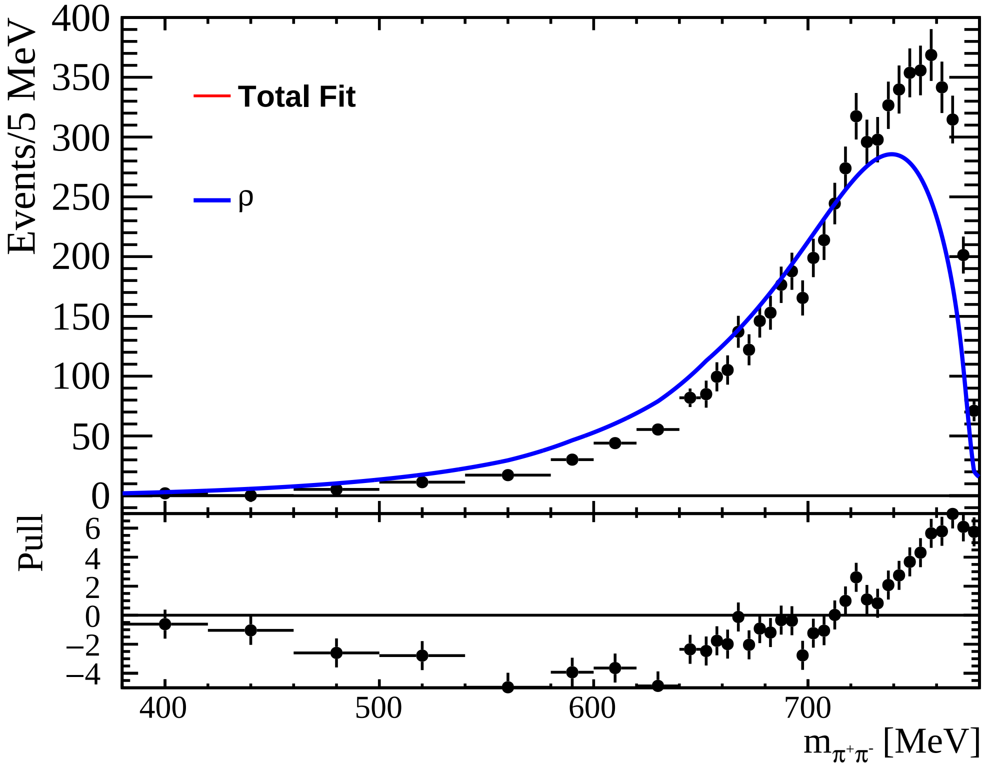

Figure 45: *Fit of ρ^0 Breit-Wigner amplitude to the data. The pulls shown below are the data points minus the fit function value, divided by the error on the data. The fit qualities are* $\chi^2/\mathrm{NDoF} = 366.6/34$ *and* $pV = 2 \times 10^{-57}$.

In the next step, we try the matrix element model previously employed by the CDF [37] and Belle [38] to fit $m_{\pi\pi}$ distribution from $X(3872) \to J/\psi\pi\pi$ decays, which takes a sum over ρ^0 and ω Breit-Wigners,

$$M = BW_\rho(m_{\pi\pi}|m_\rho, \Gamma_\rho) + A_\omega\, e^{i\,\phi}\, BW_\omega(m_{\pi\pi}|m_\omega, \Gamma_\omega), \tag{10}$$

where A_ω and ϕ are relative magnitude and phase of the ω contribution with respect to the dominant ρ^0 term. The mass and width of ω are fixed to the central values of the PDG averages, $\mathrm{m}_\omega = 782.66\ (\pm 0.13)$ MeV, $\Gamma_\omega = 8.68\ (\pm 0.13)$ MeV [22]. The fits to the data are insensitive to the phase value, as long as it is in 90-170 degree range. We fix it to 95^0, the value previously used by the CDF and Belle and motivated by the other measurements [37, 38]. The fit quality is improved substantially relative to ρ^0 contribution alone, $\chi^2/\mathrm{NDoF} = 102.9/33$, but it is still unacceptably low $pV = 4 \times 10^{-9}$ (see Fig. 46).

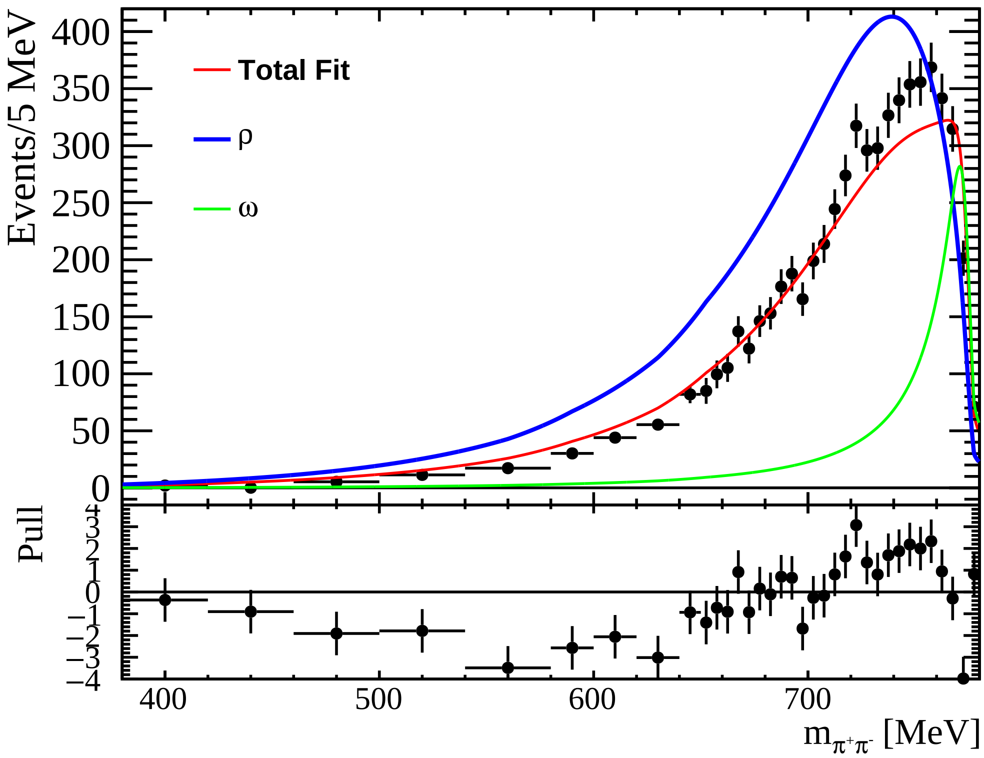

Figure 46: *Fit of a sum of Breit-Wigner amplitude for ρ^0 and ω. The total fit is shown by the red line. Individual contributions are shown by the blue and green lines respectively. In this model they interfere destructively except for the highest mass bins. The fit qualities are* $\chi^2/\mathrm{NDoF} = 102.9/33$ *and* $pV = 4 \times 10^{-9}$.

It is well known that summing Breit-Wigner amplitudes has theoretical drawbacks, especially for strongly overlapping resonances with the same quantum numbers, since it leads to a matrix element which is not unitary, violating first principles of scattering theory. In the next section, we develop a more sophisticated theoretical approach.

11 Coupled-channel model

While looking for models that can describe the data well, we had first tried single-channel K-matrix approach, with ρ^0 and ω poles coupling to the $\pi^+\pi^-$ channel. Such model is able to describe the data well, if we also allow for a small contribution which does not vary much within the fitted range, either a non-resonant term, or the tail of the ρ' resonance. However, we have settled on a K-matrix model, which is theoretically more appealing, with a proper two-channel K-matrix coupling the $\pi^+\pi^-$ and $\pi^+\pi^-\pi^0$ channels. While ρ^0 pole couples only to the $\pi^+\pi^-$ channel, ω pole couples mostly to the $\pi^+\pi^-\pi^0$ channel, but also has a rare isospin violating decay to $\pi^+\pi^-$ channel. This generates, a small off-diagonal couplings between these two channels of opposite G-parity. The K-matrix is given by,

$$K = \frac{1}{{m_\rho}^2 - s} \begin{pmatrix} {g_{\rho\to 2\pi}}^2 & 0 \\ 0 & 0 \end{pmatrix} + \frac{1}{{m_\omega}^2 - s} \begin{pmatrix} {g_{\omega\to 2\pi}}^2 & g_{\omega\to 2\pi}\, g_{\omega\to 3\pi} \\ g_{\omega\to 2\pi}\, g_{\omega\to 3\pi} & {g_{\omega\to 3\pi}}^2 \end{pmatrix}, \tag{11}$$

where $s = m^2_{\pi\pi}$, and g are the coupling constants discussed later. The T-matrix is obtained from,

$$\hat{T} = [1 - i\, K\, \rho]^{-1}\ K, \tag{12}$$

where the phase-space matrix ρ is diagonal,

$$\rho = \begin{pmatrix} \rho_{2\pi}(s) & 0 \\ 0 & \rho_{3\pi}(s) \end{pmatrix}. \tag{13}$$

We choose a notation in which the Blatt-Weisskopf barrier factors are integrated with the phase-space matrix[9], thus

$$\rho_{2\pi}(s) = \frac{2p}{\sqrt{s}}\, B_1(p), \tag{14}$$

$$p(s) = \frac{1}{2}\sqrt{s - (2m_\pi)^2}. \tag{15}$$

A naive implementation of $\rho_{3\pi}(s)$ element, assumes symmetric decay to three pions,

$$\begin{aligned} \rho_{3\pi}(s) &= \frac{2p_3}{\sqrt{s}}\, B_1(p_3), \\ p_3(s) &= \frac{1}{3}\sqrt{s - (3m_\pi)^2}. \end{aligned} \tag{16}$$

[9]Alternatively, they can be attached to the K-matrix elements. Both approaches lead to the same fits.

A better implementation, models the decay to three pions via P-wave decay to $\rho\pi$, as in fact observed for the ω decay,

$$\begin{aligned} \rho_{3\pi}(s) &= \int_{(2m_\pi)^2}^{(\sqrt{s}-m_\pi)^2} d\sigma \frac{2p(\sigma)}{\sqrt{\sigma}} \frac{B_1(p(\sigma))}{({m_\rho}^2-\sigma)^2+(m_\rho\,\Gamma_\rho)^2} \frac{2p_3'(s,\sigma)}{\sqrt{s}}\, B_1(p_3'(s,\sigma)) &(17)\\ p_3'(s,\sigma) &= \frac{[(s-(\sqrt{\sigma}+m_\pi)^2)(s-(\sqrt{\sigma}-m_\pi)^2)]^{1/2}}{2\sqrt{s}} &(18) \end{aligned}$$

We use the latter formula, though the naive formula gives almost identical results, as $\rho_{3\pi}(s)$ affects only the tail of the ω resonances, which is relatively short due to its narrow width. For a comparison of the two $\rho_{3\pi}(s)$ shapes see Fig. 47.

We take Q-vector approach to the production of these two channels in $X(3872)$ decays. The decay amplitudes are given by,

$$\begin{pmatrix} \hat{A}_{2\pi} \\ \hat{A}_{3\pi} \end{pmatrix} = \hat{T} \begin{pmatrix} \alpha_{2\pi} \\ \alpha_{3\pi} \end{pmatrix}, \tag{19}$$

where the elements of the production vector ($\alpha_{2\pi}$, $\alpha_{3\pi}$) are real and subject of the fit to our data. Only the $\hat{A}_{2\pi} = \alpha_{2\pi}\hat{T}_{2\pi,2\pi} + \alpha_{3\pi}\hat{T}_{2\pi,3\pi}$ amplitude matters for this analysis,

$$M = \hat{A}_{2\pi}\sqrt{B_1(p)}. \tag{20}$$

The couplings constants are fully determined by the other experiments,

$$\begin{aligned} g^2_{\rho\to 2\pi} &= m_\rho\,\Gamma_\rho/\rho_{2\pi}(m^2_\rho), &(21)\\ g^2_{\omega\to 3\pi} &= m_\omega\,\Gamma_\omega\mathcal{B}(\omega\to 3\pi)/\rho_{3\pi}(m^2_\omega), &(22)\\ g^2_{\omega\to 2\pi} &= m_\omega\,\Gamma_\omega\mathcal{B}(\omega\to \pi^+\pi^-)/\rho_{2\pi}(m^2_\omega), &(23) \end{aligned}$$

where $\mathcal{B}(\omega\to 3\pi) = (89.2\pm 0.7)\%$, and $\mathcal{B}(\omega\to\pi^+\pi^-) = (1.53\pm 0.12)\%$ [22].

Numerically, $g^2_{\omega\to 2\pi}/g^2_{\rho\to 2\pi} \sim 0.0009$, while $g_{\omega\to 2\pi}\,g_{\omega\to 3\pi}/g^2_{\rho\to 2\pi} \sim 0.01$. Thus, the diagonal ω coupling to 2π can be neglected in comparison to the off-diagonal coupling. In this excellent approximation,

$$\hat{T}_{2\pi,2\pi} \approx \frac{g^2_{\rho\to 2\pi}}{{m_\rho}^2 - s - i\,g^2_{\rho\to 2\pi}\rho_{2\pi}(s)}, \tag{24}$$

is simply the ρ^0 Breit-Wigner amplitude, and $\alpha_{2\pi}$ is the ρ^0 production factor in the $X(3872)$ decay. In the simplest approach, $\alpha_{2\pi}$ can be taken as a constant. However, a slight s-dependence of this factor is possible. Therefore, we allow polynomial dependence on s. It is convenient to use Chebyshev polynomials (C_n) as a basis,

$$\alpha_{2\pi}(s) = \sum_{n=0}^{n=N} P_n \, C_n(\hat{s}), \tag{25}$$

since they are orthogonal to each other, and properly normalized, where[10]

$$\hat{s} = 2\,\frac{s - s_{min}}{s_{max} - s_{min}} - 1, \tag{26}$$

$$C_0(\hat{s}) = 1, \tag{27}$$

$$C_1(\hat{s}) = \hat{s}, \tag{28}$$

$$C_2(\hat{s}) = 2\hat{s}^2 - 1. \tag{29}$$

A numerical value of P_n from a fit to the data, reflects relative importance of the n^{th} order term. Since the scaling factor S already takes care of scaling the fit model to the data, $P_0 = 1$. For the results to have the expected physical behavior, we can check that the series is converging, $|P_{n+1}| < |P_n|$, and that the maximal order to obtain a good fit to the data, N, is small.

The ω contribution enters via,

$$\hat{T}_{2\pi,3\pi} \approx \frac{g_{\omega\to 2\pi}\, g_{\omega\to 3\pi}\,(m_\rho^2 - s)}{({m_\rho}^2 - s - i\, g^2_{\rho\to 2\pi}\rho_{2\pi}(s))({m_\omega}^2 - s - i\, g^2_{\omega\to 3\pi}\rho_{3\pi}(s))}. \tag{30}$$

This term becomes zero at the ρ^0 pole, which is an artifact of the K-matrix approach, which is particularly inconvenient since this is in the region of the interest for the ω contribution. Since the bare mass does not have physical meaning and can be shifted arbitrary, the zero does not need to be enforced there. To remove it and restore more physical behavior of the ω term, we set

$$\alpha_{3\pi} = A\,\frac{1}{{m_\rho}^2 - s}. \tag{31}$$

While in principle A can have polynomial dependence on s, in practice, the ω resonance is so narrow, that the data are completely insensitive to it. Therefore, A (denoted also as A_ω) is made constant in the fits to the data. Its value controls a relative importance of the ω term, with respect to the dominant ρ^0 contribution.

[10]We fix $s_{min} = 380^2$ MeV^2 and $s_{max} = 775^2$ MeV^2 in all fits.

Using Eqs. 24, 30 and 31, with $\alpha_{2\pi}$ constant ($N = 0$), is the popular way to describe $\rho^0 - \omega$ interference in various analyses of the $\pi^+\pi^-$ system (see Sec. 21). We perform our fits, using the exact K-matrix formulae, even though the results are almost identical when using the approximation given by Eqs. 24 and 30 (see Sec. 22).

The subject of our analysis is to establish if a model with ρ^0 and ω can describe the data well, determine significance of the ω contribution, and quantify the latter numerically.

In view of Eq. 24, we interpret $\alpha_{3\pi} = 0$ models as containing ρ^0 only. The χ^2 difference between fits with $\alpha_{3\pi}$ set to zero, or allowed to vary, serves determination of the ω significance.

To quantify a relative rate of the ω contribution, we calculate the following integrals[11],

$$I_{tot} = \int_{s=(2m_\pi)^2}^{s=(m_{X(3872)}-m_{J/\psi})^2} ds\, PDF(s) \tag{32}$$

$$I_\rho = \int_{s=(2m_\pi)^2}^{s=(m_{X(3872)}-m_{J/\psi})^2} ds\, PDF(s\,|\,\alpha_{3\pi}=0) \tag{33}$$

$$I_\omega = \int_{s=(2m_\pi)^2}^{s=(m_{X(3872)}-m_{J/\psi})^2} ds\, PDF(s\,|\,\alpha_{2\pi}=0). \tag{34}$$

A measure of ω contribution, which includes all $\rho^0 - \omega$ interference effects, is obtained from

$$R_\omega^{all} \equiv 1 - \frac{I_\rho}{I_{tot}}. \tag{35}$$

A stripped down version, which excludes interference between the $\hat{T}_{2\pi,2\pi}$ and $\hat{T}_{2\pi,3\pi}$ terms, is defined as

$$R_\omega^{0} \equiv \frac{I_\omega}{I_{tot}}. \tag{36}$$

Finally, we also define the most convenient ratio for quantifying the ratio of isospin violating and conserving couplings,

$$R_{\omega/\rho}^{0} \equiv \frac{I_\omega}{I_\rho}. \tag{37}$$

To propagate fit errors to these quantities, we perform statistical simulations, in which the fit parameters are fluctuated according to the multidimensional (in case of more than one theory parameter fit to the data) Gaussian distribution, which takes the fit values and the fit covariance matrix into account. For each set of the fit parameter values, the R_ω^{all}, R_ω^{0} and $R_{\omega/\rho}^{0}$ are recalculated. Their RMS spreads over many iterations are taken as their statistical errors.

[11] The $PDF(s)$ is not smeared with the mass resolution, nor multiplied by the efficiency function.

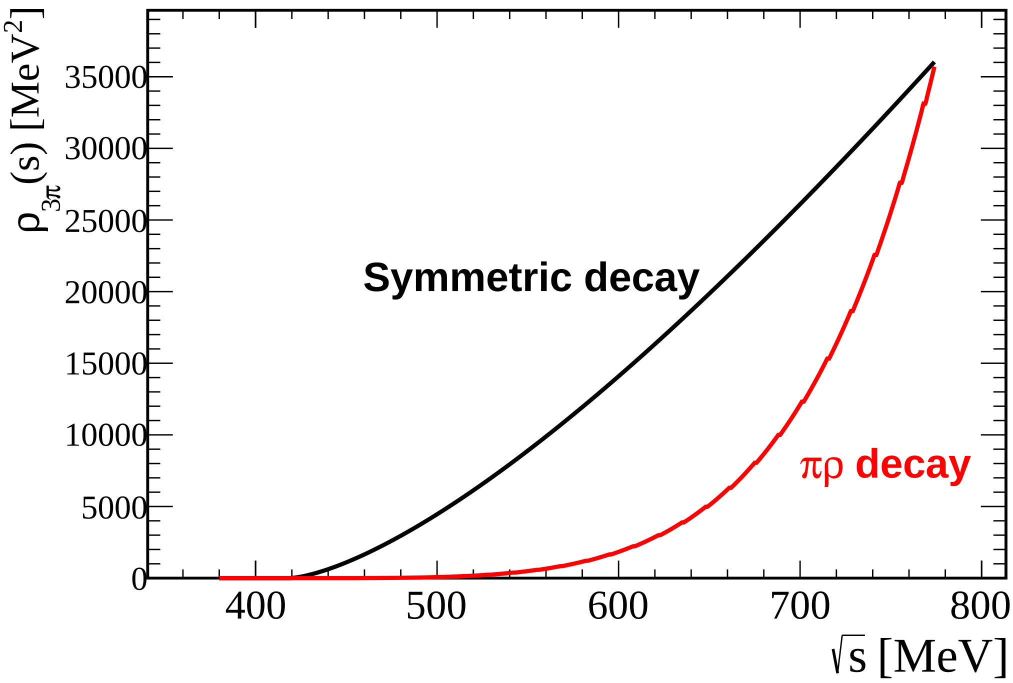

Figure 47: *Two different models of* 3π *P-wave phase space.*

12 Matching the amplitude model to known $\pi^+\pi^-$ phase shifts

The effective hadron size parameter, R, appearing in the Blatt-Weisskopf momentum barrier factor (Eq. 8), in the Breit-Wigner amplitude can be constrained from the data from scattering experiments. This parameter also appears in the coupled-channel model (Eqs. 14, 17 and 20). In fact, the coupled channel model reduces to the ρ^0 Breit-Wigner amplitude, when the ω contribution is eliminated.

The isovector P-wave $\pi^+\pi^-$ interactions are elastic below 1 GeV, therefore the scattering/production amplitudes are proportional to the sine of the scattering phase. This scattering phase has been extracted from the scattering data e.g. by García-Martín *et al.* [1] (Madrid group), and it is shown in the mass range relevant for this analysis by the black line in Fig. 48 (labelled "GKPY P-wave"). This behavior can be matched almost exactly by the ρ^0 Breit-Wigner amplitude with $R = 1.45$ GeV^{-1}, shown by the blue line overlapping the black line. The value of this parameter in the range from 1.3 to 1.6 GeV^{-1} gives the phase shift barely distinguishable from the isovector P-wave $\pi^+\pi^-$

phase shift extracted by the Madrid group. A value often utilized in Breit-Wigner fits, $R = 5$ GeV^{-1}, does not work as well, as shown by the green curve.

Since single Breit-Wigner (BW) with $R = 1.45$ GeV^{-1} describes the isovector P-wave $\pi^+\pi^-$ scattering phase well, it should not be necessary to include a tail of $\rho(1450)$ resonance in our analysis.

The phase shift for an alternative parametrization, the Gounaris-Sakurai model (GS) discussed in the Sec. 21 (see Eq. (43)), is also shown for ρ^0 in Fig. 48 by the orange line. It matches the GPKY phase within 2 deg. We note that the BW and GS curves pass through 90 deg near the nominal ρ^0 mass. The phase of the GKPY parameterization is slightly larger at that point (see the lower part of Fig. 48). We explore a possibility of small contributions other than the ρ^0 (and ω) in the fits to our data.

The F-wave $\pi^+\pi^-$ scattering phase extracted from the data by the same group is also shown in the upper part of Fig. 48 (the red line labelled "GKPY F-wave" very close to the horizontal axis). This phase barely reaches 0.25 degrees at $m_{\pi\pi} = 0.8$ GeV, which is extremely small in comparison to 108.7 degrees reached by the P-wave phase. Therefore, contributions from spin 3 resonances can be safely neglected in our analysis.

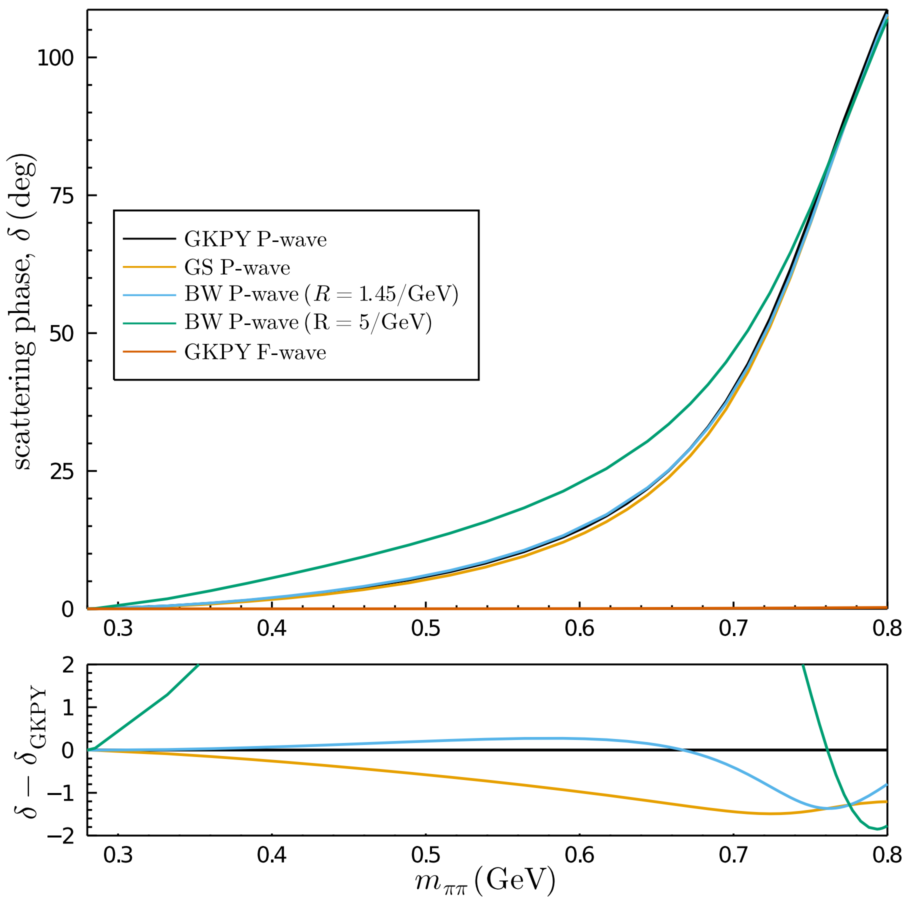

Figure 48: *The isovector $\pi^+\pi^-$ P-wave and F-wave scattering phases extracted from the scattering data by the phenomenological analysis of Ref. [1] (GKPY), compared to the single-pole Breit-Wigner model (BW) with the two different values of R, and Gounaris-Sakurai parameterization [2] from Eq.* (43)*. Note that the blue line is right on top of the black line with a little deviation at the limit of the phase space studied in this analysis. Note also, that the red line in close to zero everywhere. The deviations of the BW and GS models from the GKPY P-wave are shown in the bottom part.*

13 Fits of the coupled-channel model to the $\pi^+\pi^-$ mass distribution

The coupled-channel fit, with $\alpha_{3\pi}$ set to zero ($A = 0$ in Eq. 31) is nearly identical to the fit of ρ^0 Breit-Wigner amplitude described in Sec. 10, as already discussed in Sec. 11 (Eq. 24). They differ only via diagonal coupling of $\omega \to 2\pi$, which is very small $(g_{\omega\to 2\pi}/g_{\rho\to 2\pi})^2 \sim 0.0009$. In fact, such fit displayed in Fig. 49, has a χ^2/NDoF value of 367.8/34, as compared to 366.6/34 obtained with the ρ^0 Breit-Wigner amplitude (Fig. 45).

Allowing for the 3π channel to couple to the 2π channel via ω ($A \neq 0$), as shown in Fig. 50, drastically improves the fit to an almost acceptable level ($\chi^2/\mathrm{NDoF} = 55.1/33$, $pV = 0.0093$), in contrast to the simple-minded Breit-Wigner-sum model discussed previously (Fig. 46, $\chi^2/\mathrm{NDoF} = 102.9/33$, $pV = 4 \times 10^{-9}$). The significance of the ω contribution can be calculated via Wilks theorem [40] from the fit χ^2 difference between the fits without and with $\hat{T}_{2\pi,3\pi}$ term in the amplitude, $n_\sigma = \sqrt{367.8 - 55.1} = 17.7$ standard deviations. We can also estimate the significance of the $\hat{T}_{2\pi,3\pi}$ term as, $A/\Delta A$, where A is the parameter controlling size of this term with respect to the $\hat{T}_{2\pi,2\pi}$ term (see Eq. 31), and ΔA is the fit error. This gives a similar significance to the ω term, 17.7σ.

Since the fit quality is not quite satisfactory, we now allow polynomial corrections to the 2π production coupling (Eq. 25). Already with a linear corrections, $\alpha_{2\pi}(s) = 1 - P_1\, C_1(\hat{s})$ (Eqs. 26-29), an excellent fit quality, $\chi^2/\mathrm{NDoF} = 24.7/32$ ($pV = 0.82$), is achieved with the ρ^0 and ω contributions (Fig. 52). The obtained P_1 coefficient is comfortably small, $P_1 = 0.226 \pm 0.045$. Because it gives the highest p-value, this is our default fit model. It gives the following fit fraction: $R^{0}_{\omega} = 0.0193 \pm 0.0044$ and $R^{all}_{\omega} = 0.214 \pm 0.023$ ($1 - R^{all}_{\omega} = 0.786 \pm 0.023$ is the ρ^0 fit fraction), which are measures of fractional ω contributions with and without interference between the $\hat{T}_{2\pi,2\pi}$ and $\hat{T}_{2\pi,3\pi}$ terms (see Eqs. 35-36). The default fit gives, $A = (0.208 \pm 0.024) \times ({m_\omega}^2 - {m_\rho}^2)$, where the mass difference multiplier was introduced to make the fit parameter dimensionless (values of all floated and fixed parameters in the default fit are summarized in Table 10 in Appendix B). The significance of ω estimated as $A/\Delta A = 8.6\sigma$, is again similar as the one estimated via Wilks theorem, $\sqrt{\Delta\chi^2} = 8.1\sigma$. The fit with the ρ^0 term alone, has still unacceptably low p-value, 2×10^{-7} (Fig. 51).

Table 8: *Fits to the data with the coupled-channel model.*

$\alpha_{2\pi}(s)$	constant		linear (default)		quadratic	
fit components	ρ^0	ρ^0, ω	ρ^0	ρ^0, ω	ρ^0	ρ^0, ω
χ^2/NDoF	367.8/34	55.1/33	90.5/33	24.7/32	54.9/32	24.6/31
pV	1×10^{-57}	0.0093	2×10^{-7}	0.82	0.0071	0.78
$A/({m_\omega}^2 - {m_\rho}^2)$	—	0.287 ± 0.018	—	0.208 ± 0.024	—	0.197 ± 0.042
$A/\Delta A$	—	16.3σ	—	8.6σ	—	4.7σ
$\sqrt{\Delta\chi^2}$	—	17.7σ	—	8.1σ	—	5.5σ
P_1	—	—	0.497 ± 0.042	0.226 ± 0.045	0.163 ± 0.047	0.210 ± 0.066
P_2	—	—	—	—	0.166 ± 0.022	0.016 ± 0.047
R_ω^{all}	—	0.292 ± 0.015	—	0.214 ± 0.023	—	0.206 ± 0.035
R_ω^{0}	—	0.0397 ± 0.0041	—	0.0193 ± 0.0044	—	0.0178 ± 0.0062
$R_{\omega/\rho}^{0}$	—	0.0561 ± 0.0070	—	0.0246 ± 0.0062	—	0.0225 ± 0.0088

There is no improvement in $\rho^0 + \omega$ fit quality when allowing a quadratic term (see Table 8). The fit shown in Fig. 54 has a p-value which dropped to 0.78, indicating that the model is now over-tuned given statistical precision of the data. The P_2 polynomial correction is consistent with zero, 0.016 ± 0.047. The A, P_1, R_ω^{0} and R_ω^{all} values stay within the statistical errors of the linear fit. The statistical errors are larger because of the introduction of unnecessary nuisance parameter. The significance of ω term drops correspondingly, though stays above 5σ from the Wilks theorem (the more proper way to estimate significance than $A/\Delta A$).

The fit with ρ^0 term alone (Fig. 53), does not quite reach acceptable p-value (0.0071), and has the quadratic polynomial term P_2, which is more significant than the P_1 term. This is not an expected behavior for a converging correction series. Since only the tail of ω contributes to our data, it is not a surprise that higher order polynomial modification of the ρ^0 term can start absorbing the ω contribution. Thus further increase in order of polynomial is not very interesting.

It is interesting to display the fitted amplitude with an extended phase-space limit,

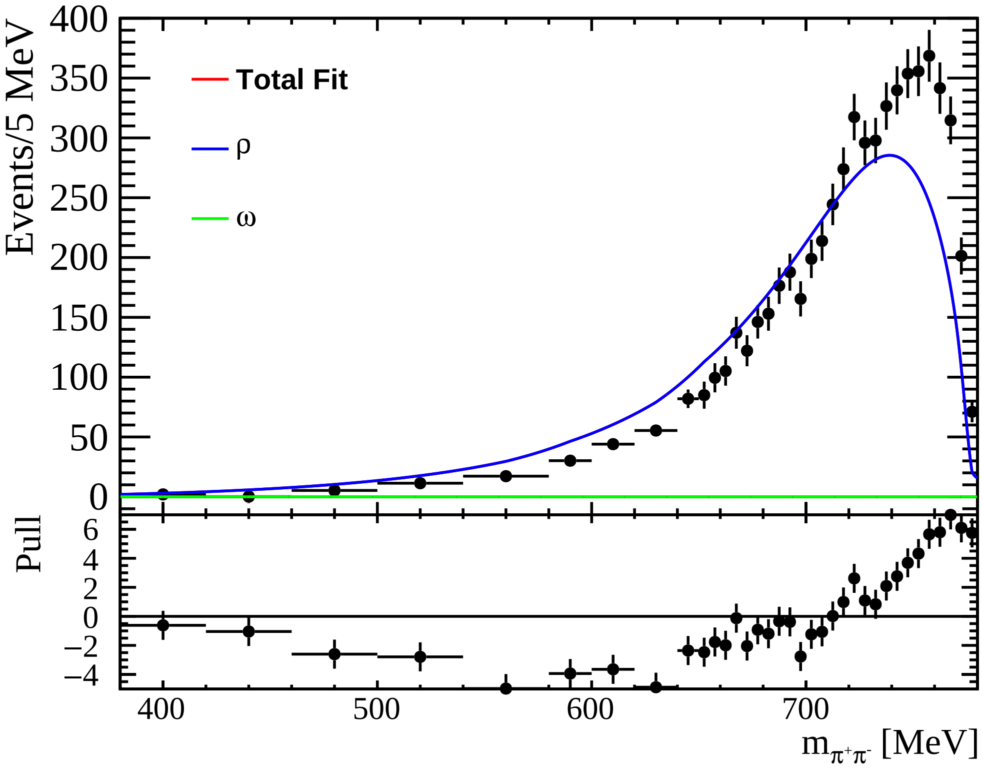

Figure 49: *Fit of the coupled-channel model with ρ^0 alone (i.e. $\alpha_{3\pi} = 0$) and constant $\alpha_{2\pi}(s)$. $\chi^2/\mathrm{NDoF} = 367.8/34$, $pV = 1\times^{-57}$. This fit is almost identical to the fit with ρ^0 Breit-Wigner amplitude (Fig. 45).*

which we achieve by setting $X(3872)$ mass to 4000 MeV. This is shown for the default fit in Fig. 55. The phase-space limit imposed by the actual $X(3872)$ mass (the vertical dashed line) is just below the ω mass peak. Prominent constructive $\rho^0 - \omega$ interference is visible in the mass range available in the $X(3872)$ decays. The ratio of the integrals of the ρ^0 and ω contributions, I_{ρ^0}/I_ω, is 41 ± 10 in actual phase-space, and 5.6 ± 1.6 in the extended phase-space (the errors are statistical from the fit). After dividing I_{omega} by the small $\mathcal{BR}(\omega \to \pi^+\pi^-)$, the ρ^0/ω intensity ratio in the extended phase-space is 0.086 ± 0.023. Since both resonances are nearly fully contained, this ratio reflects the ratio of the $X(3872)$ couplings to $\rho^0 J/\psi$ and $\omega J/\psi$, squared. Taking its square root, we obtain a value of 0.29 ± 0.04, which is very similar to the value of the $X(3872)$ coupling constants extracted by Hanhart *et al.* [34] from the Belle and BaBar data under the $J^{PC} = 1^{++}$ assignment to $X(3872)$, $R_X = 0.26^{+0.08}_{-0.05}$. This value, is an order of magnitude larger than expected for a ratio of isospin violating to isospin conserving decays for an ordinary charmonium state (see Sec. 4 and Ref. [34]).

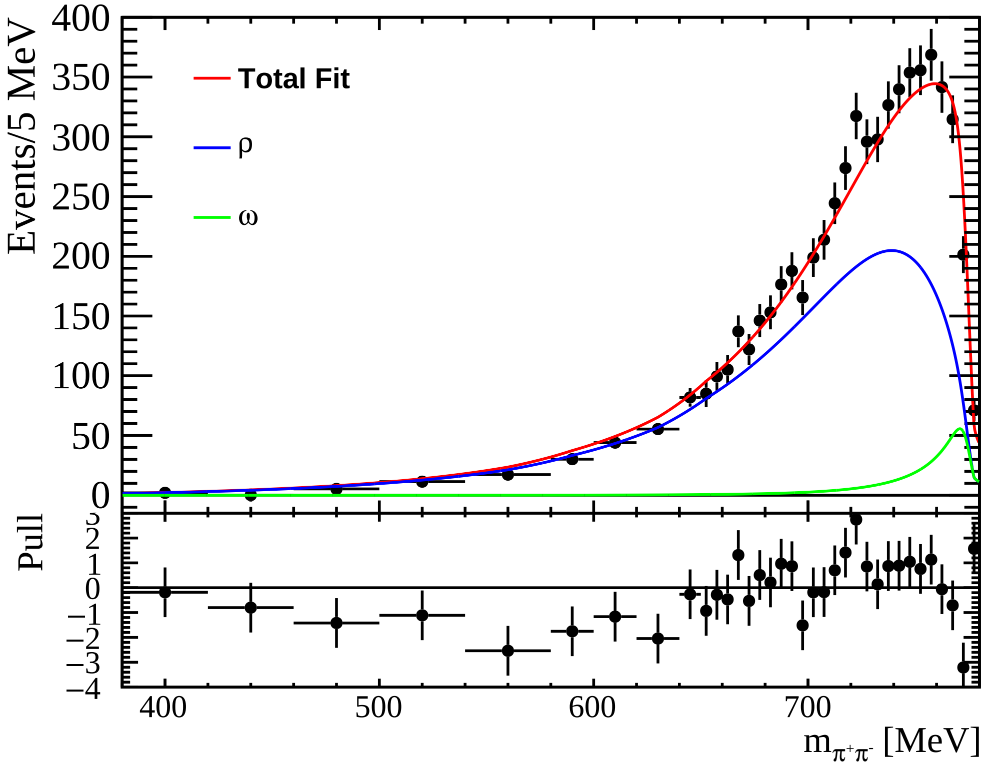

Figure 50: *Fit of the coupled-channel model with the* ρ^0 *and* ω *contributions and constant* $\alpha_{2\pi}$*.* $\chi^2/\mathrm{NDoF} = 55.1/33$, $pV = 0.0093$.

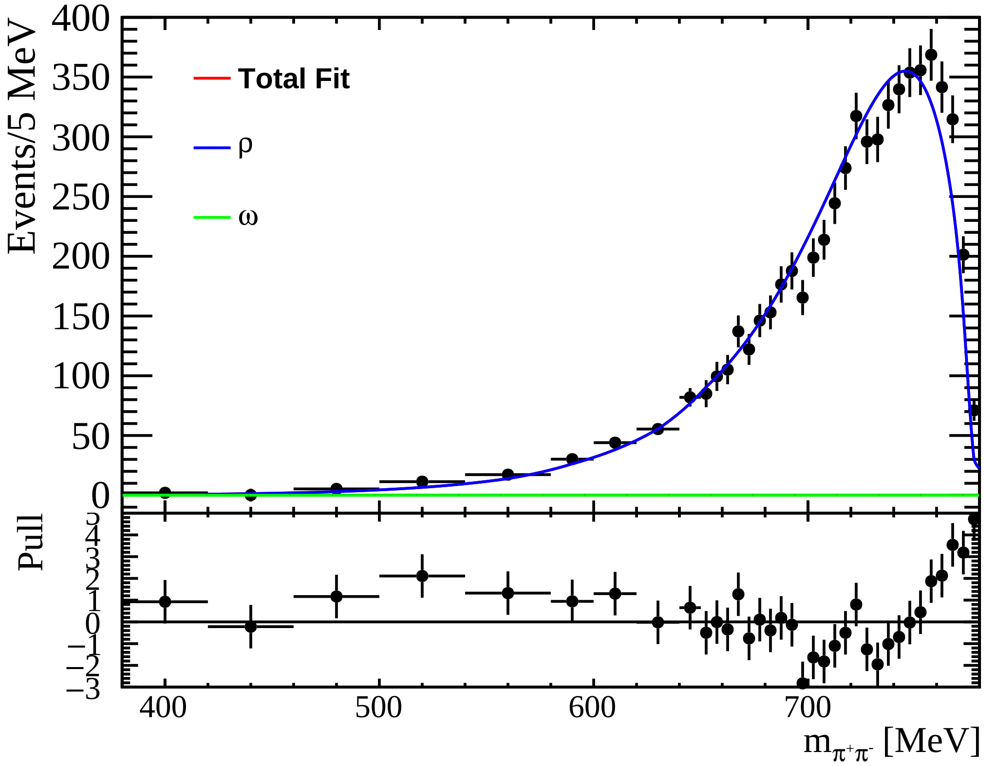

Figure 51: *Fit of the coupled-channel model with ρ^0 alone with linear $\alpha_{2\pi}$.* $\chi^2/\mathrm{NDoF} = 90.5/33$, $pV = 2 \times 10^{-7}$, *and* $P_1 = 0.50 \pm 0.04$.

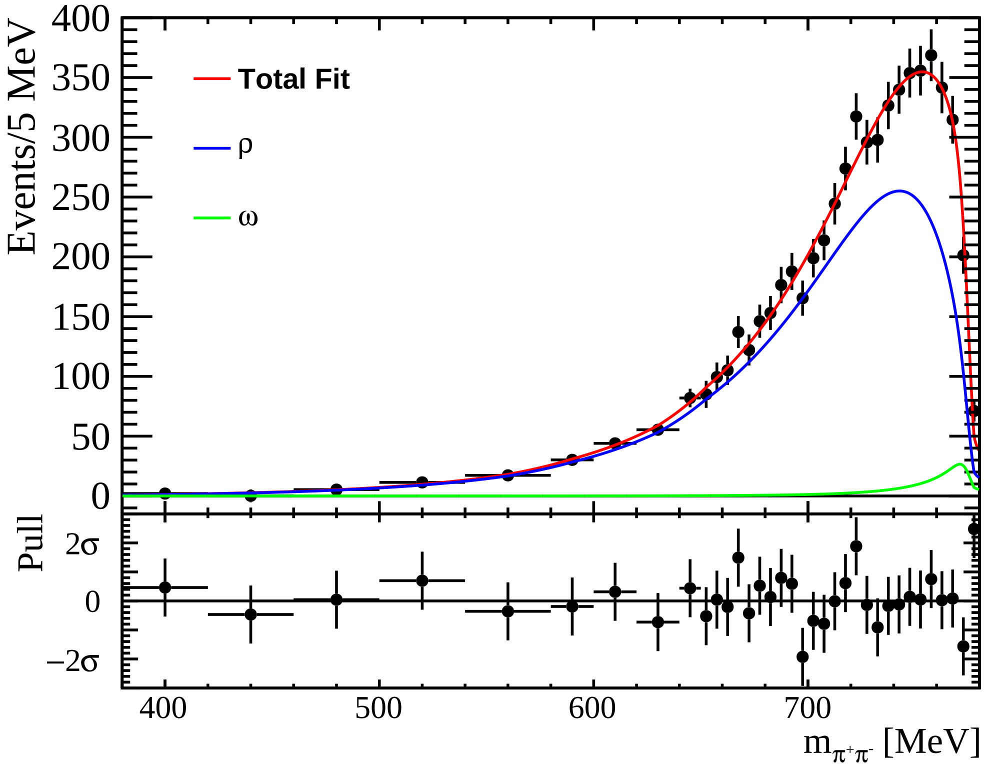

Figure 52: *Fit of the coupled-channel model with the* ρ^0 *and* ω *contributions and linear dependence of* $\alpha_{2\pi}$ *on* $m^2_{\pi\pi}$*. This is our default fit to the data.* $\chi^2/\mathrm{NDoF} = 24.7/32$*,* $pV = 0.82$*, and* $P_1 = 0.226 \pm 0.045$.

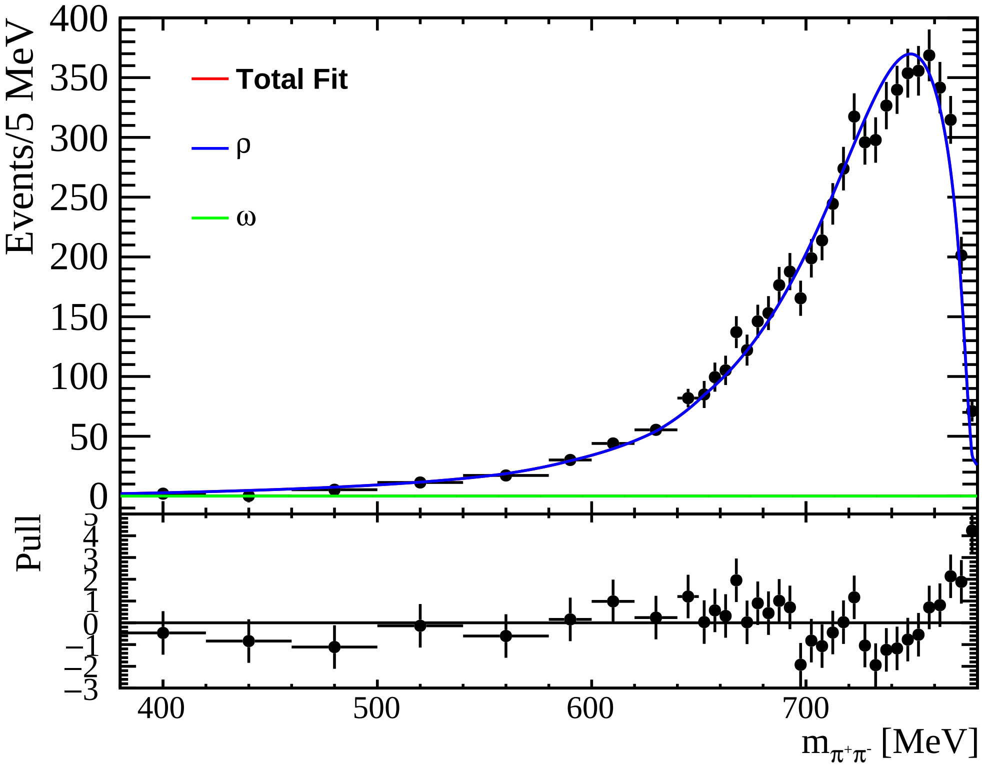

Figure 53: *Fit of the coupled-channel model with ρ^0 alone and quadratic $\alpha_{2\pi}$.* $\chi^2/\mathrm{NDoF} = 54.9/32$, $pV = 0.0071$, $P_1 = 0.16 \pm 0.05$, *and* $P_2 = 0.17 \pm 0.02$.

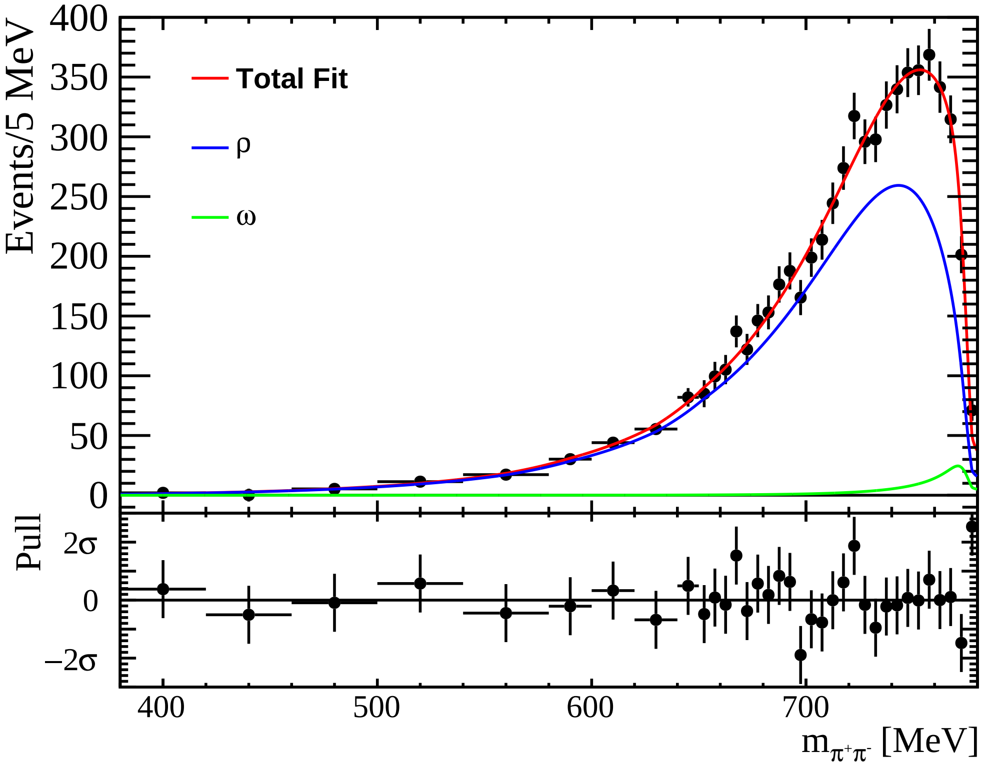

Figure 54: *Fit of the coupled-channel model with* ρ^0 *and* ω *and quadratic* $\alpha_{2\pi}$*.* $\chi^2/\mathrm{NDoF} = 24.6/31$*,* $pV = 0.78$*,* $P_1 = 0.21 \pm 0.07$*, and* $P_2 = 0.02 \pm 0.05$*.*

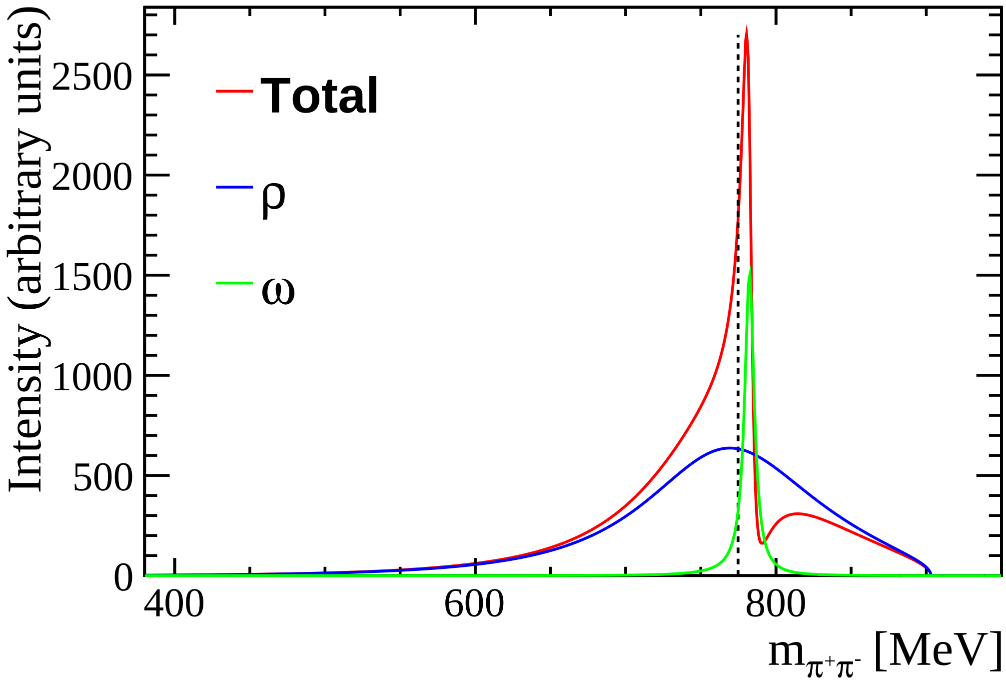

Figure 55: *The amplitude model obtained by the fit to the LHCb data, with the phase-space limit extended by setting $X(3872)$ mass to 4000 MeV. The actual phase-space limit imposed by the true $X(3872)$ mass is indicated by the vertical dashed line. No mass resolution, nor detector efficiency were included here.*

14 Fit model variations

The ρ^0 mass and width values which we use in the nominal fit are the world average numbers over the determinations in e^+e^- experiments [22]. Since we use the same values when tuning the Blatt-Weisskopf form-factor parameter R to the isovector P-wave e^+e^- phase variation extracted from the scattering experiments, there is no strong motivation to vary these parameters. Nevertheless, as a cross-check we try to fit them to our data, one at a time (see Figs. 56-57). The fit quality changes insignificantly, as shown in Table 9, which summarizes all cross-checks and systematic studies. The fitted values, $m_\rho = 771.1 \pm 10.8$ MeV and $\Gamma_\rho = 144.2 \pm 12.4$ MeV, are consistent with the world average values. The ω fractional contributions, R_ω^{all} and R_ω^{0}, remain consistent with the nominal results, however, they now have large statistical errors[12] reflecting that the ρ^0 mass and width are not well constrained by our data, as only about half of this resonance is within the available phase-space. Without external input on ρ^0 parameters the discrimination between ρ^0 and ω is difficult, as also reflected in low ω significance levels.

Since ω resonance peaks beyond the phase-space limit, our data are unable to probe for its mass and width. Since this is such a narrow resonance, its parameters are very well determined and don't vary across different production mechanisms.

The scattering data constrain the R parameter, to about $1.3 - 1.6$ GeV^{-1} range. We use $R = 1.45$ GeV^{-1} in the nominal fit. The variation of R in the interval given above, hardly yields any change in the results (Tab. 9, Fig. 58). The Gounaris-Sakurai model of ρ^0, discussed in Sec. 21, offers an alternative approach to the Breit-Wigner amplitude with the R-dependent form-factor, and constitutes a more drastic systematic variation for related shape uncertainty.

In principle, the 2π production form-factor in $X(3872)$ decays (entering via $B_1(p)$ in Eq. 20) could be different than the one determined from the $\pi\pi$ scattering experiments. In the default fit, we use $R_{prod} = R = 1.45$ GeV^{-1}. If we consider R_{prod} to be an independent parameter of the $R = 1.45$ GeV^{-1} in the denominator of Eq. 12, we find that the data are insensitive to its value. We vary it in a wide range, 0-30 GeV^{-1}, as shown in Table 9 and Fig. 59.

[12] They are not consistent when the ω term is excluded from the fit, $m_\rho = 831 \pm 16$ MeV and $\Gamma_\rho = 102 \pm 6$ MeV.

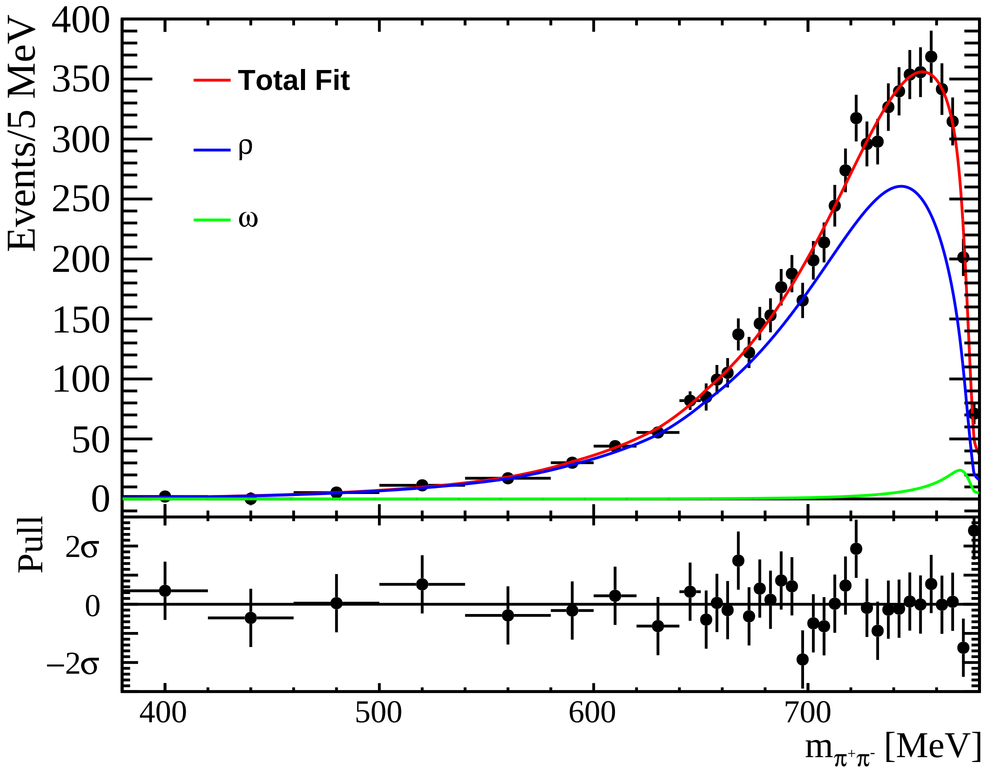

Figure 56: *Fits of the coupled-channel model with ρ^0 and ω contributions and linear dependence of $\alpha_{2\pi}$ on $m^2_{\pi\pi}$. In this fit, m_ρ mass is a free parameter.* $\chi^2/\mathrm{NDoF} = 24.7/31$*, pV* $= 0.78$*,* $m_\rho = 777.1 \pm 10.8$ *MeV and* $P_1 = 0.23 \pm 0.06$*.*

As a variation of the production model, we add a non-resonant terms to the production vector, via

$$\begin{pmatrix} \hat{A}_{2\pi} \\ \hat{A}_{3\pi} \end{pmatrix} = [1 - i\,K\,\rho]^{-1} \left[K \begin{pmatrix} \alpha_{2\pi} \\ \alpha_{3\pi} \end{pmatrix} + \begin{pmatrix} f_{2\pi} \\ f_{3\pi} \end{pmatrix} \right]. \tag{38}$$

Without $X(3872) \to 3\pi J/\psi$ data in the fit, we are unable to probe for $f_{3\pi}$, thus we set it to zero. A constant $\alpha_{2\pi}$ suffices for a good fit in such approach, with the same fit quality as the default model with the linearly corrected $\alpha_{2\pi}(s)$ and no non-resonant production (Fig. 60). The NR production parameter is significant, $f_{2\pi} = (-9.7 \pm 1.6) \times 10^{-7}$. The ω results are similar to the nominal fit (see Tab. 9). Adding non-resonant terms to the K-matrix[13] is known to affect the effective K-matrix pole positions. Without ability to control ρ^0 and ω pole masses from our data, such exercise would not have had a well defined meaning.

After the R parameter has been tuned to the scattering data, there is no strong

[13]This can be accomplished by adding a diagonal constant matrix to Eq. 11.

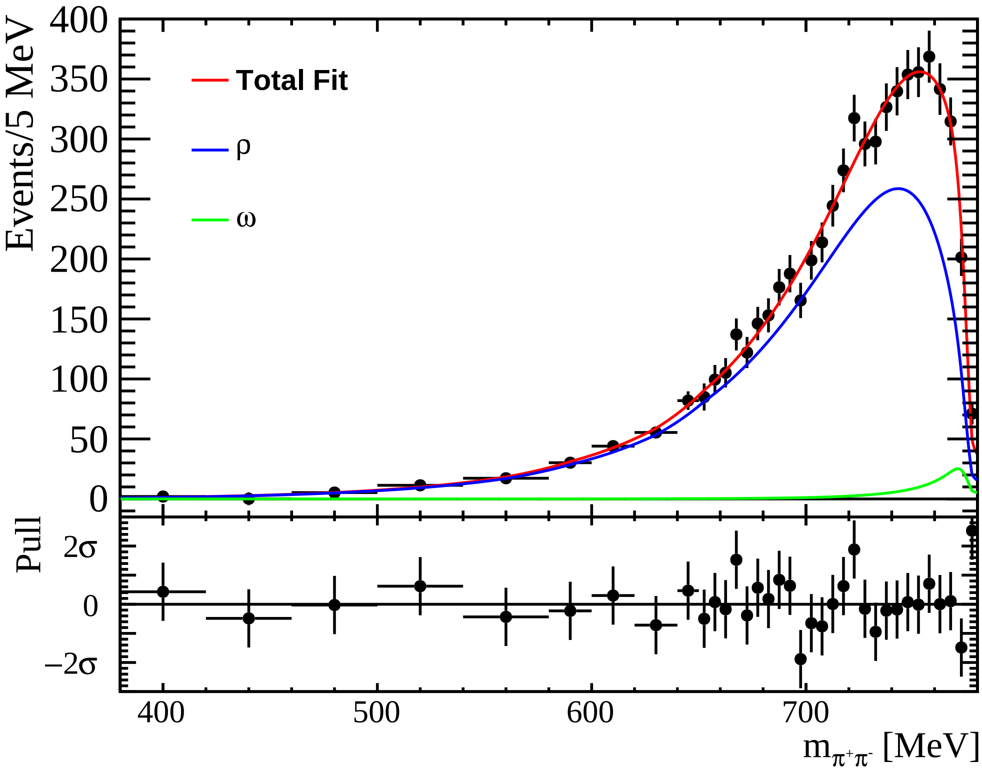

Figure 57: *Fits of the coupled-channel model with ρ^0 and ω contributions and linear dependence of $\alpha_{2\pi}$ on $m^2_{\pi\pi}$. In this fit, Γ_ρ mass is a free parameter.* $\chi^2/\mathrm{NDoF} = 24.7/31$*,* $pV = 0.78$*,* $\Gamma_\rho = 144.2 \pm 12.4$ *MeV and* $P_1 = 0.21 \pm 0.08$*.*

motivation to include an excited ρ^0 to the K-matrix. Nevertheless, we try

$$K = K_0 + \frac{1}{m_{\rho'}{}^2 - s} \begin{pmatrix} g_{\rho'\to 2\pi}{}^2 & 0 \\ 0 & 0 \end{pmatrix}, \tag{39}$$

where $g_{\rho'\to 2\pi} = m_{\rho'}\Gamma_{\rho'}\mathcal{B}(\rho' \to 2\pi)/\rho_{2\pi}(m_{\rho'})$. We set $m_{\rho'} = 1465$ MeV, $\Gamma_{\rho'} = 400$ MeV [22]. Assuming that 2π and 4π channels dominate ρ' width, and given $\mathcal{B}(\rho' \to 2\pi)/\mathcal{B}(\rho' \to 4\pi) = 0.37 \pm 0.10$ [22], we derive $\mathcal{B}(\rho' \to 2\pi) = (27 \pm 6)\%$. It is necessary to allow for linear term in $\alpha_{2\pi}(s)$, which becomes larger $P_1 = 0.32 \pm 0.05$. The fit quality becomes insignificantly worse ($pV = 0.80$), and the ω results don't change much (Tab. 9, Fig. 61).

Changing the well motivated form of $\rho_{3\pi}(s)$ given by Eq. 17 to the simple approximation given by Eq. 16, changes the ω results very little (Tab. 9), since the ω width is rather small.

Even though, it would be hard to argue that approximations should be taken on par with more accurate formulae, it is interesting to check what happens to the fit results when $g^2_{\omega\to 2\pi}$ term in the K-matrix is dropped, resulting in Eqs. 24 and 30. As can be seen from

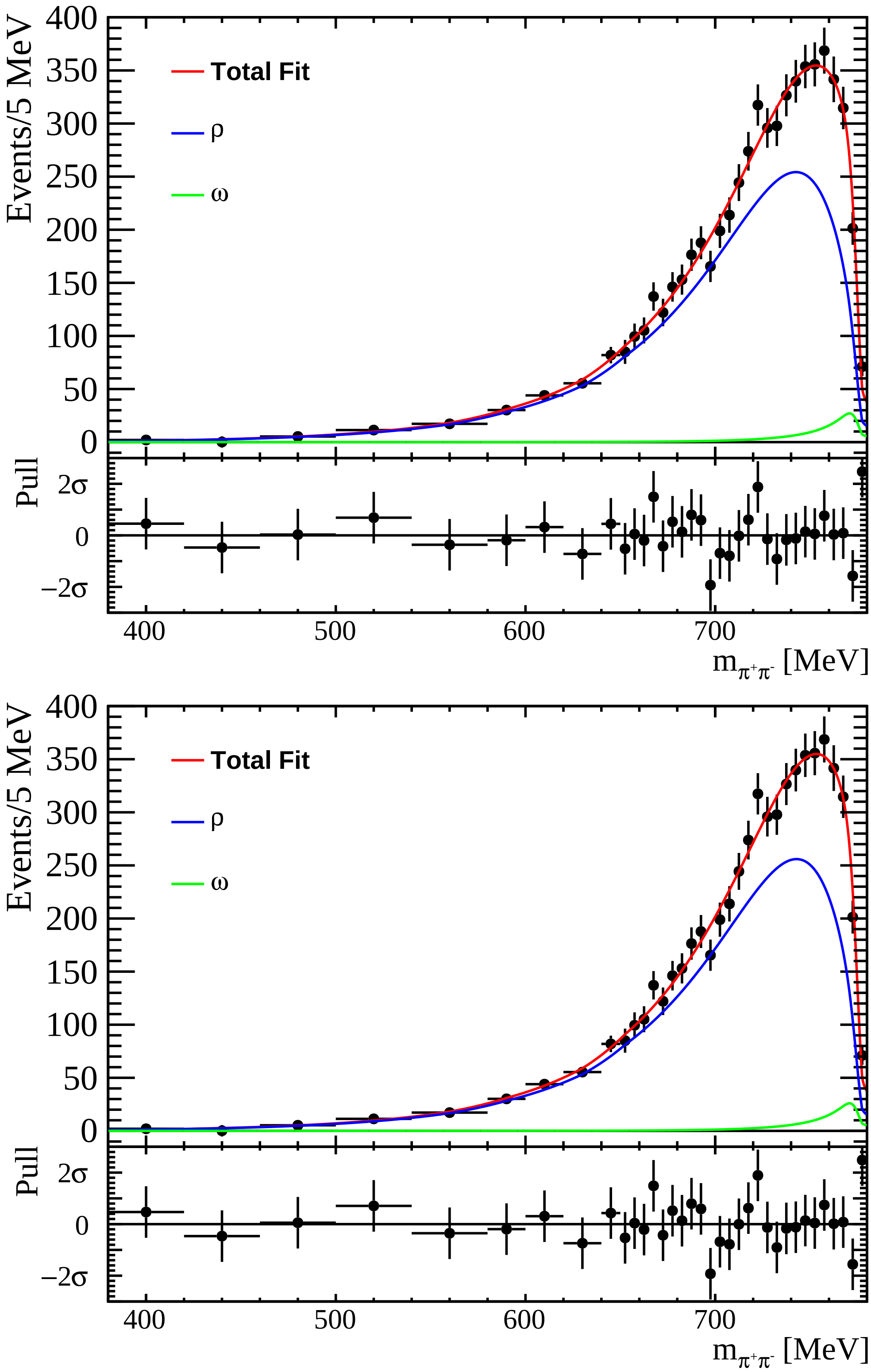

Figure 58: *Fits of the coupled-channel model with* ρ^0 *and* ω *contributions and linear dependence of* $\alpha_{2\pi}$ *on* $m_{\pi\pi}^2$. *In these fits,* $R = 1.3$ *(1.6) GeV*$^{-1}$ *at the top (bottom) displays. The* P_1 *coefficients are* 0.21 ± 0.05 (0.24 ± 0.05)*, respectively.*

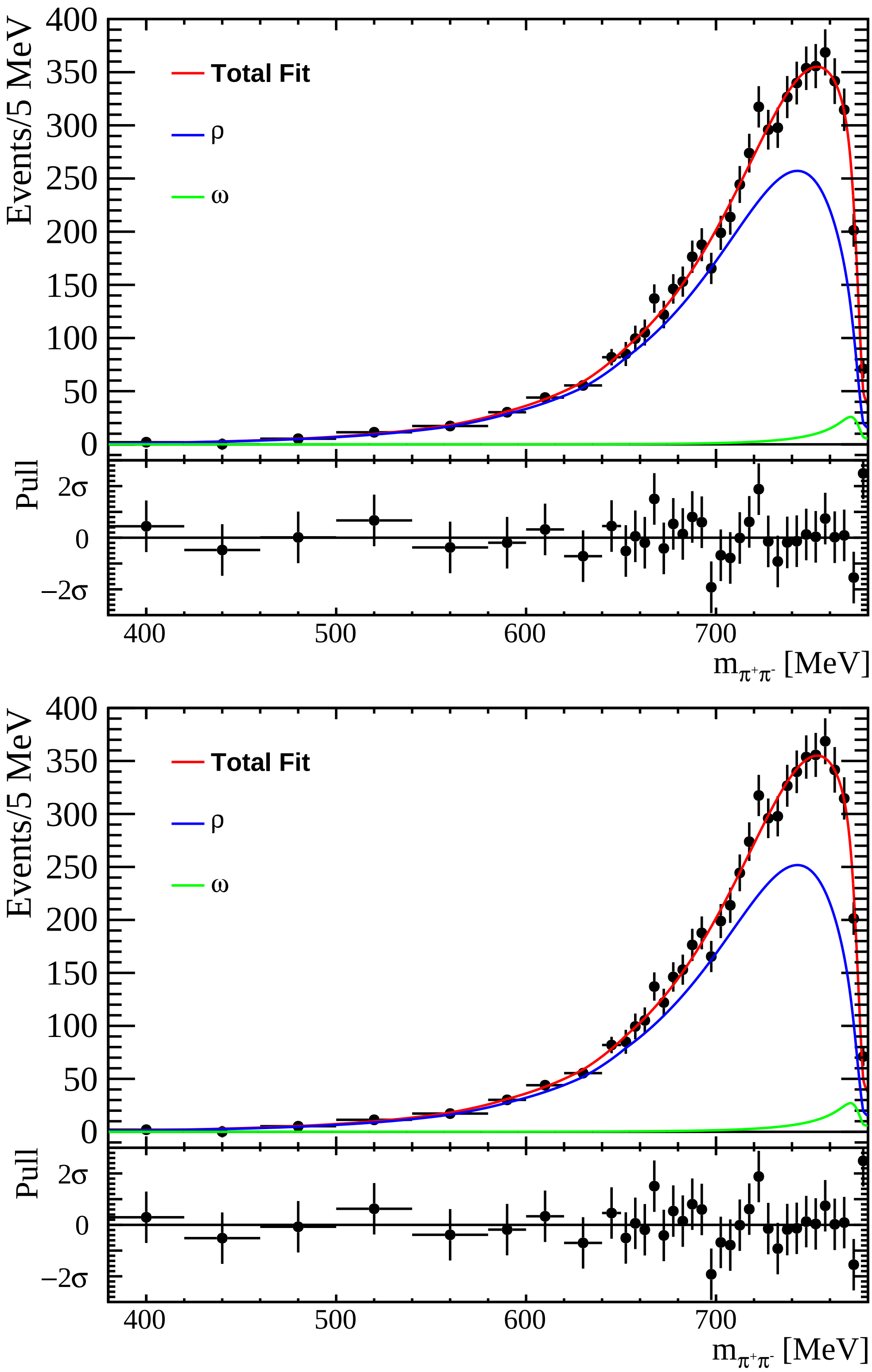

Figure 59: *Fit of the coupled-channel model with the ρ^0 and ω contributions and linear dependence of $\alpha_{2\pi}$ on $m^2_{\pi\pi}$. The top (bottom) figures are obtained with $R_{prod} = 0$ (30) GeV^{-1} (see the text). The P_1 coefficients are 0.17 ± 0.04 (0.56 ± 0.05), respectively.*

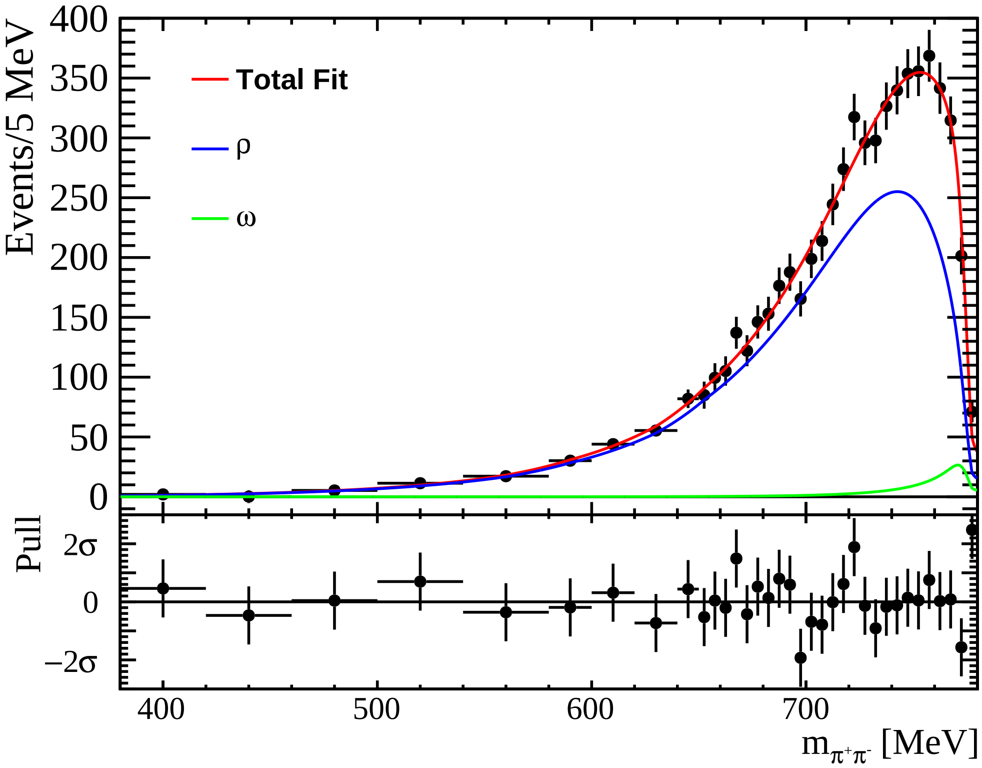

Figure 60: *Fit of the coupled-channel model with ρ^0 and ω contributions and constant dependence of $\alpha_{2\pi}$ on $m^2_{\pi\pi}$. Non-resonant $\pi^+\pi^-$ terms is added to the production vector.* $\chi^2/\mathrm{NDoF} = 24.5/32$ *and* $pV = 0.82$.

Tab. 9, the fit results hardly change, which gives validity to the interpretation of $\hat{T}_{2\pi,2\pi}$ term as ρ^0 component, and $\hat{T}_{2\pi,3\pi}$ term as ω component, which is implied throughout this work.

15 D-wave decay of $X(3872)$

In the default fit, we neglect D-wave decays by assuming that $X(3872)$ decays to J/ψ and $\pi^+\pi^-$ in S-wave. This is well justified since the analysis of the angular correlations in this decay set a tight limit on a fraction of D-wave decays, $f_D < 4\%$ at 95% confidence level [3]. The likelihood function peaked at 10 times smaller value, $f_D \sim 0.004$, as shown in Fig. 63.

In this section, we perform fits to the dipion mass distribution in which we allow for

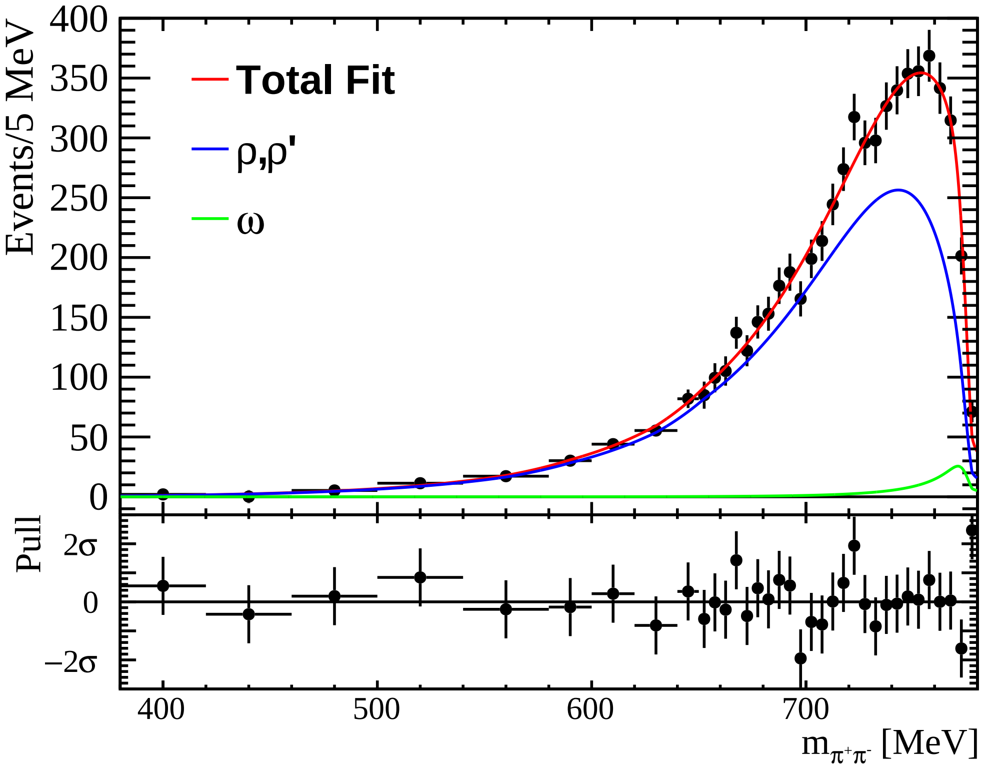

Figure 61: *Fit of the coupled-channel model with* ρ^0 *and* ω *contributions and linear dependence of* $\alpha_{2\pi}$ *on* $m^2_{\pi\pi}$. *An excited* ρ^0 *is included in the K-matrix.* $\chi^2/\mathrm{NDoF} = 25.1/32$, $pV = 0.80$ *and* $P_1 = 0.32 \pm 0.05$.

D-wave amplitude (A_D). We multiply the PDF function (Eq. 4) by a factor, S_D, given by:

$$S_D = 1 + \left[A_D\, F_2(p_{J/\psi}, p_{J/\psi}(m_\rho))\right]^2, \tag{40}$$

$$F_2(p_{J/\psi}, p_{J/\psi}(m_\rho)) = \sqrt{\frac{B_2(p_{J/\psi})}{B_2(p_{J/\psi}(m_\rho))}}, \tag{41}$$

$$B_2(p_{J/\psi}) = {p_{J/\psi}}^4 \frac{1}{9 + 3\,(R\,p_{J/\psi})^2 + (R\,p_{J/\psi})^4}, \tag{42}$$

where $B_2(p)$ is the Blatt-Weisskopf barrier factor for D-wave decay (we used the notation of Eqs. 7-8). With this normalization choice, ${A_D}^2$ expresses the ratio of D-wave to S-wave probabilities at the ρ^0 mass ($F_2 = 1$ at $m_{\pi\pi} = m_\rho$).

The χ^2 value changes from 24.7 with $A_D = 0$ to 24.5 when A_D is floated in the fit. Thus, D-wave contribution from the fit to the dipion mass distribution is completely insignificant (0.5σ from Wilks theorem). In fact, the fit p-value drops from 0.82 to 0.79. The fitted value, $A_D = 0.13 \pm 0.41$, is consistent with zero within the large error ($A_D/\Delta A_D = 0.3\sigma$), and corresponds to a D-wave to S-wave fraction at $m_{\pi\pi} = m_\rho$ of

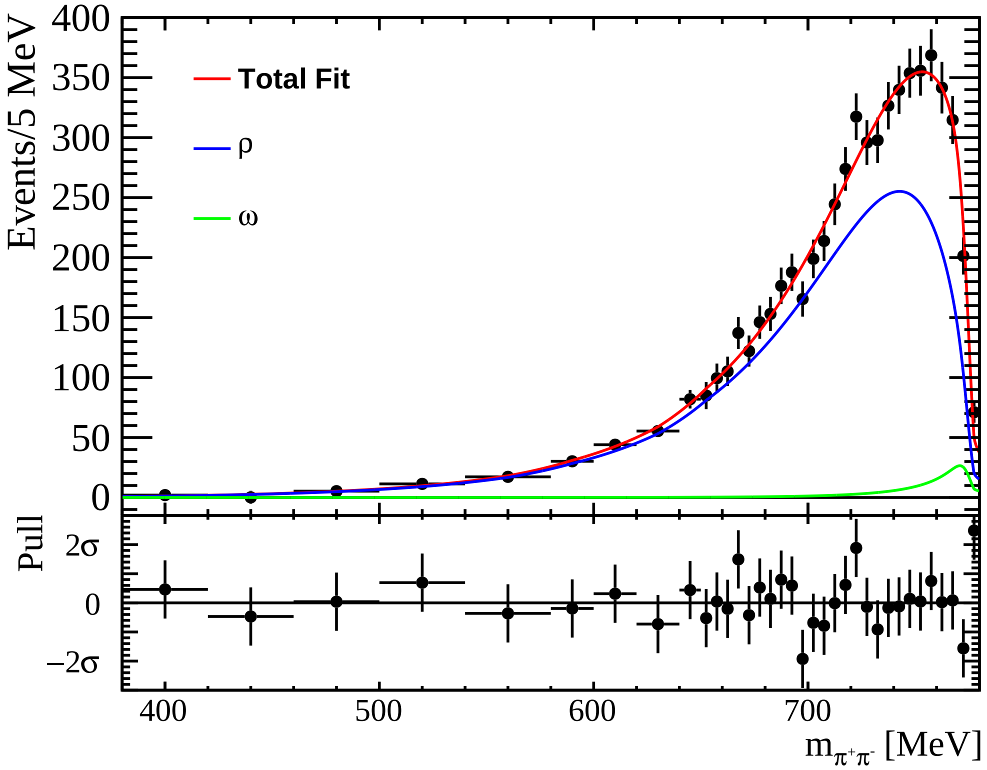

Figure 62: *Fits of the coupled-channel model with ρ^0 and ω contributions and linear dependence of $\alpha_{2\pi}$ on $m^2_{\pi\pi}$. Fit result when $g^2_{\omega\to 2\pi}$. $\chi^2/\mathrm{NDoF} = 24.7/32$, $pV = 0.82$ and $P_1 = 0.23 \pm 0.05$.*

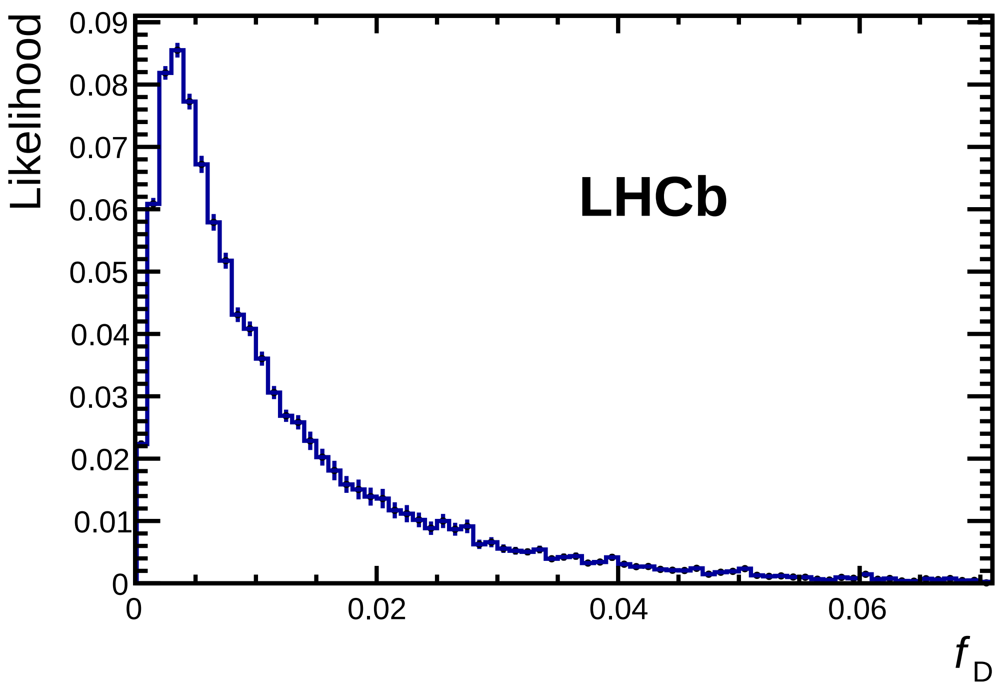

Figure 63: *Likelihood-weighted distribution of the D–wave fraction as extracted from the analysis of angular correlations in $X(3872)$ decays to J/ψ and $\pi^+\pi^-$ (Fig. 2 from Ref. [3]).*

$(1.7^{+27.2}_{-\ 1.7})\%$. When integrating the probabilities in the full phase-space without efficiency and mass resolution, the corresponding D-wave fit fraction is $f_D = (2.2^{+26.6}_{-\ 2.2})\%$. The significance of the ω contribution is still very high (7.8σ from Wilks theorem). The measures of ω fit fraction change only by about a quarter of the statistical errors in the default fit (see Table 9). The statistical errors on the ω fit fraction increase somewhat, however, they reflect the uncertainty in f_D from the dipion mass fit alone. From the analysis of the angular correlations discussed above, the uncertainty in f_D is an order of magnitude smaller. By using iterative procedure, we have found that $A_D = 0.176$ corresponds to $f_D = 4\%$. Fixing A_D at this value restores the statistical errors on R^{all}_{ω} and R^{0}_{ω} to the values from the default fit (Table 9). We use this fit, shown in Fig. 64, to bound the systematic uncertainty due to possible non-zero D-wave fraction.

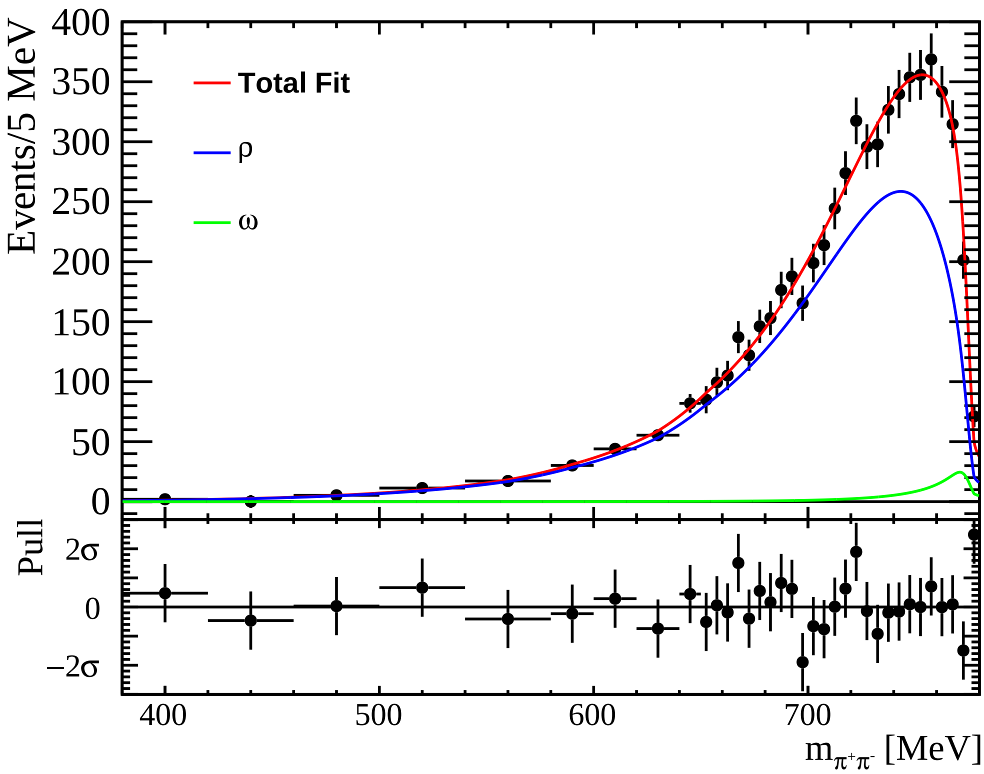

Figure 64: *Fit of the coupled-channel model with the* ρ^0 *and* ω *contributions, linear dependence of* $\alpha_{2\pi}$ *on* $m^2_{\pi\pi}$ *and* $A_D = 0.176$*, which gives the D-wave fraction of 4%.* $\chi^2/\mathrm{NDoF} = 24.5/32$, $pV = 0.82$*, and* $P_1 = 0.313 \pm 0.046$.

16 Check for interference with other decays

The final state we have selected, $B^+ \to J/\psi K^+\pi^+\pi^-$, is dominated by production of kaon excitations. This a dominant component of the smooth background under the $X(3872)$ peak in the $J/\psi\pi^+\pi^-$ distribution (Fig. 30), as fraction of non-B^+ candidates is rather small (Fig. 31). The $X(3872)$ has a very narrow natural width [41], thus it is rather unlikely for it to interfere with such contributions. Such interferences are neglected in our analysis. As the composition of kaon resonances changes with $K^+\pi^+\pi^-$ mass, correlated with the $X(3872)$ helicity angle, $\cos\theta_X$ (defined as an angle in the $X(3872)$ rest frame between the J/ψ and K^+ directions), we can check for possible interference effects with the kaon excitations by dividing the total sample into subsamples of $\cos\theta_X < 0$ and $\cos\theta_X > 0$ data. The $X(3872)$ is expected to be split approximately evenly by such subdivision. We have performed independent extraction of the dipion mass distribution in each subsample, by the method described in Sec. 6. While the mass resolution is consistent in the two subsamples, the relative efficiency differ somewhat, as shown in Fig. 65. We then fitted each subsample separately, as illustrated in Fig. 66. The results are compatible with each other, proving that any potential interference effects are not significant and can be neglected.

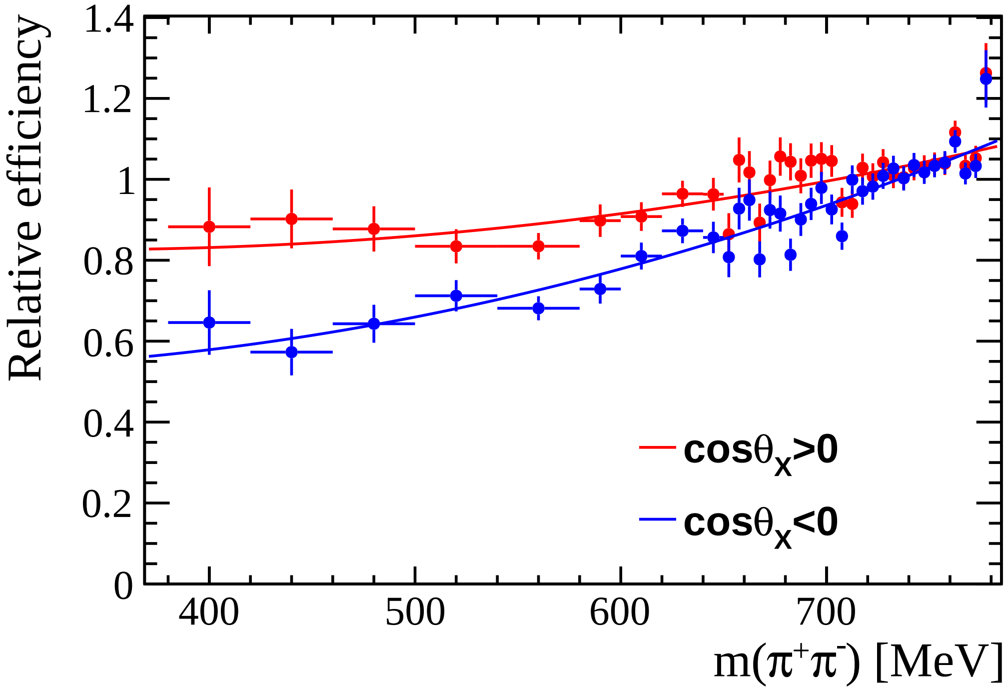

Figure 65: *Dipion mass efficiency for* $cos\theta_X > 0$ *and* $cos\theta_X < 0$ *samples.*

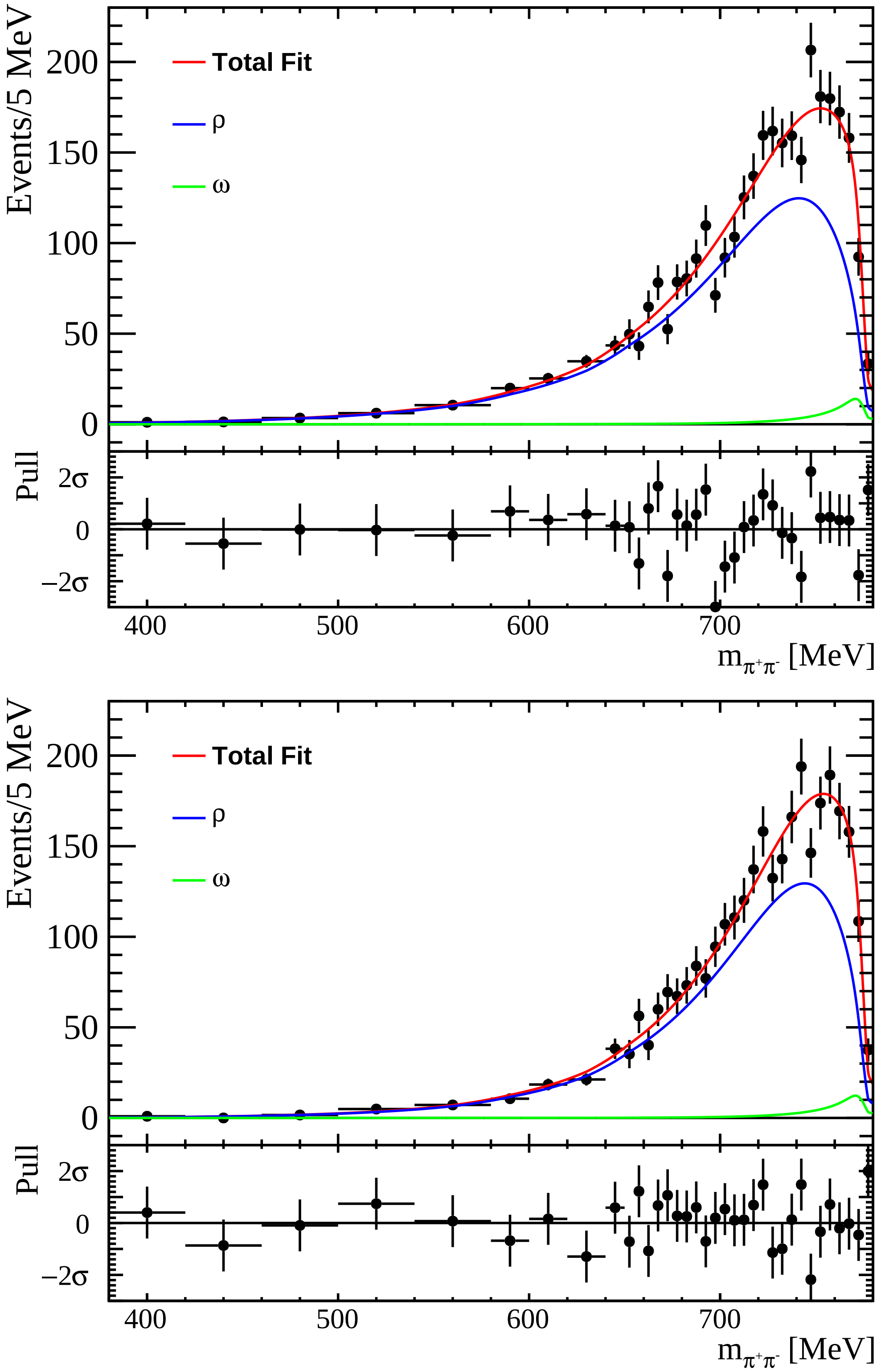

Figure 66: *Fit of thee coupled-channel model with the* ρ^0 *and* ω *contributions and linear dependence of* $\alpha_{2\pi}$ *of* $m^2_{\pi\pi}$. *The top: fit sample is in the* $cos\theta_X > 0$ *region,* $\chi^2/\mathrm{NDoF} = 42.2/32$, $pV = 0.11$. *The bottom: fit sample is in the* $cos\theta_X < 0$ *region,* $\chi^2/\mathrm{NDoF} = 26.9/32$ *and* $pV = 0.72$. θ_X *is the helicity angle of* $X(3872)$. *The* P_1 *coefficients are* 0.16 ± 0.05 *and* 0.31 ± 0.08, *respectively.*

17 Selection of data with multivariate discriminant

Our default data selection uses relatively loose cuts, since non-B^+ background are relatively small in the signal region (see Fig. 31), thanks to the narrowness of the B^+ and $X(3872)$ mass peaks. To check for possible systematic effects in the simulations of efficiency variation with $m_{\pi\pi}$ influencing our results, we perform a more sophisticated data selection, which makes a more aggressive use of hadron identification, and folds in information from other discriminating variables by the use of Boosted Decision Tree method. We perform this tighter data selection on top of our nominal data selection cuts.

The following variables have been used on input to BDT:

- A combined hadron ID variable: log[K_ProbNNk(1-K_ProbNNpi) Pi1_ProbNNpi(1-Pi1_ProbNNk) Pi2_ProbNNpi(1-Pi2_ProbNNk)] (labeled kNN in Fig. 69),
- A log of B^+ vertex χ^2/NDoF (labeled as Bvc2),
- A log of the minimum of hadron $\chi^2_{\rm IP}$ (labeled as hIPc2min)
- A log of the minimum of hadron PT (labeled as hptmin)
- A log of B^+ $\chi^2_{\rm IP}$ (labeled as B_IPc2)
- A log of the minimum between $\mu^+\mu^-$ $\chi^2_{\rm IP}$ (labeled as Min_Mu1_IPchi2_Mu2_IPchi2)
- B^+ A log of B flight distance χ^2 (labeled B_FDchi2)
- A log of 1-B_DIRA (labeled as B_DIRA)

We utilize a large, clean sample of $B^+ \to \psi(2S)K^+$, $\psi(2S) \to \pi^+\pi^- J/\psi$ events in our preselected data sample (see Fig. 67) as a signal proxy, since it has a topology very similar to $B^+ \to X(8372)K^+$, $X(3872) \to \pi^+\pi^- J/\psi$. After 2σ cuts around the B^+ and $\psi(2S)$ masses, $120k$ events are used in training. Non-B background in the training sample is only 1%, as determined bu the fit to the B^+ mass distribution (see Fig. 68), and it is simply ignored. The non-B background sample for training is taken from $4-10\sigma$ sidebands of the B^+ mass peak, which are also outside 4σ mass windows around the $\psi(2S)$ and $X(3872)$ signal peaks and have $\pi^+\pi^- J/\psi$ mass below 3950 MeV. The distributions of the BDT input variables for the signal and background training samples is shown in Fig. 69.

The cut on BDT output discriminant is -0.1091, as determined from the optimization curve shown in Fig. 70. The distribution of the BDT output discriminant on the actual $X(3872)$ signal sample is shown in Fig. 73. About 8% of the events are removed by the cut. The total signal $X(3872)$ yield is 6761 ± 100 (see Fig. 71), which is 99.6% of our nominal yield, and close to the expectations from the simulations, 99.4% (Fig. 74). The non-B^+ background has been reduced from 9.4% in our default sample to 3.1% (see Fig. 72). However, the gain in the background level under the $X(3872)$ peak, 17% vs. 23%, is very modest because of the irreducible background from the other $B^+ \to J/\psi K^+\pi^+\pi^-$ decays (kaon excitations).

The efficiency variation with $m_{\pi\pi}$ (Fig. 75) is similar to the one in the nominal analysis (Fig. 43). The mass resolution does not change.

The fit results to the dipion mass distribution (Fig. 76 and Table 9) are very consistent with the nominal result.

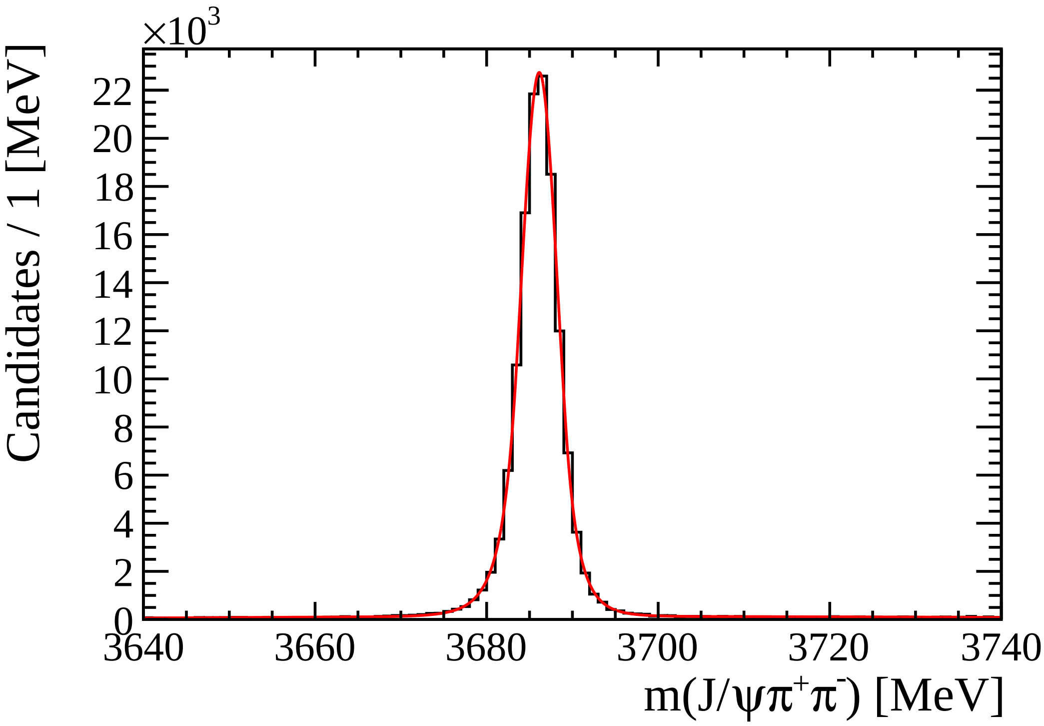

Figure 67: *A fit to the $\psi(2S)$ peak in the $J/\psi\pi^+\pi^-$ mass distribution after the $\pm 2\sigma$ cut on the B^+ mass.*

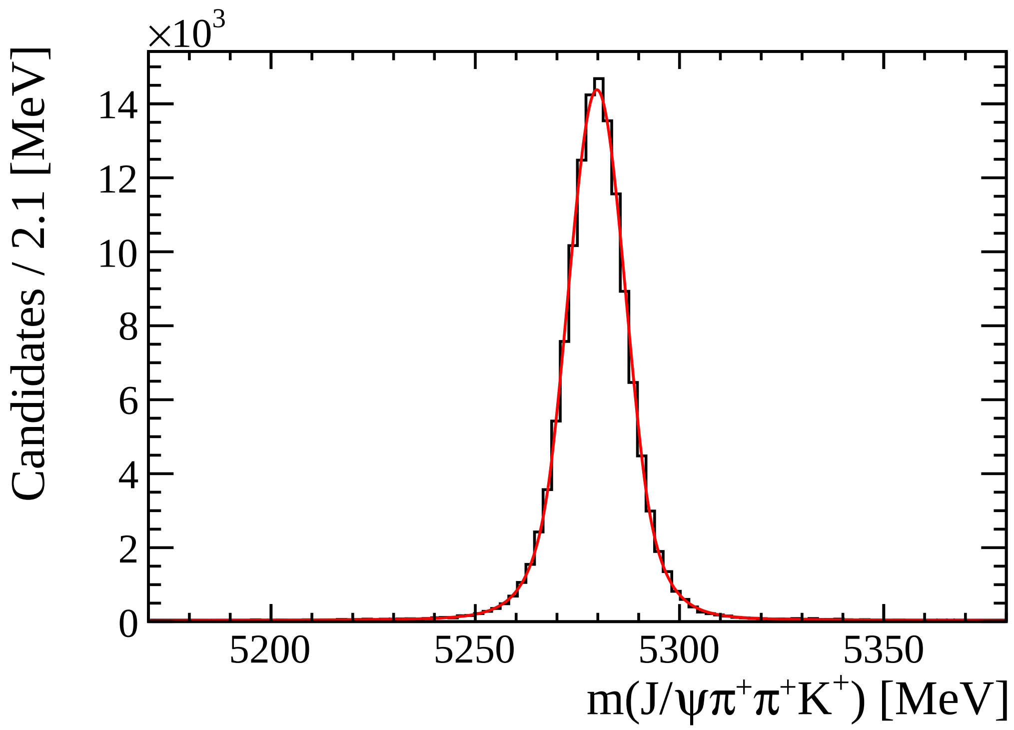

Figure 68: *A fit to the B^+ mass peak after the $\pm 2\sigma$ cut on the $\psi(2S)$ mass.*

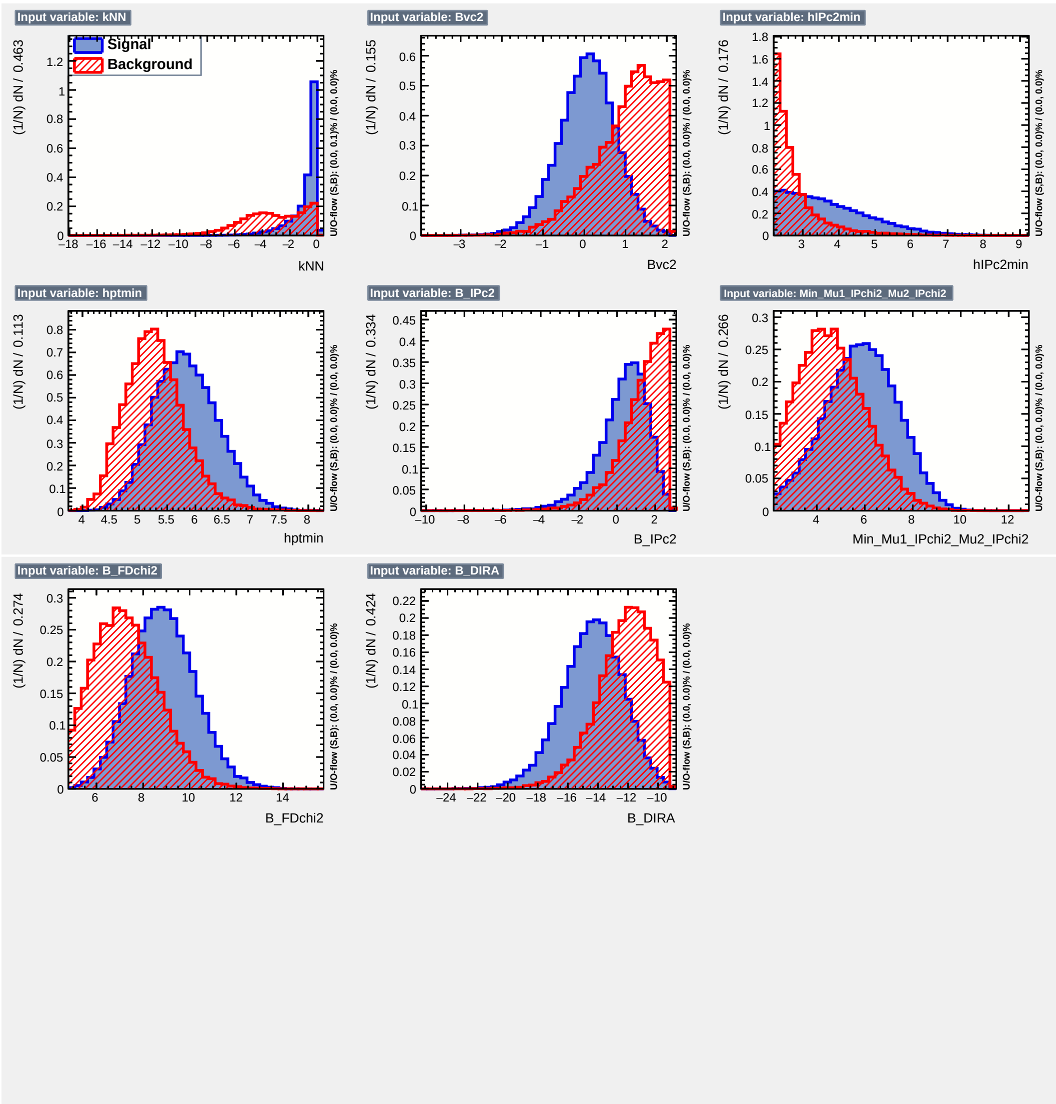

Figure 69: *BDT input variables (see the description in the text).*

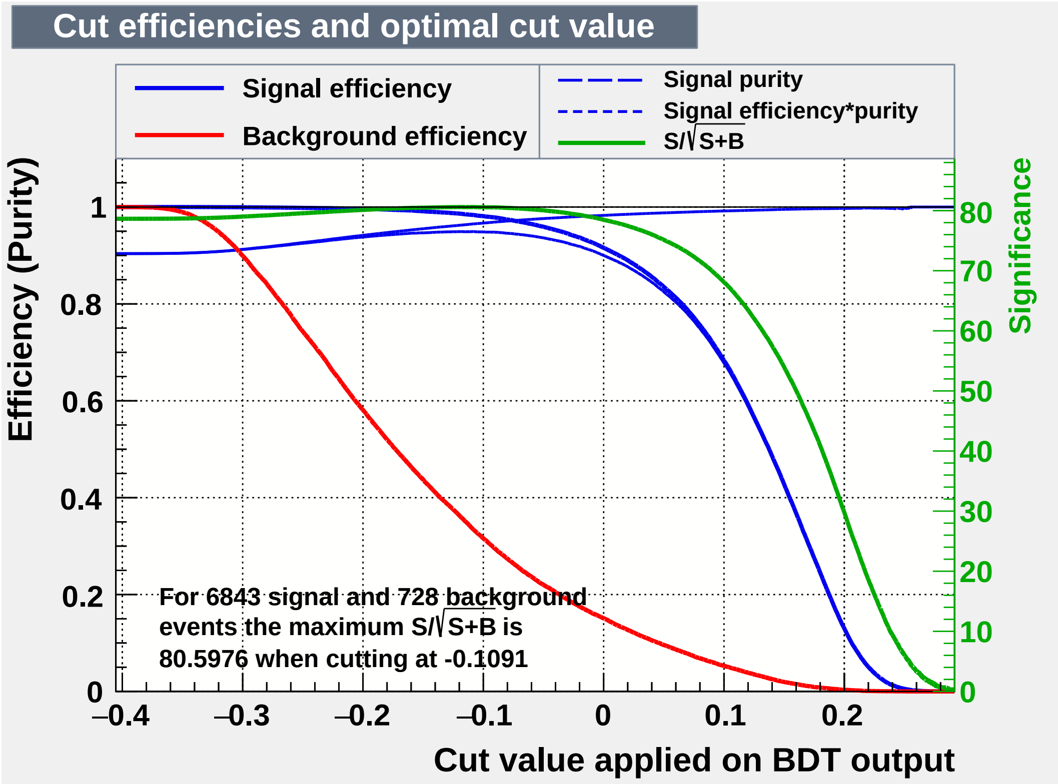

Figure 70: *Optimization of a cut on the BDT output discriminant.*

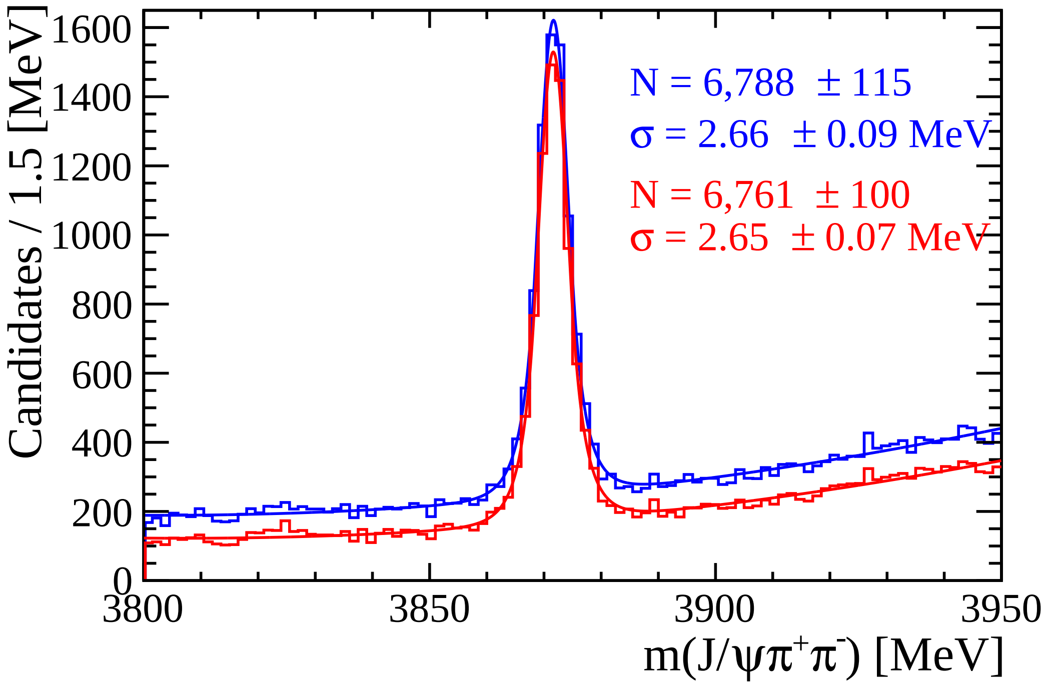

Figure 71: *Fits to the $X(3872)$ mass peak after the default selection (blue) and after the additional cut on the BDT discriminant (red).*

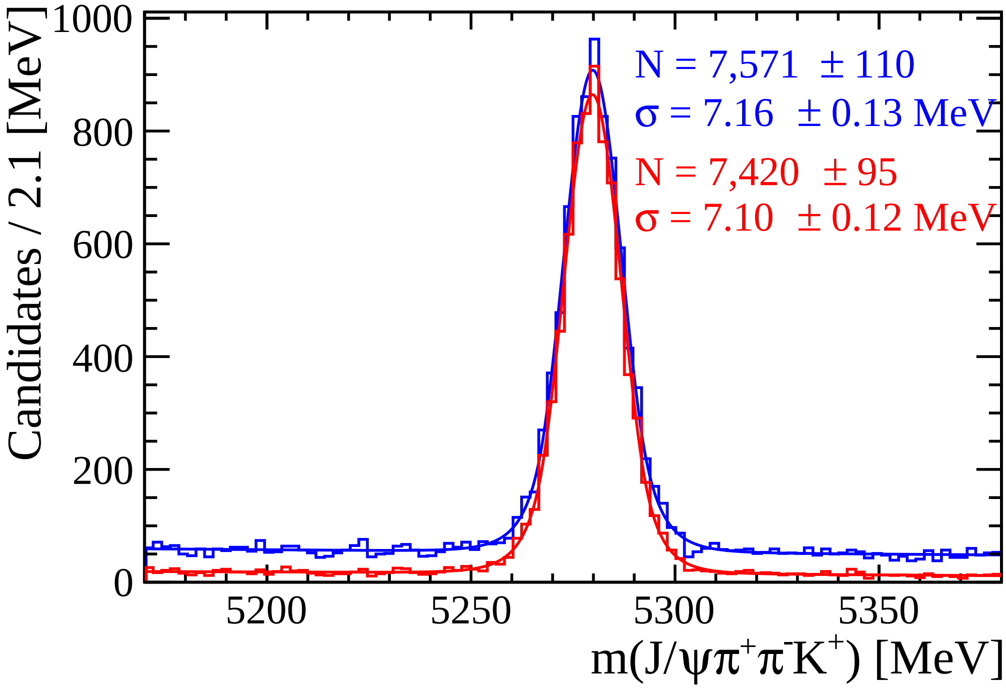

Figure 72: *Fits to B^+ mass peak after the default selection (blue) and after the additional cut on the BDT discriminant (red).*

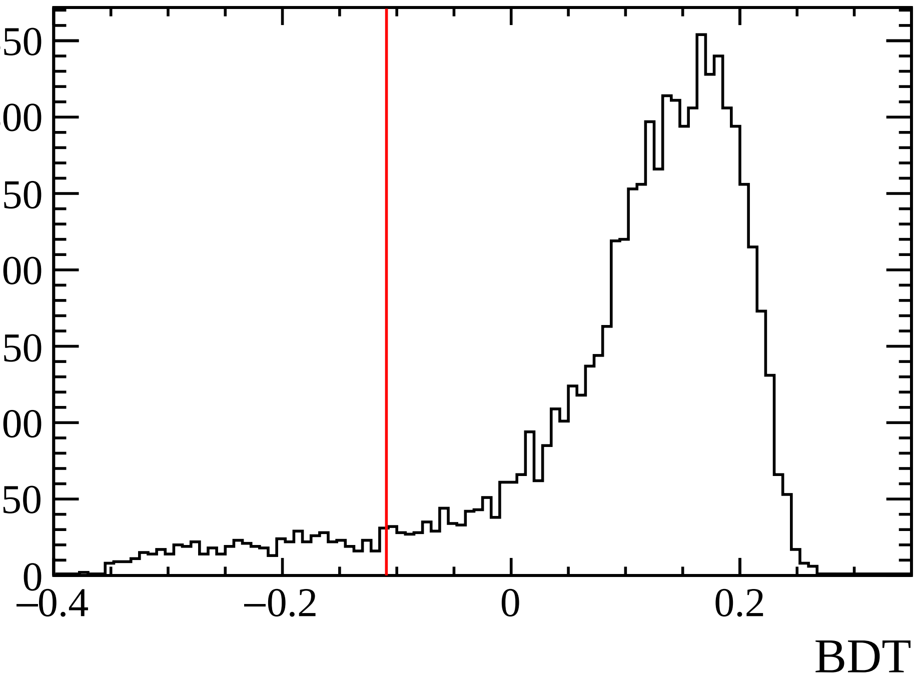

Figure 73: *BDT cut on the data sample. Cut value is* -0.1091.

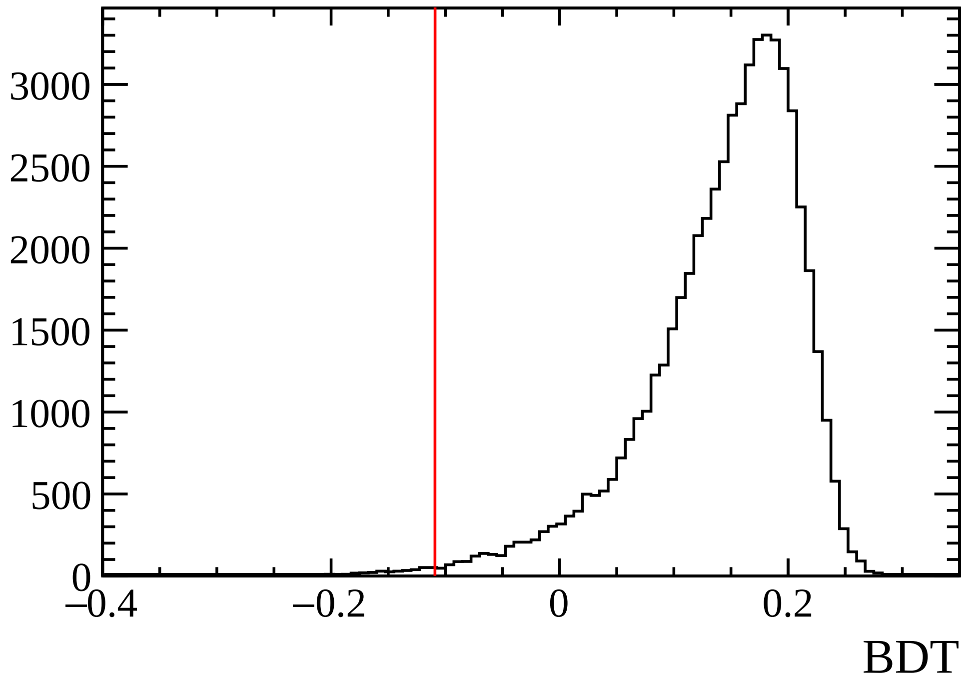

Figure 74: *BDT cut on the MC sample. Cut value is* -0.1091.

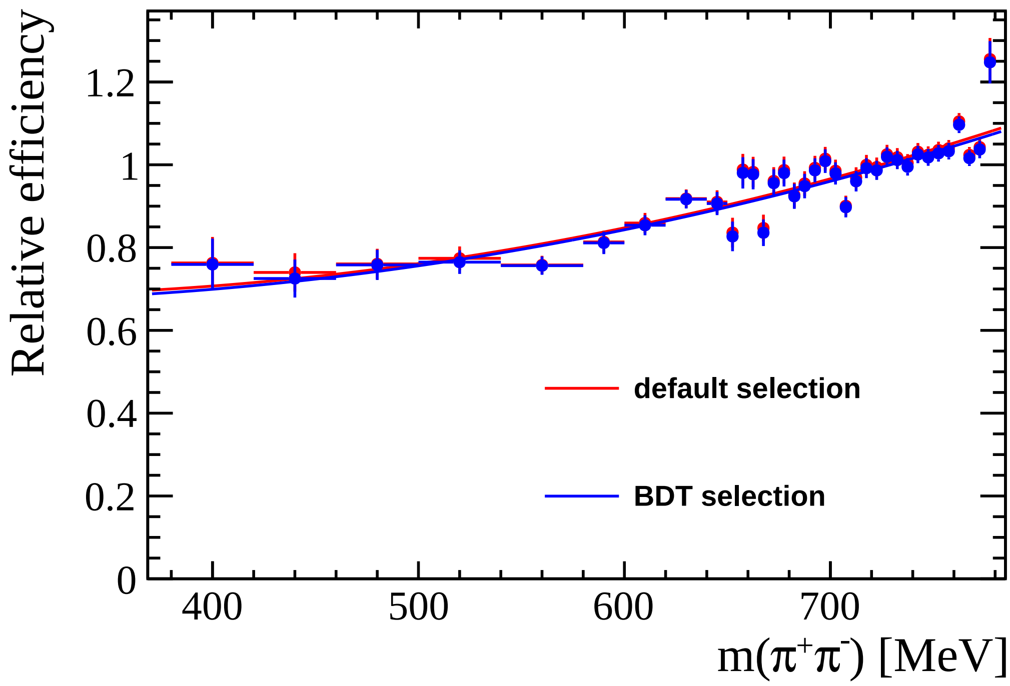

Figure 75: *Variation of the reconstruction efficiency with dipion mass after the BDT cut (blue points), compared to the efficiency with the default cuts (red points). The differences are small.*

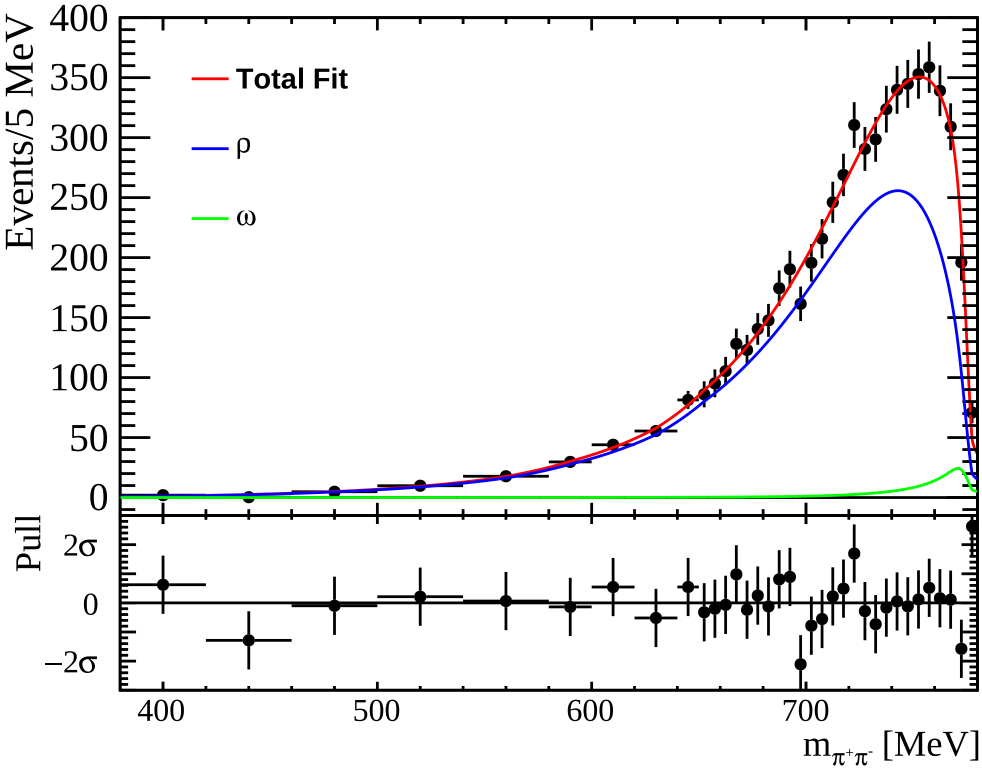

Figure 76: *Fit of the coupled-channel model with the ρ^0 and ω contributions and linear dependence of $\alpha_{2\pi}$ on $m_{\pi\pi}^2$. The BDT cut is applied to this sample.* $\chi^2/\mathrm{NDoF} = 24.6/32$, *$pV = 0.82$ and $P_1 = 0.24 \pm 0.04$.*

18 Systematic uncertainty from hadron identification

The hadron identification cuts in our default analysis (Sec. 5) are very loose: PIDK> -5 for the kaon candidate, PIDK$< +5$ for the pion candidates. The kaon candidate must also have a larger PIDK value, than any of the two pion candidates. In the default approach to the relative efficiency simulation, we rely on PIDK values set by the simulations. Since the cuts are loose, this works fairly well, and the kinematic distributions in the data are well reproduced by the simulations (see Fig. 37), once the B^+ transverse momentum distribution is corrected for as discussed in Sec. 7.

A more aggressive use of hadron identification variables is employed in the BDT data selection performed as a cross-check (Sec. 17). A log of the product of ProbNN variables, K_ProbNNk(1-K_ProbNNpi) Pi1_ProbNNpi(1-Pi1_ProbNNk) Pi2_ProbNNpi(1-Pi2_ProbNNk), is used as one of the inputs to the BDT discriminant. The relative efficiency hardly changes (Fig. 75) and the results from the fit to the dipion mass distribution in the data change very little (Table 9).

As an additional cross check on systematic uncertainty related to the simulations of hadron identification cuts, we replace PIDK values in the simulated events by values sampled from the PDFs extracted for kaons and pions from the calibration data using PIDCalib package. It turns out that following this procedure, kaon transverse momenta in the data are not well reproduced by the simulations even after the $p_T(B^+)$ reweighting (Fig. 77). After additional reweighting of the Monte Carlo sample in $p_T(K)$ (the weight function is shown in Fig. 78), the agreement between the data and simulations is reasonable as shown in Fig. 79. The relative efficiency variation with the dipion mass, is very similar to the one obtained with the default simulations (see Fig. 80 for a comparison). The fit to the dipion mass distribution in the data (Fig. 81), with the relative efficiency simulated using PIDCalib package, is almost identical to the default fit results as shown in Table 9.

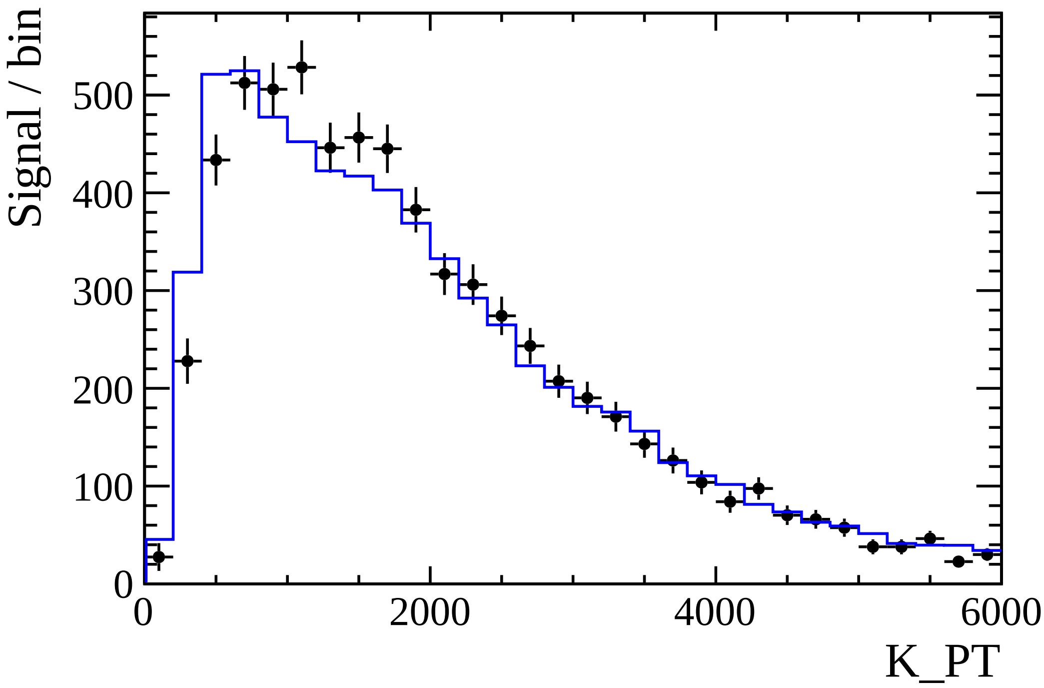

Figure 77: *The distribution of $p_T(K)$ for the data (points with error bars) and for the MC (histogram). The distributions were corrected for the varying bin width. The data points were obtained by fitting the $X(3872)$ peak in the $J/\psi\pi^+\pi^-$ mass distributions for various bins. The MC events were weighted by the run-dependent, dipion-mass dependent, and $p_T(B^+)$ weights. The MC distribution was normalized to the same number of entries as the data.*

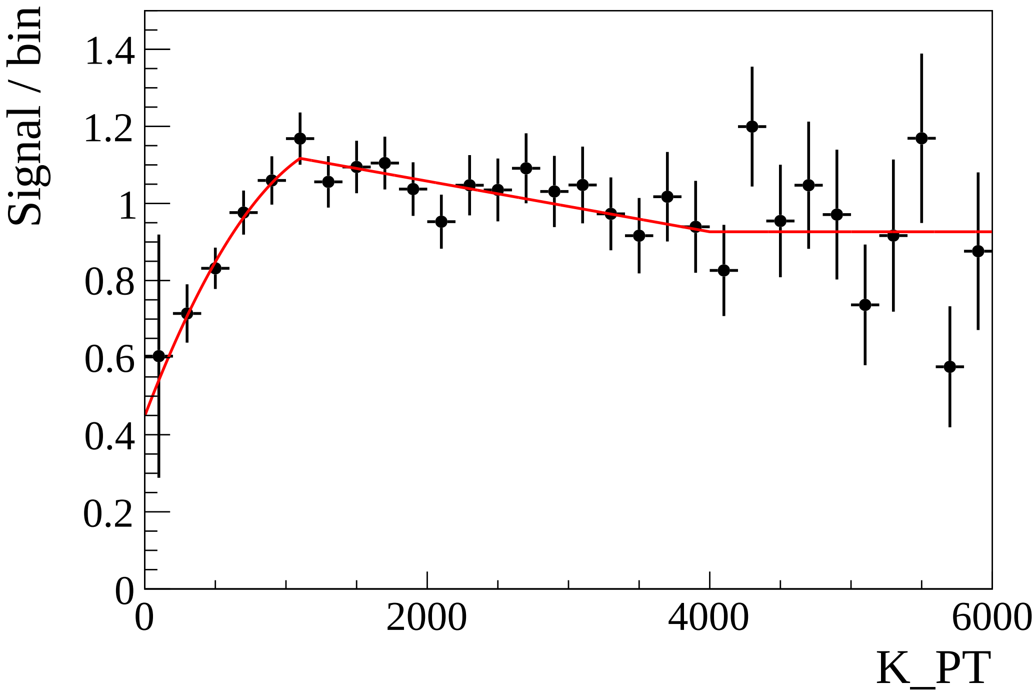

Figure 78: *The ratio of the data and MC distributions of $p_T(K)$ when using PIDcalib package in MC. Fit of a smooth function, used as a correction weight for simulated events, is shown.*

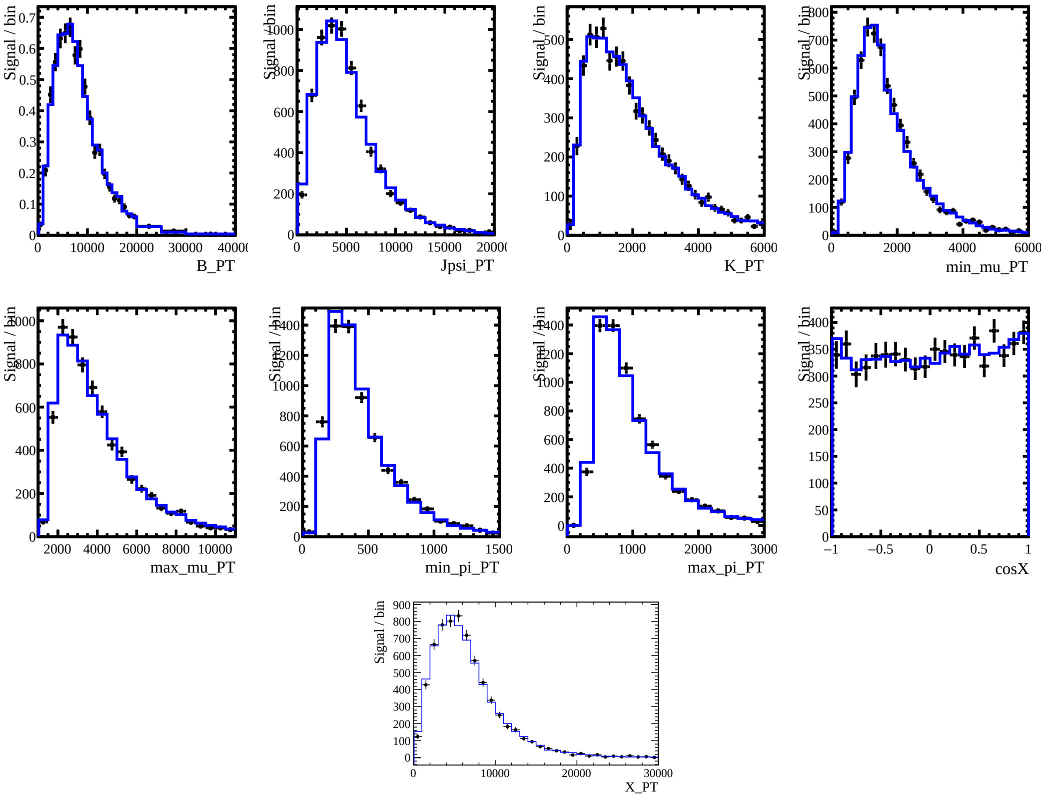

Figure 79: *The distributions of p_T of various reconstructed particles, and of $X(3872)$ helicity angle, for the data (points with error bars) and for the MC (histogram) with use of PIDcalib package. The distributions were corrected for the varying bin width. The data points were obtained by fitting the $X(3872)$ peak in the $J/\psi\pi^+\pi^-$ mass distributions for various bins. The MC events were weighted by the run-dependent, dipion-mass-dependent and $p_T(B^+)$-dependent weights. The MC distributions were normalized to the same number of entries as the data.*

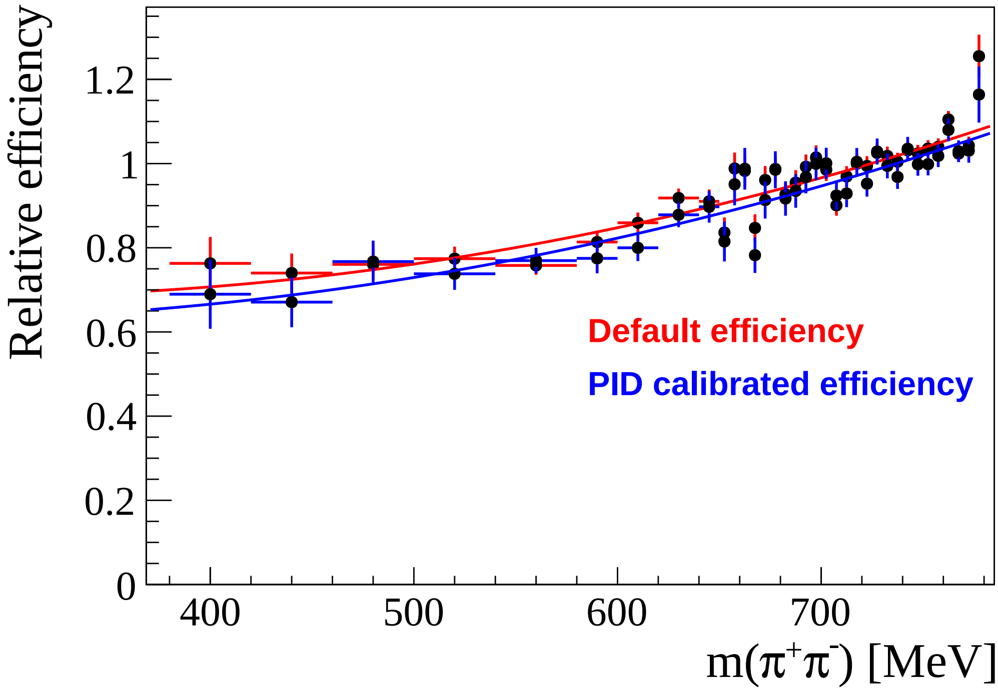

Figure 80: *Variation of the reconstruction efficiency with dipion mass obtained using PIDcalib in the simulations (blue points), compared to the efficiency with the default simulations (red points).*

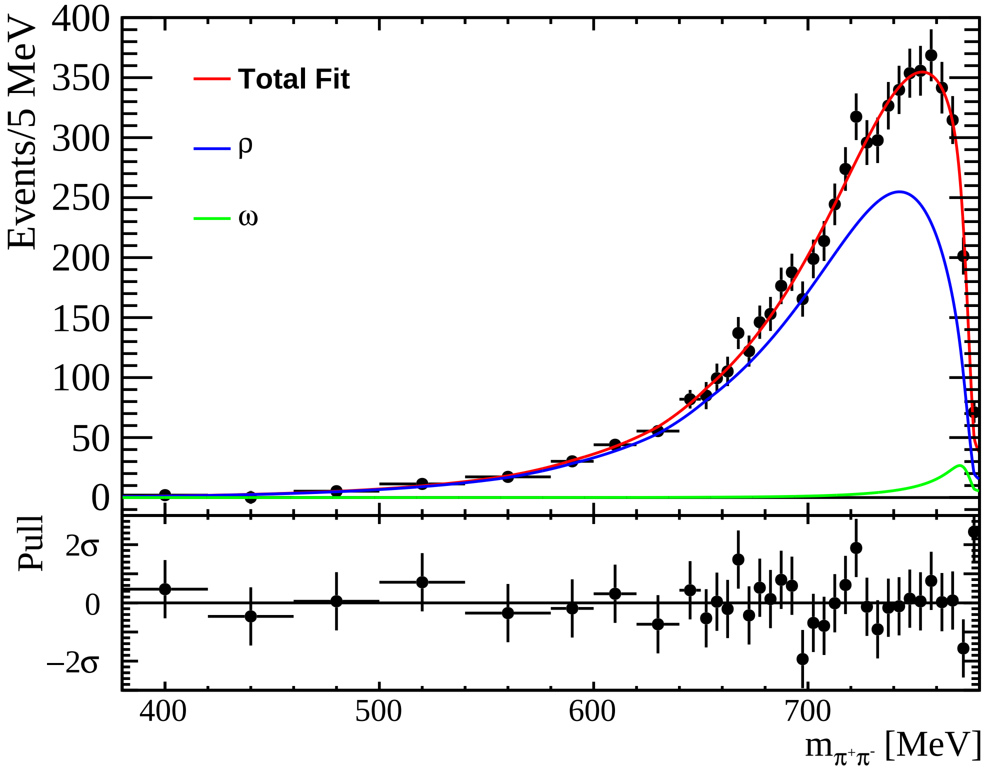

Figure 81: *Fit of the coupled-channel model with the* ρ^0 *and* ω *contributions and linear dependence of* $\alpha_{2\pi}$ *on* $m^2_{\pi\pi}$*. The BDT cut is applied to this sample.* $\chi^2/\mathrm{NDoF} = 24.6/32$*,* $pV = 0.82$ *and* $P_1 = 0.22 \pm 0.04$*.*

19 Mass resolution systematics

By default, we scale the dipion resolution up by a factor of 1.06, as deduced from the visible $X(3872)$ widths in the data and and in the simulations, and discussed in Sec. 8. To explore uncertainty in the dipion mass resolution used in the fits, we vary the scaling factor from 1.0 (no corrections) to 1.14 derived from the ratio of B^+ mass resolutions in the data and in the MC (see Sec. 8). The fits are shown in Figs. 82-83 and the results are given in Tab. 9.

The dipion mass bin which is the most sensitive to the mass resolution effects is in 775-780 MeV range. As an additional systematic variation, we exclude this bin from the fit. The results change by amount comparable to the statistical error from the fit (Fig. 84 and Tab. 9).

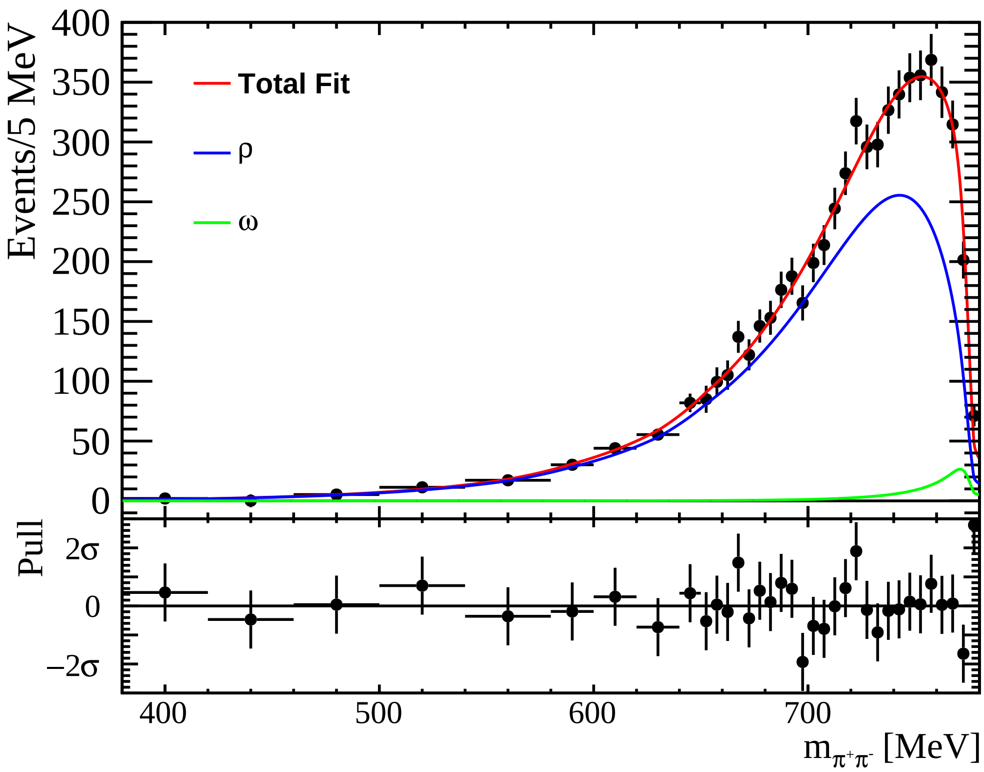

Figure 82: *Fit of the coupled-channel model with the ρ^0 and ω contributions and linear dependence of $\alpha_{2\pi}$ on $m^2_{\pi\pi}$. This fit was performed with the dipion mass resolution taken from simulations without any correction factor.* $\chi^2/\mathrm{NDoF} = 26.6/32$, $pV = 0.74$, $P_1 = 0.23 \pm 0.05$.

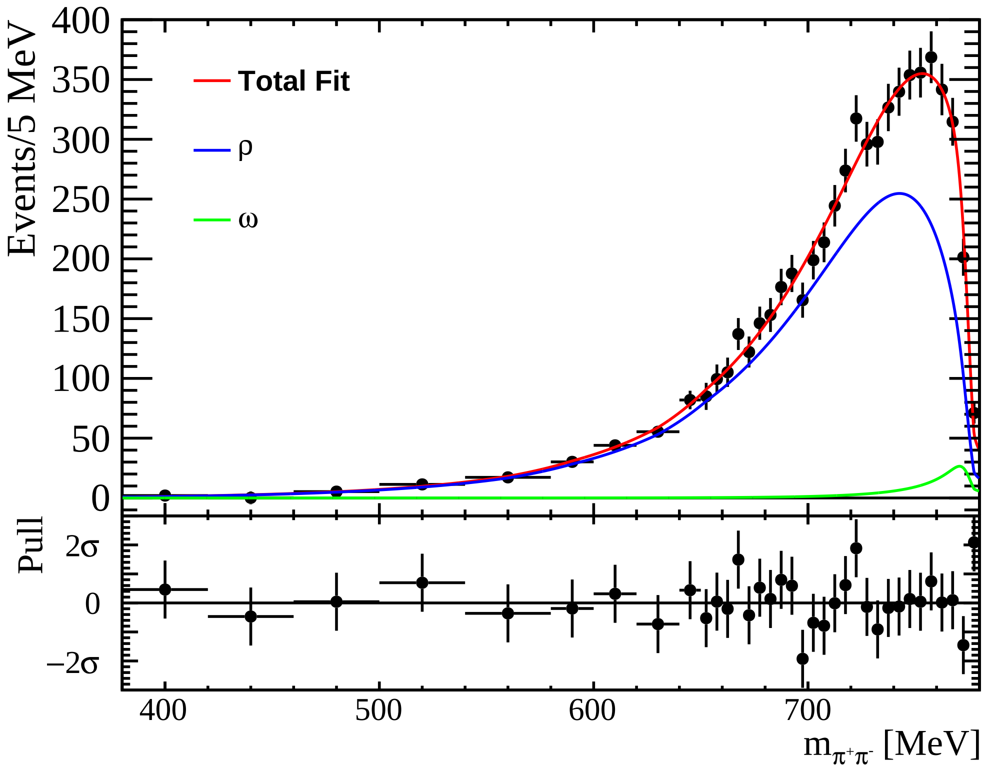

Figure 83: *Fit of the coupled-channel model with the* ρ^0 *and* ω *contributions and linear dependence of* $\alpha_{2\pi}$ *on* $m_{\pi\pi}^2$*. This fit was performed with the dipion mass resolution scaled up by 14%.* $\chi^2/\mathrm{NDoF} = 22.6/32$, $pV = 0.89$, $P_1 = 0.23 \pm 0.05$.

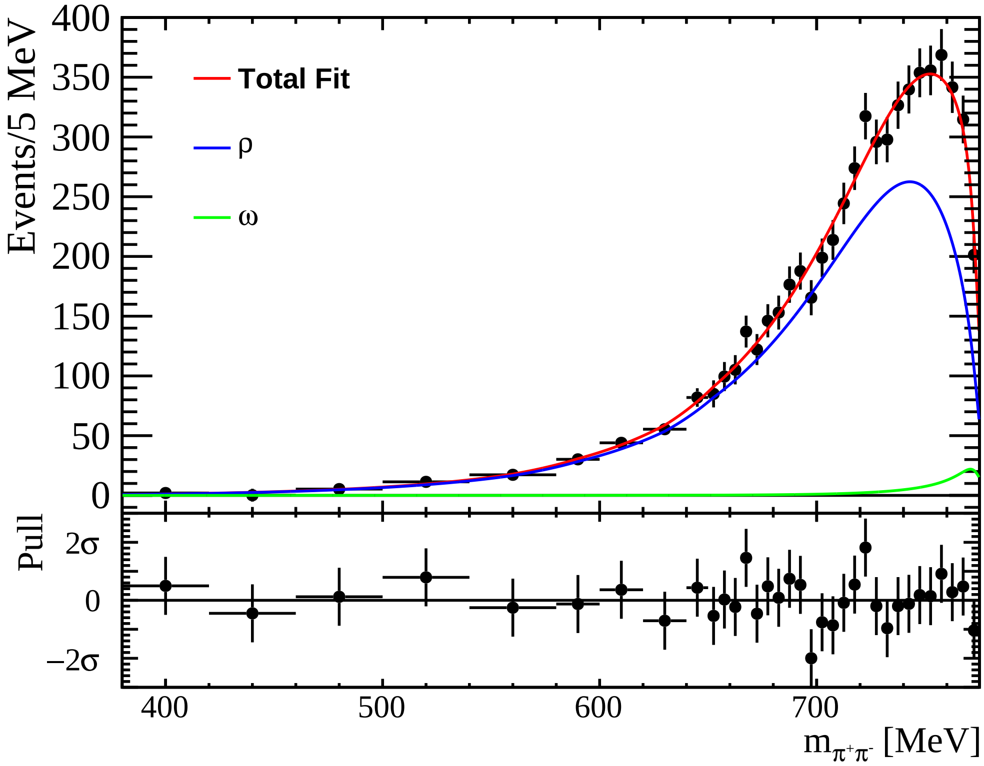

Figure 84: *Fit of the coupled-channel model with the* ρ^0 *and* ω *contributions and linear dependence of* $\alpha_{2\pi}$ *on* $m^2_{\pi\pi}$. *This fit was performed in reduced mass range from* $380 MeV$ *to* $775 MeV$. $\chi^2/\mathrm{NDoF} = 18.0/31$, $pV = 0.97$, $P_1 = 0.24 \pm 0.05$.

20 $X(3872)$ lineshape systematics

In the default analysis, we use double-sided Crystal Ball lineshape as the $X(3872)$ signal PDF in $m_{J/\psi\pi\pi}$ mass distribution when extracting the dipion mass distribution from the data (Sec. 6). This shape describes the $X(3872)$ mass peak well in the data and in the simulations. In this section, we present results obtained with simple Gaussian lineshape. Even though this lineshape model does not describe the simulations well (Fig. 85), the results depend only on a ratio of $X(3872)$ signal yield in the data and in the simulations (via efficiency corrections), thus some deficiencies of this model cancel out. This approach sets a conservative bound on how much the lineshape assumptions can matter for the physics results.

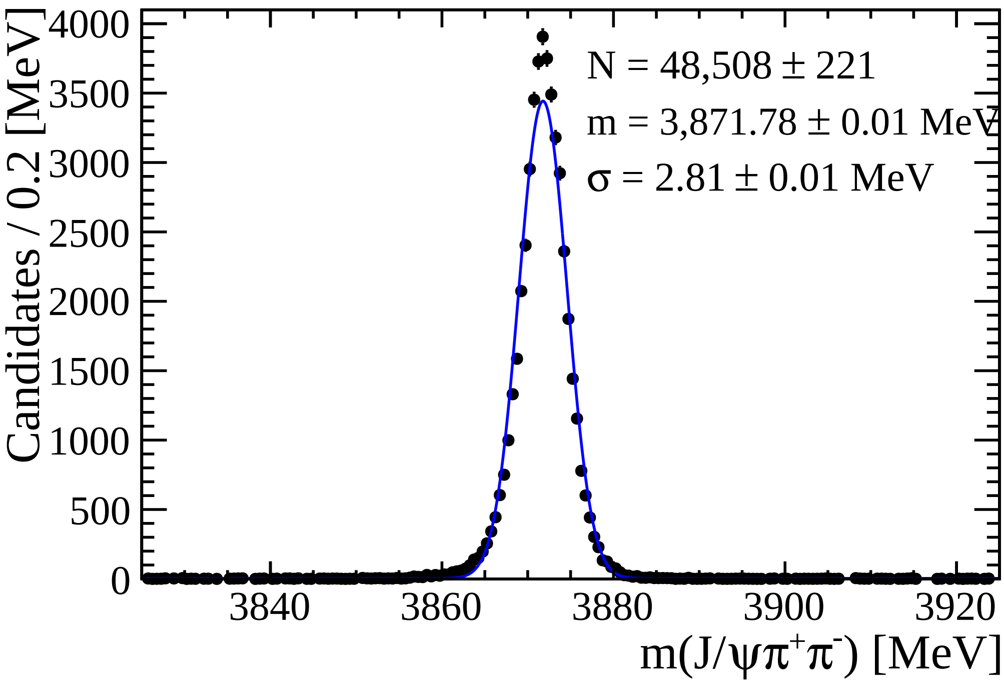

Figure 85: *Fit to the $J/\psi\pi^+\pi^-$ distribution in the signal simulations, after the 2σ B^+ mass cut, and with the PV, J/ψ and B^+ mass constraints. We used Gaussian function for the signal peak and flat background. The blue line represents the total fit. Compare to fit with the double-sided Crystal Ball lineshape shown in Fig. 42.*

The Gaussian fit to the $X(3872)$ peak in the data is shown in Fig. 86. The peak mass value and σ obtained in this fit, are used in 2D fits to $m_{J/\psi\pi\pi}$ vs. $m_{\pi\pi}$, in bins of $m_{\pi\pi}$. A sample of such fits in projection onto $m_{J/\psi\pi\pi}$ is shown in Fig. 87. The efficiency dependence on $m_{\pi\pi}$ obtained by using Gaussian shape in 2D fits to MC is shown in Fig. 88. The fit to such obtain dipion mass spectrum with ρ^0 and ω contributions is shown in Fig. 89, and with ρ^0 contribution alone in Fig. 90. The numerical results are shown in Table 9 and are on par with the other systematic uncertainties.

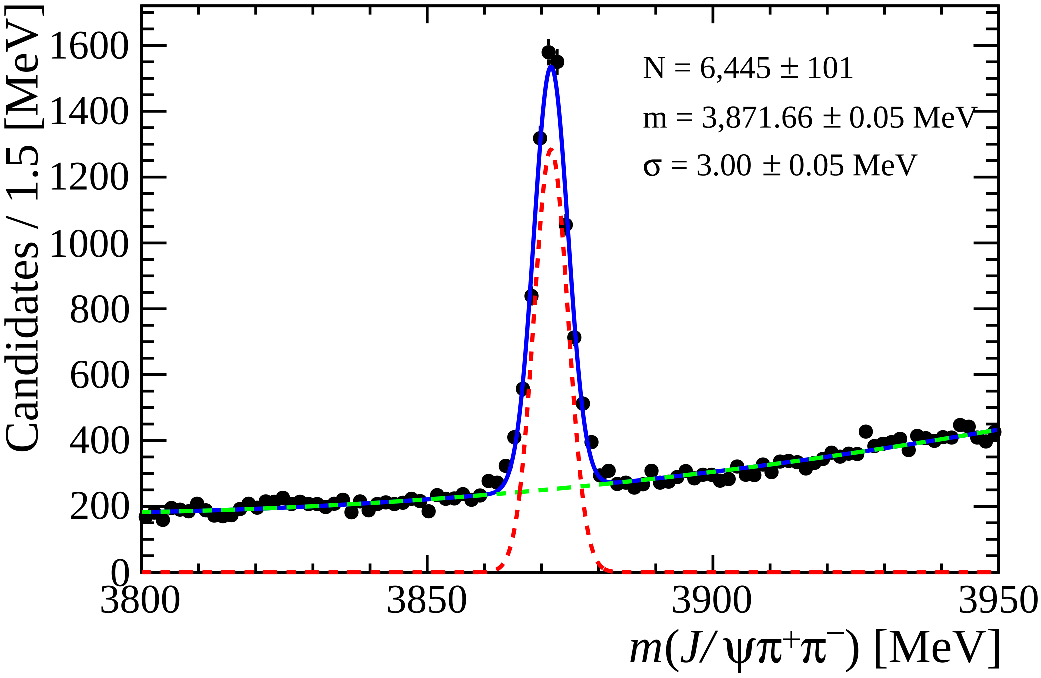

Figure 86: *The distribution of* $m_{J/\psi\pi^+\pi^-}$ *with the* 2σ B^+ *mass signal cut, with the PV,* J/ψ *and* B^+ *mass constraints, fit with a Gaussian for the signal, and quadratic polynomial for the background. The blue line represents the total fit, red is the signal component, and the dashed-green is the background. Compare to the fit with the double-sided Crystal Ball lineshape in Fig. 30.*

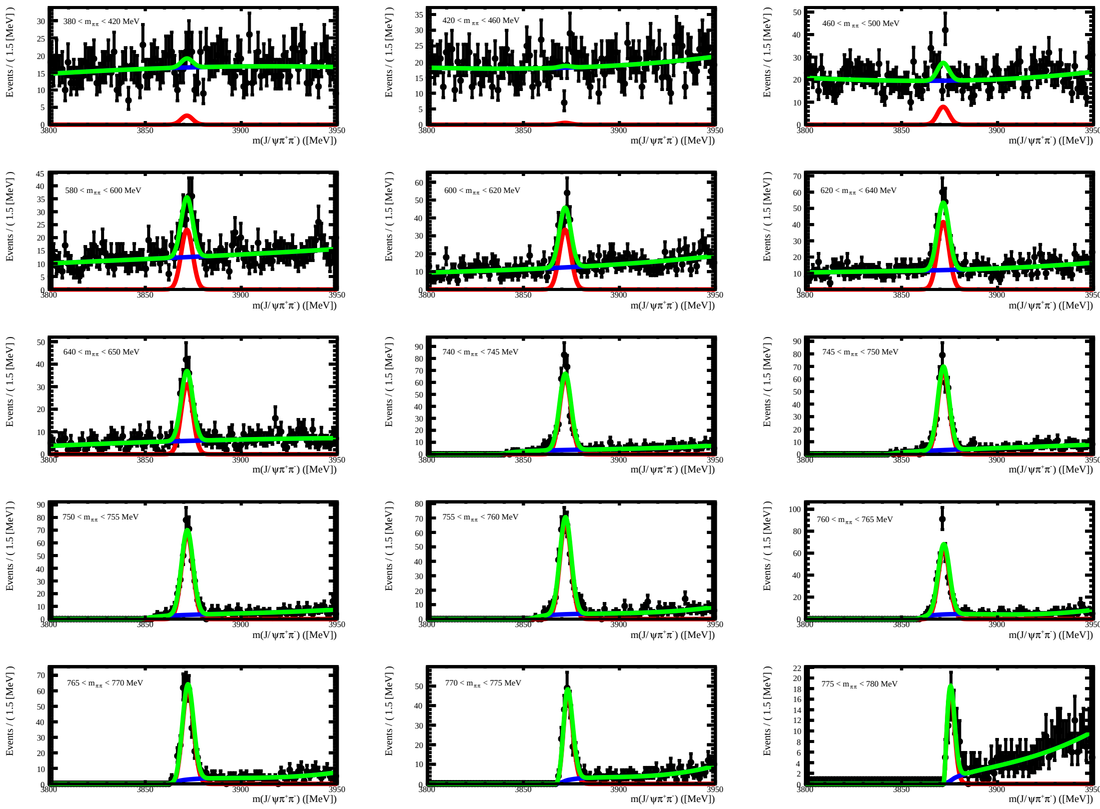

Figure 87: *Projections of unbinned fits to $m_{J/\psi\pi\pi}$ vs. $m_{\pi\pi}$, with Gaussian $X(3872)$ shape, in different $m_{\pi\pi}$ bins, onto the $m_{J/\psi\pi\pi}$ axis. The total fit, the $X(3872)$ signal and the background components are shown by the green, red and blue lines, respectively. Compare to the fits shown done with double-sideded Crystal Ball lineshape in Fig. 33.*

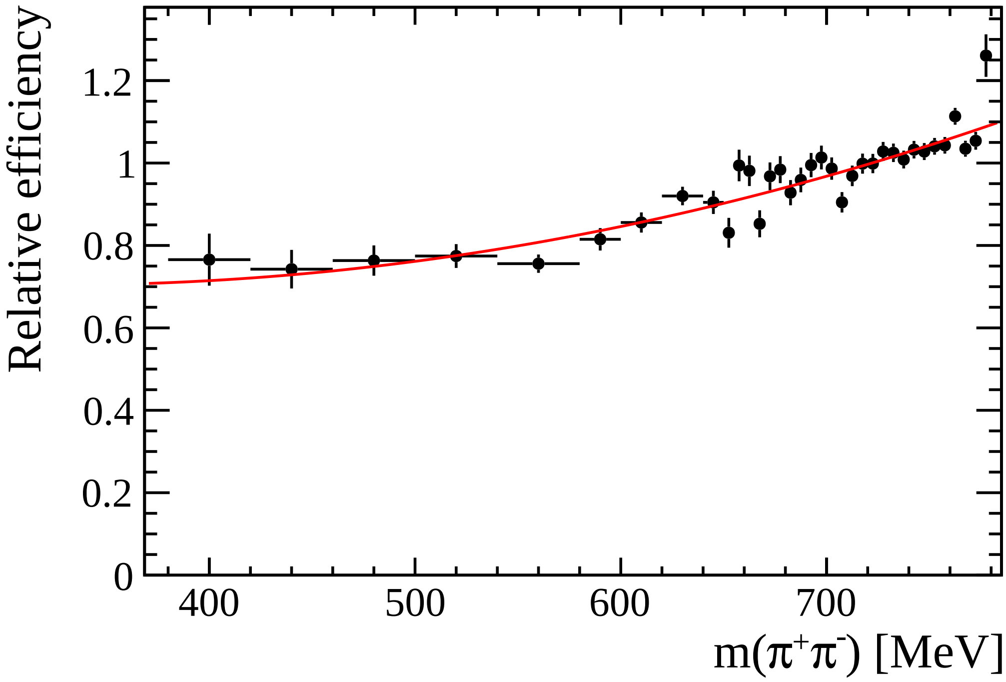

Figure 88: *Variation of the reconstruction efficiency with dipion mass obtained using Gaussian lineshape for $X(3872)$. Units of efficiency are arbitrarily chosen to be close to 1 near 700 MeV, as only the relative variation matters in this analysis. Compare to the efficiency obtained with the double-sided Crystal Ball lineshape in Fig. 43.*

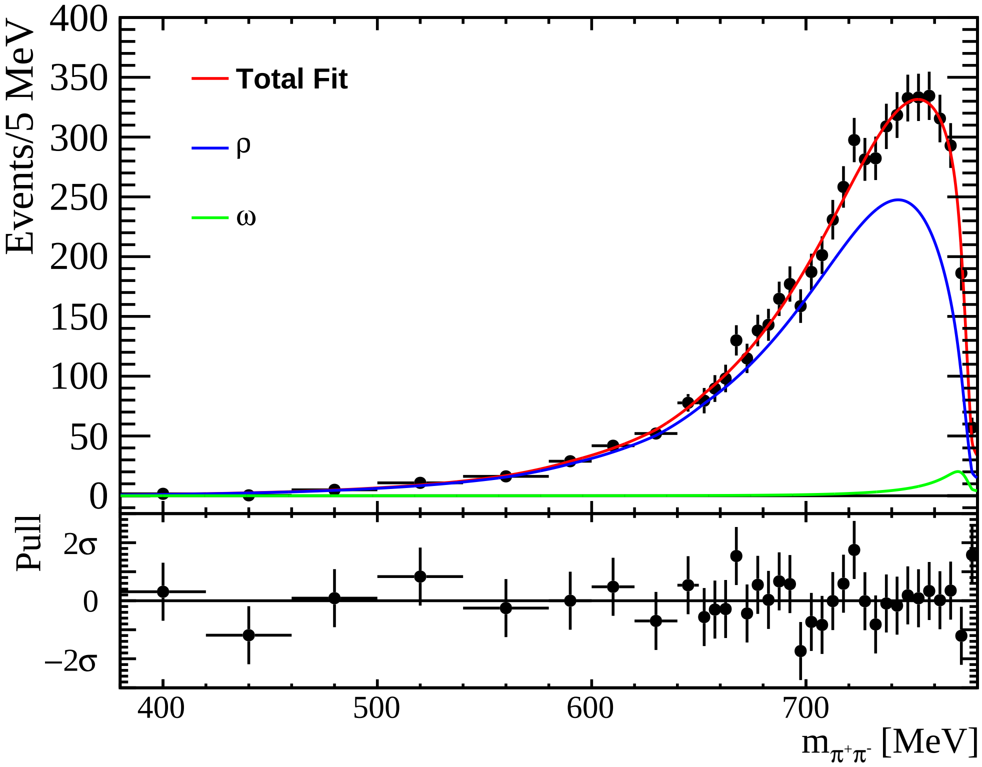

Figure 89: *Fit of the coupled-channel model to the mass spectrum obtained using Gaussian* $X(3872)$ *shape, with the* ρ^0 *and* ω *contributions and linear dependence of* $\alpha_{2\pi}$ *on* $m_{\pi\pi}^2$. $\chi^2/\mathrm{NDoF} = 20.0/32$, $pV = 0.95$, *and* $P_1 = 0.242 \pm 0.045$.

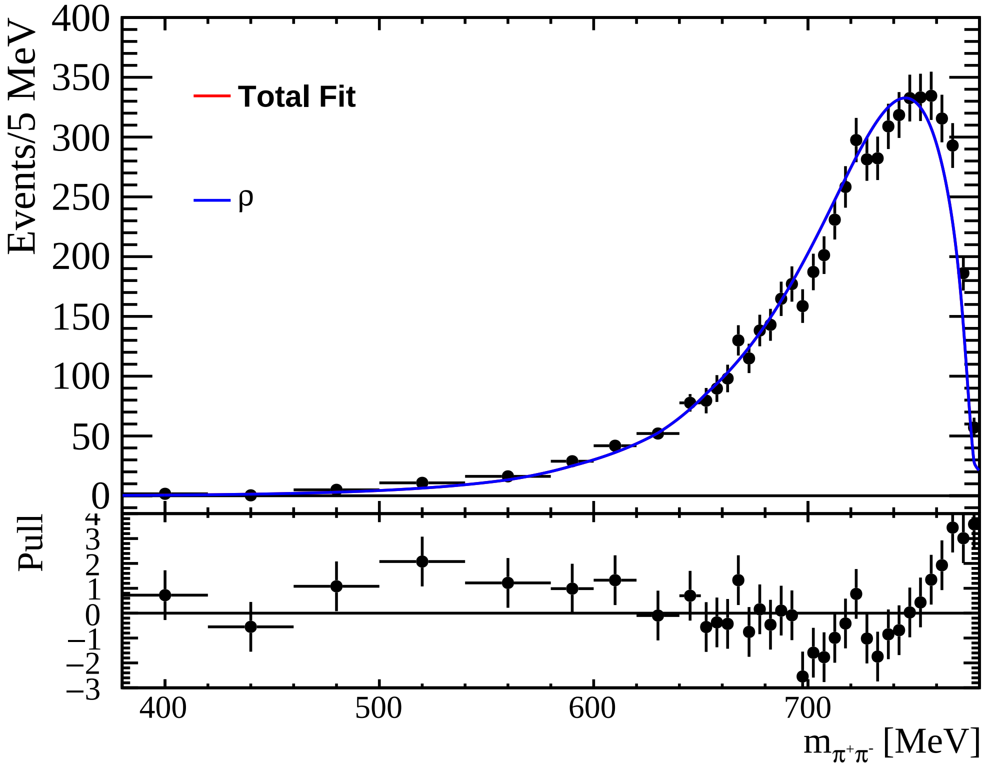

Figure 90: *Fit of the coupled-channel model to the mass spectrum obtained using Gaussian* $X(3872)$ *shape, with the* ρ^0 *contribution alone and linear dependence of* $\alpha_{2\pi}$ *on* $m^2_{\pi\pi}$*.* $\chi^2/\mathrm{NDoF} = 72.8/33$*,* $pV = 8 \times 10^{-5}$*, and* $P_1 = 0.48 \pm 0.04$*.*

21 Gounaris-Sakurai model

A high statistics data on $\rho^0-\omega$ interference in $e^+e^-\to\pi^+\pi^-$ reaction was successfully described by the BaBar collaboration [4] by using Gounaris-Sakurai model of the ρ^0 resonance [2],

$$BW_\rho^{\mathrm{GS}}(s,m_\rho,\Gamma_\rho)=\frac{m_\rho^2\left[1+d(m_\rho)\Gamma_\rho/m_\rho\right]}{m_\rho^2-s+f(s,m_\rho,\Gamma_\rho)-i\,m_\rho\Gamma(s,m_\rho,\Gamma_\rho)}, \tag{43}$$

where,

$$\Gamma(s,m,\Gamma)=\Gamma\frac{m}{\sqrt{s}}\left[\frac{k(s)}{k(m^2)}\right]^3, \tag{44}$$

$$d(m)=\frac{3}{\pi}\frac{m_\pi^2}{k^2(m^2)}\log\left[\frac{m+2k(m^2)}{2m_\pi}\right]+\frac{m}{2\pi k(m^2)}-\frac{m_\pi^2 m}{\pi k^3(m^2)}, \tag{45}$$

$$f(s,m,\Gamma)=\frac{\Gamma m^2}{k^3(m^2)}\left[k^2(s)\left[h(s)-h(m^2)\right]+(m^2-s)k^2(m^2)h'(m^2)\right], \tag{46}$$

$$k(s)=p(s), \tag{47}$$

$$h(s)=\frac{2}{\pi}\frac{k(s)}{\sqrt{s}}\log\left[\frac{\sqrt{s}+2k(s)}{2m_\pi}\right], \tag{48}$$

and $h'(s)$ is a derivative of $h(s)$, which we calculate numerically. This is an alternative formulation to the parameterization of the ρ^0 line shape with the mass-dependent width equipped with the Blatt-Weisskopf form-factor, which we used in Sections 10 and 11. To include the $P-$wave momentum barrier in ρ^0 decay, we set

$$M=\frac{k(s)}{k(m_\rho)}\,BW_\rho^{\mathrm{GS}}(s,m_\rho,\Gamma_\rho). \tag{49}$$

Fit of this ρ^0 shape to our data, is better than the fit of the Breit-Wigner shape described in Sec. 10, however, it still fails to describe the data as illustrated in Fig. 91.

Including ω contribution by adding its Breit-Wigner amplitude improves the fit, but still gives a bad quality fit $pV=3\times10^{-5}$ (see Fig. 92).

A good quality fit to the data is achieved following the prescription used by BaBar[14] [4],

$$M=\frac{k(s)}{k(m_\rho)}BW_\rho^{\mathrm{GS}}(s,m_\rho,\Gamma_\rho)\,\left[1+A_\omega\,e^{i\phi_\omega}\,BW_\omega(s,m_\omega,\Gamma_\omega)\right], \tag{50}$$

$$BW_\omega(s,m_\omega,\Gamma_\omega)=\frac{m_\omega^2}{m_\omega^2-s-im_\omega\Gamma_\omega}. \tag{51}$$

[14] Following the work by BaBar, we use a simple Breit-Wigner amplitude for ω here, with mass dependence of the width neglected, which hardly matters for such a narrow resonance. We also use ρ^0 and ω masses and widths used by BaBar in their fit to $e^+e^-\to\pi^+\pi^-(\gamma)$ data (Table VI in Ref. [4]).

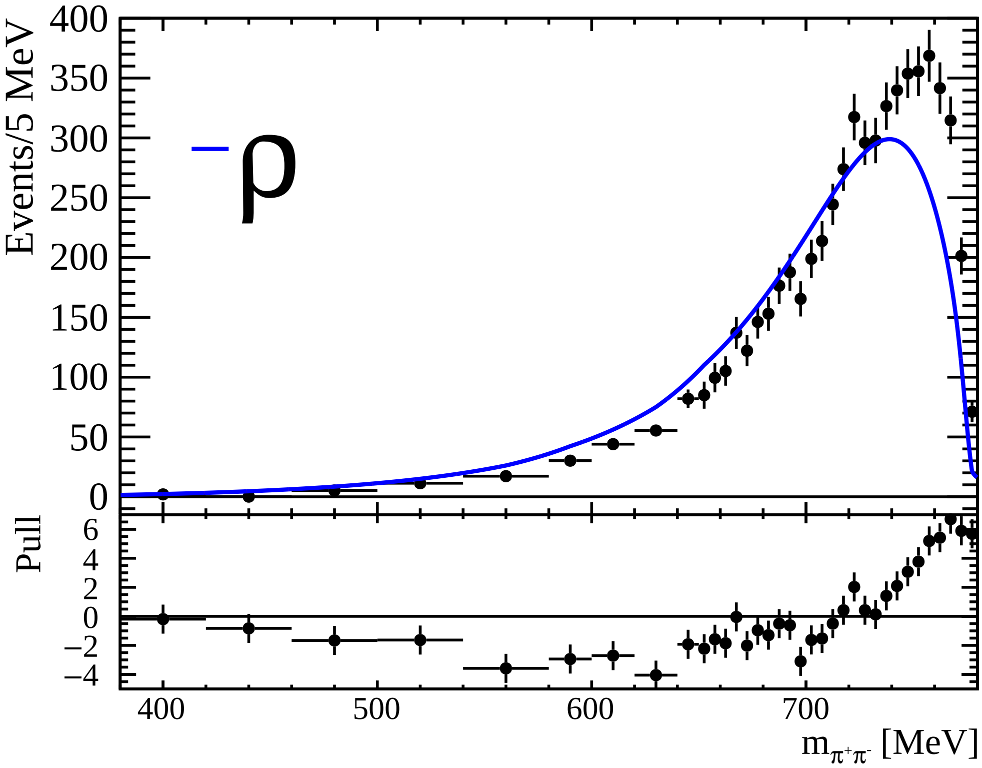

Figure 91: *Fit of ρ^0 Gounaris-Sakurai model to the data. The fit qualities are* $\chi^2/\mathrm{NDoF} = 290.0/34$ *and* $pV = 2 \times 10^{-42}$.

In fact, this form arises from the coupled-channel approach as discussed in Sec. 11, when the diagonal coupling of ω to $\pi^+\pi^-$ is neglected. Using this approximate form of the coupled-channel approach, allows us to use Gounaris-Sakurai model for the ρ shape, instead of the ρ^0 pole with the Blatt-Weisskopf form factor. Production couplings are expected to be real in the coupled-channel approach, thus we set ϕ_ω to zero. In fact, the BaBar data were consistent with this expectation ($\phi_\omega = -0.011 \pm 0.037$ radians [4]). The fit quality to our data is good with $\chi^2/\mathrm{NDoF} = 34.3/33$ and $pV = 0.40$ (see Fig. 93). The $A_\omega = 0.0232 \pm 0.0016$ is 15.0σ away from zero, and by an order of magnitude larger than when ρ^0 and ω are produced in $e^+e^- \to \pi^+\pi^-$ reaction, 0.001644 ± 0.000061 [4], which is perhaps not surprising given that the $X(3872) \to \rho^0 J/\psi$ decay violates isospin. Yet even larger ρ^0 suppression had been expected in case the $X(3872)$ would have been an ordinary isoscalar charmonium state (see Sec. 4 and 13). The ω fractional contributions, overall $R_\omega^{all} = 0.272 \pm 0.014$, and excluding the interference of the two terms $R_\omega^{0} = 0.034 \pm 0.004$, are larger than in our default coupled-channel model (Sec. 13). The ω significance determined from the χ^2-difference method is 16.0σ.

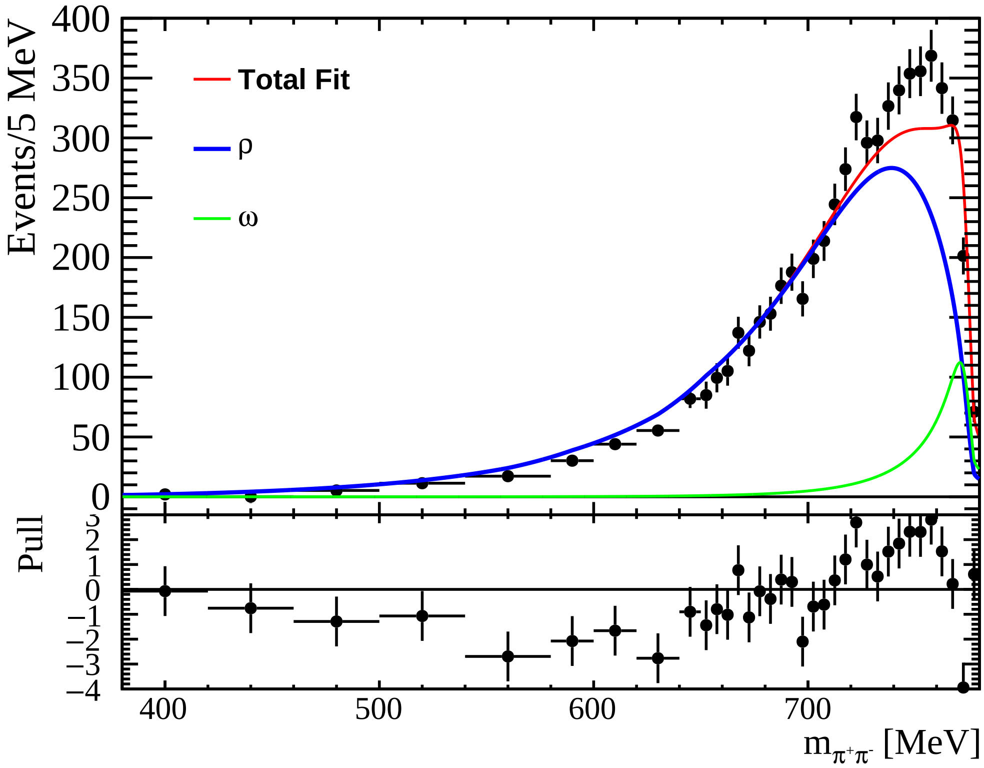

Figure 92: *Fit of Gounaris-Sakurai model of* ρ^0 *plus a simple Breit-Wigner formula for* ω *(Eq. 51) to the data. The relative phase was set to* 95^0 *(the fit is insensitive to it as discussed in Sec. 10). The fit qualities are* $\chi^2/\mathrm{NDoF} = 90.0/33$ *and* $pV = 3 \times 10^{-7}$.

The results are fairly insensitive to the value of the ϕ_ω. They don't change at all when its value is fixed to -0.011 radians. When we fit this parameter to our data, we obtain a value consistent with zero, $-0.40^{+0.41}_{-0.33}$ rad, with no improvements to the fit quality ($\chi^2/\mathrm{NDoF} = 33.4/32$, $pV = 0.40$). In such a fit ω parameters are poorly determined ($A_\omega = 0.026 \pm 0.005$, $R_\omega^{all} = 0.277 \pm 0.029$, $R_\omega^{0} = 0.047 \pm 0.017$).

The BaBar collaboration found a significant contribution of the ρ' resonance, $A_{\rho'} = 0.158 \pm 0.018$, $\phi_{\rho'} = 3.76 \pm 0.10$ rad, when adding the $A_{\rho'}\, e^{i\phi_{\rho'}}\, BW^{\mathrm{GS}}_{\rho'}(s, m_{\rho'}, \Gamma_{\rho'})$ term to Eq. 50 [4]. We fix the ρ' mass, width and phase to the values determined from the BaBar data [4], and obtain a fit quality, $\chi^2/\mathrm{NDoF} = 24.8/32$, $pV = 0.81$ (see Fig. 94), matching the fit quality of our nominal fit. The ρ' significance is 3.1σ from the χ^2-difference method (Wilks theorem). The production parameter, $A_{\rho'} = 0.302 \pm 0.099$, is also 3.0σ away from zero, and consistent within the large errors with the value obtained by the fit to the BaBar data (see above). The ω significance is 7.8σ from the Wilks theorem. Its production parameter, $A_\omega = 0.0171 \pm 0.0024$ is 7.2σ away from zero. The ω fractional contributions

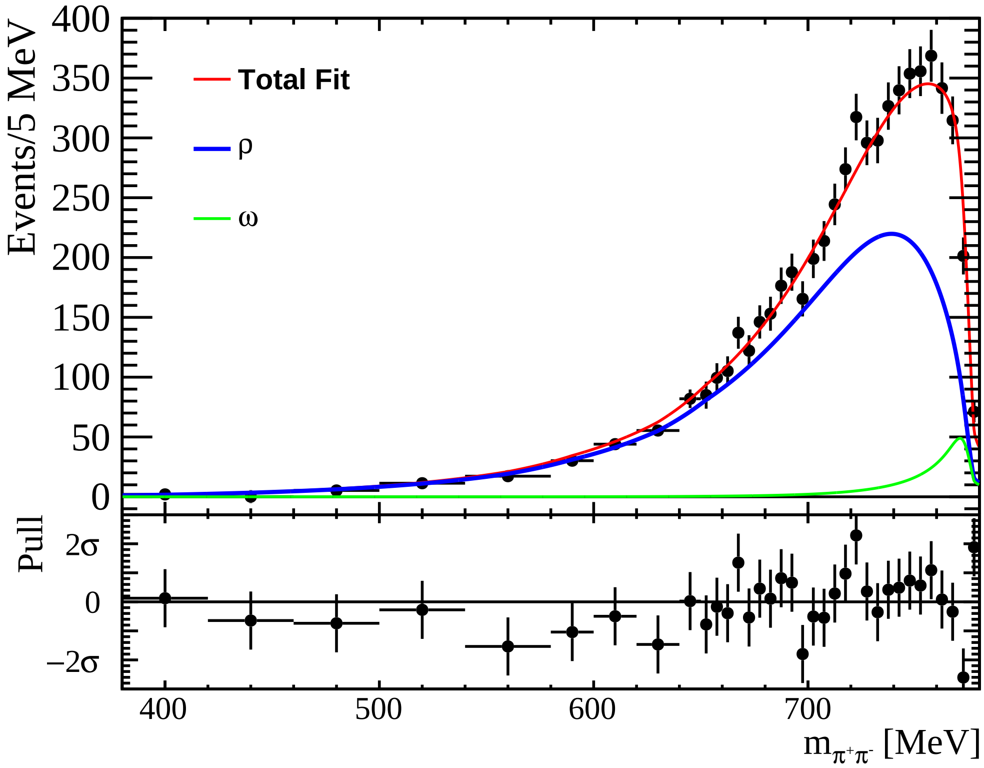

Figure 93: *Fit of Gounaris-Sakurai model of* ρ^0 *coupled with* ω *via Eq. 50. The relative phase was set to zero. The fit qualities are* $\chi^2/\mathrm{NDoF} = 34.4/33$ *and* $pV = 0.40$.

are now more consistent with our default model, $R_\omega^{all} = 0.221 \pm 0.024$, $R_\omega^{0} = 0.021 \pm 0.005$. In here, $R_\omega^{all} = 1 - R_{\rho+\rho'}$, where $R_{\rho+\rho'} = 0.780 \pm 0.023$ is the coherent fit fraction of ρ^0 and $\rho^{0\prime}$ together. Individual fit fractions are $R_\rho = 0.833 \pm 0.037$ and $R_{\rho'} = 0.013 \pm 0.008$. We include this fit when evaluating the systematic uncertainty of our results (see Table 9).

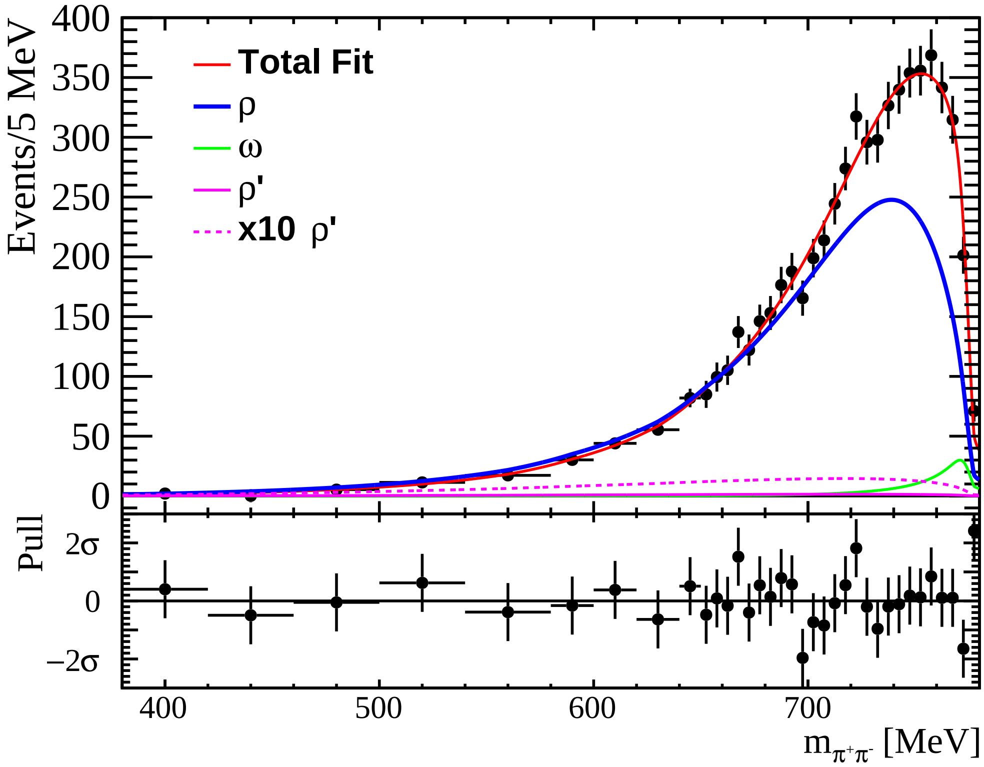

Figure 94: *Fit of Gounaris-Sakurai (GS) model of* ρ^0 *coupled with* ω *via Eq. 50, and* ρ^0*' in the GS representation added to the fit. The relative phase of* ω *was set to zero. The relative phase of* ρ^0*' was set to* 3.76 *rad [4]. The fit qualities are* $\chi^2/\mathrm{NDoF} = 24.8/32$ *and* $pV = 0.81$.

22 Summary of systematic variations

The summary of the results, including all systematic variations and cross-checks is given in Table 9. We set the systematic errors from the largest variations found in the table. For significance of the ω contribution, we take the smallest number found, excluding the division of the data into subsamples. The final result, including the systematic error is given in the last row.

Table 9: *Summary of systematic studies and cross-checks. Numbers in italic font do not contribute to the total systematic uncertainties.*

Fit type	χ^2/NDoF	p-value	R^{all}_{ω}	R^{0}_{ω}	$R^{0}_{\omega/\rho}$	ω significance	
						$\sqrt{\Delta\chi^2}$	$\frac{A}{\Delta A}$
Default	24.7/32	0.82	0.214 ± 0.023	0.019 ± 0.004	0.025 ± 0.006	8.1σ	8.6σ
$P_2 \neq 0$	24.6/31	0.78	0.206 ± 0.035	0.018 ± 0.006	0.023 ± 0.009	*5.5σ*	*4.7σ*
Free m_{ρ}	24.7/31	0.78	*0.202 ± 0.301*	*0.017 ± 0.064*	*0.022 ± 0.090*	*2.5σ*	*0.7σ*
Free Γ_{ρ}	24.7/31	0.78	*0.207 ± 0.053*	*0.018 ± 0.009*	*0.023 ± 0.013*	*5.3σ*	*3.3σ*
$R = 1.3$ GeV^{-1}	24.7/32	0.82	0.216 ± 0.022	0.020 ± 0.004	0.026 ± 0.006	8.2σ	8.7σ
$R = 1.6$ GeV^{-1}	24.7/32	0.82	0.212 ± 0.023	0.019 ± 0.004	0.025 ± 0.006	8.0σ	8.5σ
$R_{prod} = 0$ GeV^{-1}	24.7/32	0.82	0.209 ± 0.023	0.019 ± 0.004	0.024 ± 0.006	7.9σ	8.4σ
$R_{prod} = 30$ GeV^{-1}	24.6/32	0.82	0.229 ± 0.022	0.021 ± 0.004	0.028 ± 0.006	8.7σ	9.0σ
NR prod. of 2π	24.7/32	0.82	0.214 ± 0.022	0.019 ± 0.004	0.025 ± 0.006	8.1σ	7.1σ
ρ'	25.1/32	0.80	0.209 ± 0.023	0.018 ± 0.004	0.024 ± 0.006	8.1σ	8.6σ
simple $\rho_{3\pi}(s)$	24.7/32	0.82	0.217 ± 0.023	0.020 ± 0.005	0.026 ± 0.007	8.1σ	8.6σ
$g^2_{\omega\to 2\pi} = 0$	24.7/32	0.82	0.214 ± 0.021	0.019 ± 0.004	0.025 ± 0.006	8.1σ	8.6σ
D-wave free	24.5/31	0.79	0.210 ± 0.029	0.017 ± 0.005	0.021 ± 0.007	7.8σ	7.6σ
D-wave fixed at 4%	24.5/32	0.82	0.208 ± 0.023	0.018 ± 0.004	0.023 ± 0.006	7.9σ	8.3σ
$X(3872)$ lineshape	20.0/32	0.95	0.194 ± 0.024	0.016 ± 0.004	0.020 ± 0.006	7.3σ	7.7σ
$\cos\theta_X < 0$	26.9/32	0.72	0.211 ± 0.035	0.019 ± 0.007	0.024 ± 0.010	*5.2σ*	*5.6σ*
$\cos\theta_X > 0$	42.2/32	0.11	0.217 ± 0.030	0.021 ± 0.006	0.027 ± 0.009	*4.2σ*	*6.7σ*
BDT selection	24.6/32	0.82	0.207 ± 0.022	0.018 ± 0.004	0.023 ± 0.006	7.9σ	8.4σ
cubic $\epsilon(m_{\pi\pi})$	24.5/32	0.83	0.221 ± 0.023	0.021 ± 0.005	0.027 ± 0.007	8.1σ	8.9σ
PIDcalib	24.6/32	0.82	0.214 ± 0.023	0.019 ± 0.004	0.025 ± 0.006	8.1σ	8.6σ
$\sigma(m_{\pi\pi}) \times 1.0$	26.6/32	0.74	0.213 ± 0.023	0.019 ± 0.004	0.025 ± 0.006	8.1σ	8.6σ
$\sigma(m_{\pi\pi}) \times 1.14$	22.6/32	0.89	0.215 ± 0.023	0.020 ± 0.004	0.026 ± 0.006	8.1σ	8.7σ
$[380, 775] MeV$	18.0/31	0.97	0.196 ± 0.024	0.016 ± 0.004	0.021 ± 0.006	7.1σ	7.5σ
GS model, ρ'	24.8/32	0.81	0.221 ± 0.024	0.021 ± 0.005	0.028 ± 0.007	7.8σ	7.2σ
Summary			$0.214 \pm 0.023 \pm 0.020$	$0.019 \pm 0.004 \pm 0.003$	$0.025 \pm 0.006 \pm 0.005$	$> 7.1\sigma$	

23 Conclusions

We have performed analysis of dipion mass distribution in $X(3872) \to \pi^+\pi^- J/\psi$ decays, reconstructed from $B^+ \to K^+ X(3872)$ decays, with the signal statistics which is 43 times larger than in the previous analysis of this type. The ρ^0 and ω contributions are resolved for the first time. The decay is dominated by $\rho^0 \to \pi^+\pi^-$ contribution, however this contribution alone fails to describe the data. We have developed a coupled-channel K-matrix model, which describes the data well once the ω contribution, coupling to both $\pi^+\pi^-$ and $\pi^+\pi^-\pi^0$ is allowed. The data can be equally well described with Gounaris-Sakurai model of ρ^0, coupling to ω, with a small ρ^0' contribution, previously used to describe the high statistics $e^-e^+ \to \pi^+\pi^-(\gamma)$ data [4]. We establish a $\omega \to \pi^+\pi^-$ contribution with a high significance ($> 7.1\sigma$) for the first time. At present, this is a more significant observation of $X(3872) \to \omega J/\psi$ decays, than the observations with $\omega \to \pi^+\pi^-\pi^0$ decays.

Quantitatively, the $\omega \to \pi^+\pi^-$ contribution leaves a large impact on the overall $X(3872) \to \pi^+\pi^- J/\psi$ rate, by contributing as much as $(21.4 \pm 2.3 \pm 2.0)\%$, mostly via interference with the ρ^0 contribution. Without this interference, the dominant ω term in our coupled-channel model constitutes only $(1.9 \pm 0.4 \pm 0.3)\%$ of the total rate, which is consistent with the expectations based on $X(3872) \to \omega J/\psi$, $\omega \to \pi^+\pi^-\pi^0$ rate measurements and the known ω branching fractions to channels with two and three pions.

By providing a detailed explanation of the dipion mass distribution observed in the $X(3872) \to \pi^+\pi^- J/\psi$ decays, we properly quantify magnitude of isospin violating production of ρ^0 resonance for the first time. Relative to the isospin conserving $\omega J/\psi$ decay, $\rho^0 J/\psi$ rate is an order of magnitude larger than expected for an ordinary charmonium state.

Large isopin violation is naturally expected in models in which the $X(3872)$ state has a significant component of $D\overline{D}^*$ pairs, either as constituents (molecular model) or generated dynamically in the decay, which would preferentially be $D^0\overline{D}^{*0}$ combination, thanks to the proximity of the $X(3872)$ mass to the related threshold, rather than D^+D^{*-} combination, which is 8 MeV heavier [27–30, 33, 35, 42–45]. However, it has been also suggested that two, degenerate and mixed, neutral, compact tetraquark states could also give a raise to a large isospin violation in the $X(3872)$ decays [46–48]. The compact tetraquark model predicts charged partners of $X(3872)$, which have not been observed.

Appendices

A Dipion mass distribution in the signal simulations

In this section we discuss in more detail the dipion mass distribution in the simulated sample of $B^+ \to X(3872)K^+$, $X(3872) \to J/\psi\rho^0$, $\rho^0 \to \pi^+\pi^-$, $J/\psi \to \mu^+\mu^-$ events. In particular, we cover reweighting of this sample with the dipion mass, applied when comparing the simulated sample to the real data in variables other than the dipion mass. We also present a test of the default matrix element model on this fully simulated sample.

The events were generated according to EventType 12145003, in which the B^+ decay chain is simulated using the helicity model in which 1^{++} $X(3872)$ decays in S-wave, which describes the angular distributions in the data well [3]. For convenience, we list here EvtGen dec-file directives:

```
Decay B+sig
1.000 MyX_1(3872) K+ HELAMP  1.0 0;
Enddecay
CDecay B-sig
#
Decay MyX_1(3872)
1.00000 MyJ/psi Myrho0 HELAMP 0.707107 0 0.707107 0 0.707107 0 0 0 -0.707107 0 -0.707107 0 -0.707107 0;
Enddecay
#
Decay MyJ/psi
1.000 mu+ mu- PHOTOS VLL;
Enddecay
#
Decay Myrho0
1.000 pi+ pi- VSS;
Enddecay
```

The comparison between the reconstructed dipion mass distributions in the data and in the MC is shown in Fig. 95. Both were obtained by fitting the $X(3872)$ peak in the $J/\psi\pi^+\pi^-$ mass distribution in bins of the dipion mass as described in Sec. 6. Since the MC has very little combinatoric background under the $X(3872)$ peak, and no contribution from $B^+ \to J/\psi K^{*+}$, $K^{*+} \to K^+\pi^+\pi^-$ which are significant in the data, the background polynomial is reduced to a constant term when fitting the MC. The distributions track each other rather well, except for the highest mass values. However, this is an accident, since the data contains the significant ω contribution, which accounts for about 20% of the total rate (after interference with the ρ^0) present mostly at high dipion masses. The

MC makes up for the lack of the ω contribution in the simulations by not implementing a proper phase-space factor in the $X(3872) \to J/\psi\rho^0$ decay. We discuss this further below. When projecting the simulations to other variables than the dipion mass, we correct for the deviations between the data and MC seen in Fig. 95, by weighting the simulated sample with the mass-dependent weight shown in Fig. 96.

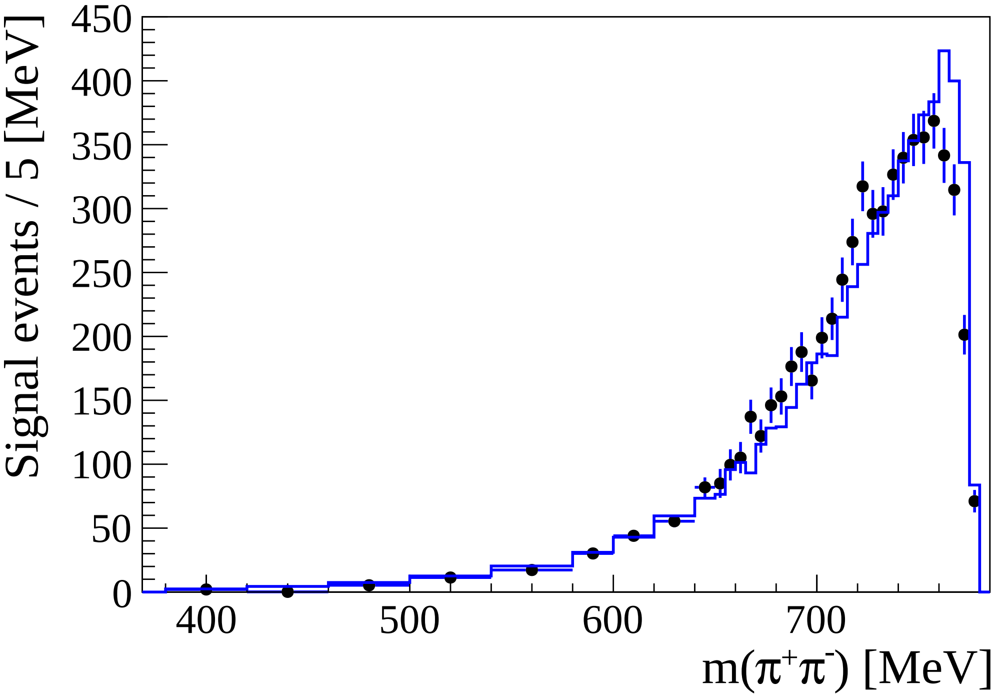

Figure 95: *The reconstructed dipion mass distributions in the data (points with the error bars) and in the MC (histogram). The MC signal sample is 6.3 times larger than in the data and was scaled down to the same integral as the data.*

An attempt to fit the dipion mass distribution in the MC with the ρ^0 contribution alone, exposes the problem in the generation of the proper ρ^0 shape in the MC generation, as illustrated in Fig. 97. The ρ^0 Breit-Wigner shape here is consistent with the ρ^0 shape documented in the previous publication on this topic by the Belle Collaboration [38], which rules out a possibility of a mistake in our formulae or coding. Therefore, the problem is on the MC generation side. In fact, the MC distribution observed here is consistent with the ρ^0 mass sampled from the ρ^0 Breit-Wigner formula and just truncated at the upper kinematic bound, without taking into account the phase-space factor, $p_{J/\psi}$, in the $X(3872) \to J/\psi\rho^0$ decay. The observed sharp drop off of the reconstructed dipion mass

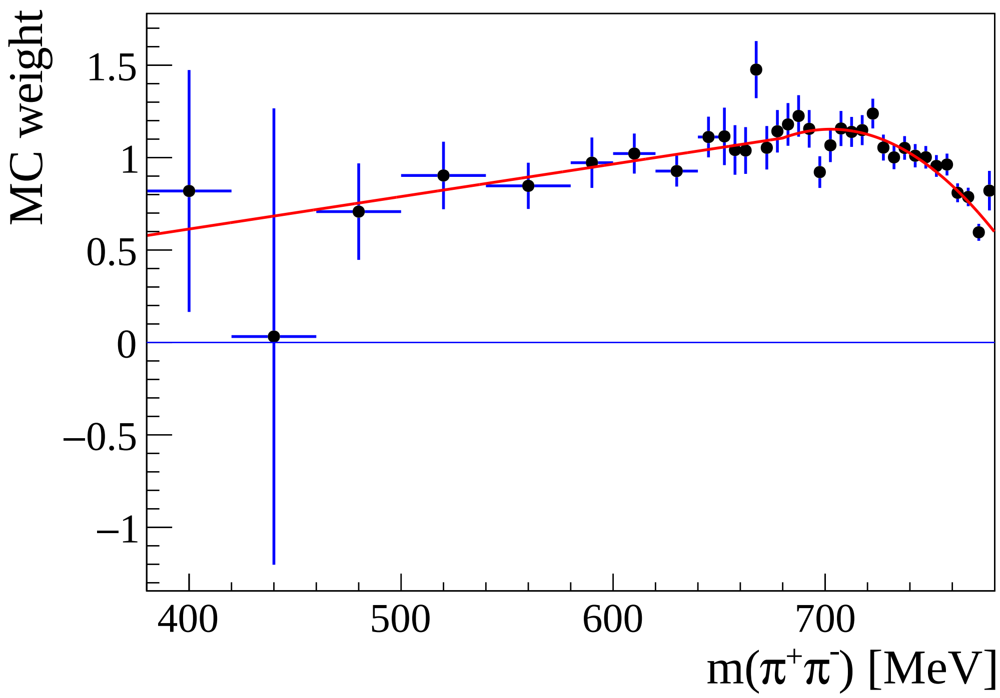

Figure 96: *The ratio of the dipion mass distribution reconstructed in the data and in the simulations (points with error bars), with the smoothing weight function superimposed. p-value of the fit is 47%.*

distribution in the MC near the upper kinematic bound is only due to the finite mass resolution.

To make up for improper ρ^0 mass generation in the MC, we reweight the simulated sample according to the $p_{J/\psi}(m)/p_{J/\psi}(700\,\text{MeV})$ weight, where m is the true dipion mass (from the MC "truth" information), and 700 MeV is an arbitrary weight-normalization point. After reweighting, we fit the simulated sample with our default K-matrix model, which allows for ρ^0, with a linear mass dependence of its production vector, and for ω contribution. The ρ^0 mass and width are fixed in the fit to the values used in the generation (768.5 MeV and 151 MeV, respectively). The mass resolution is not scaled up. It is not clear to us if EvtGen uses mass dependent width formula for ρ^0, and if so, what is the effective hadron size parameter (R) used in the Blatt-Weisskopf form-factor. It is not even clear if the Breit-Wigner used in the generation is in a non-relativistic or relativisitic form. Since it would be difficult to take relativity out of our K-matrix model, we stick to our default formulation and float the R value in the fit. The obtained value is $R = (5.8 \pm 1.5)\,\text{GeV}^{-1}$.

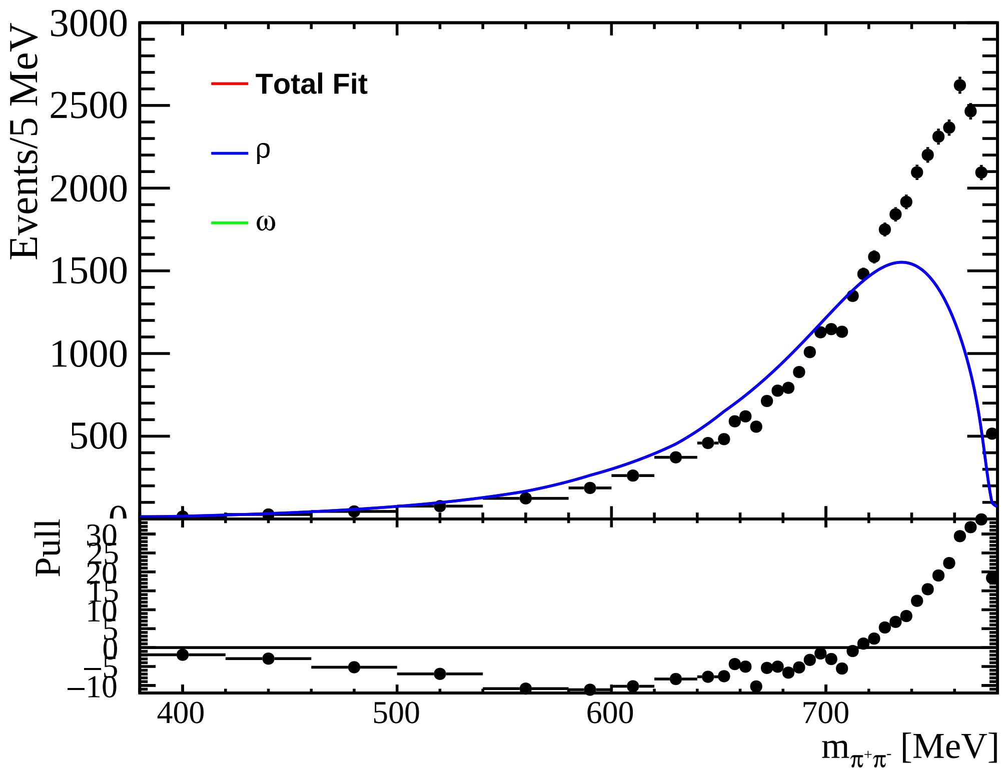

Figure 97: *The fit of ρ^0 Breit-Wigner shape to the dipion mass distribution reconstructed in the signal MC.*

The fit describes the reweighted simulations reasonably well as shown in Fig. 98. The obtained ω contribution is consistent with zero, $A_\omega = (0.002 \pm 0.018) \times ({m_\omega}^2 - {m_\rho}^2)$, $R^0_\omega = R^0_{\omega/\rho} = 0.0001 \pm 0.0002$ and $R^{all}_\omega = 0.002 \pm 0.018$. The ρ^0 production is consistent with no dependence on the dipion mass, $P_1 = 0.102 \pm 0.052$, as in fact expected for these simulations. This exercise validates our fitting approach and proves the lack of the $p_{J/\psi}$ phase-space factor in the ρ^0 shape generation in the simulations.

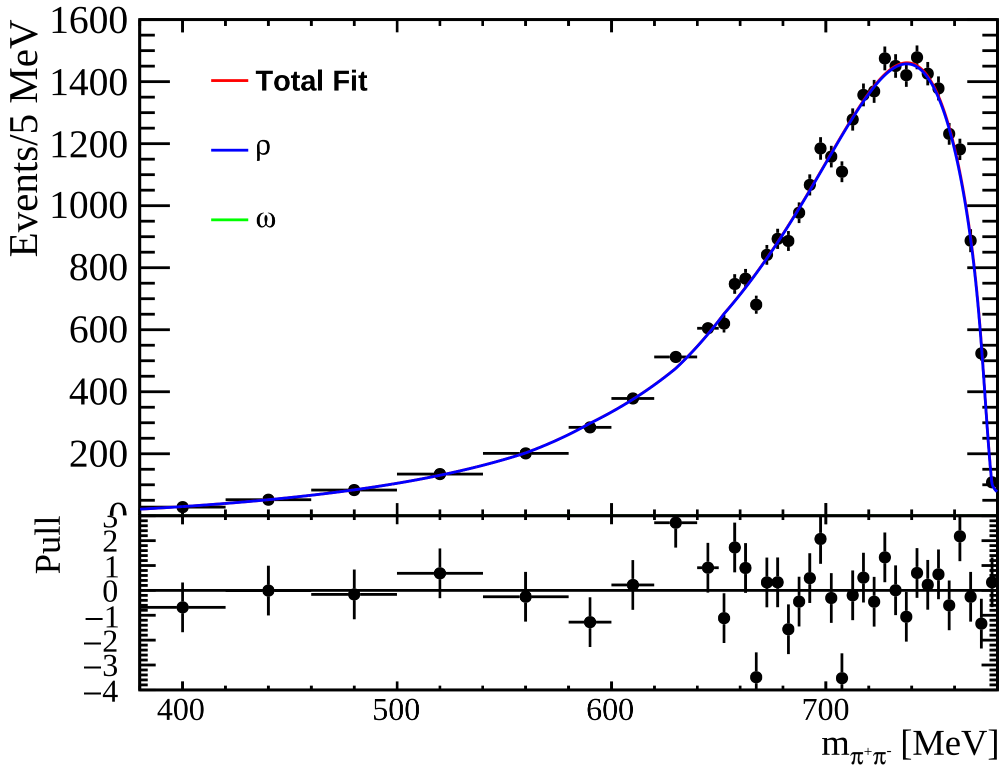

Figure 98: *The fit of ρ^0 and ω contributions to the dipion mass distribution reconstructed in the signal MC after reweighting MC with $p_{J/\psi}$, as described in the text.*

B Various additional plots and information

In this appendix we include various plots and information added on request, which do not fit other sections.

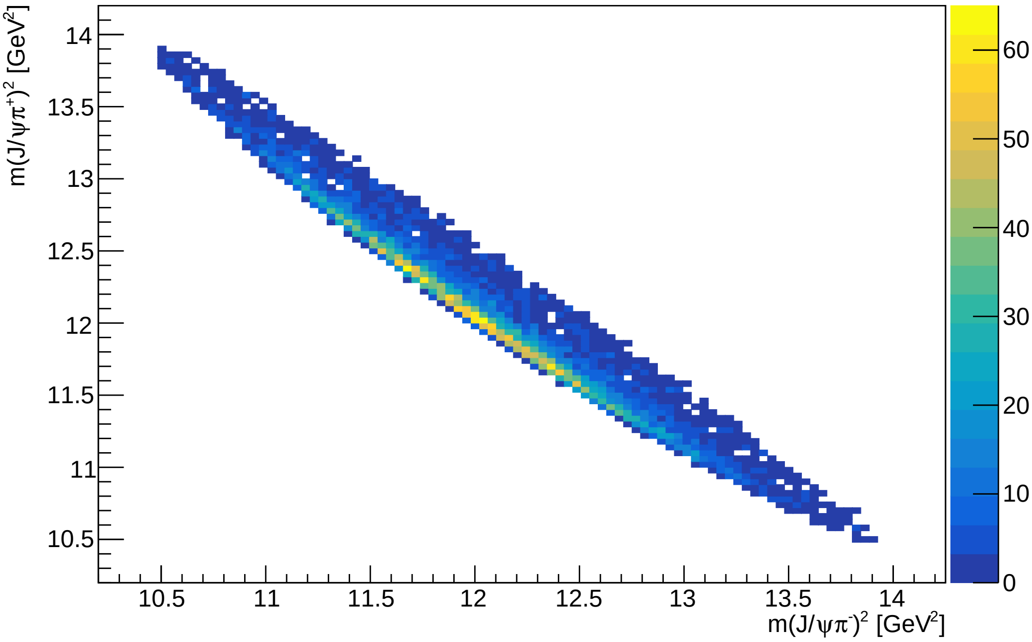

Figure 99: *Dalitz plot for $X(3872) \to J/\psi\pi^+\pi^-$ decay. The pion candidate which has the same sign as B in the selected $B \to X(3872)K$ decay is labeled as π^+.*

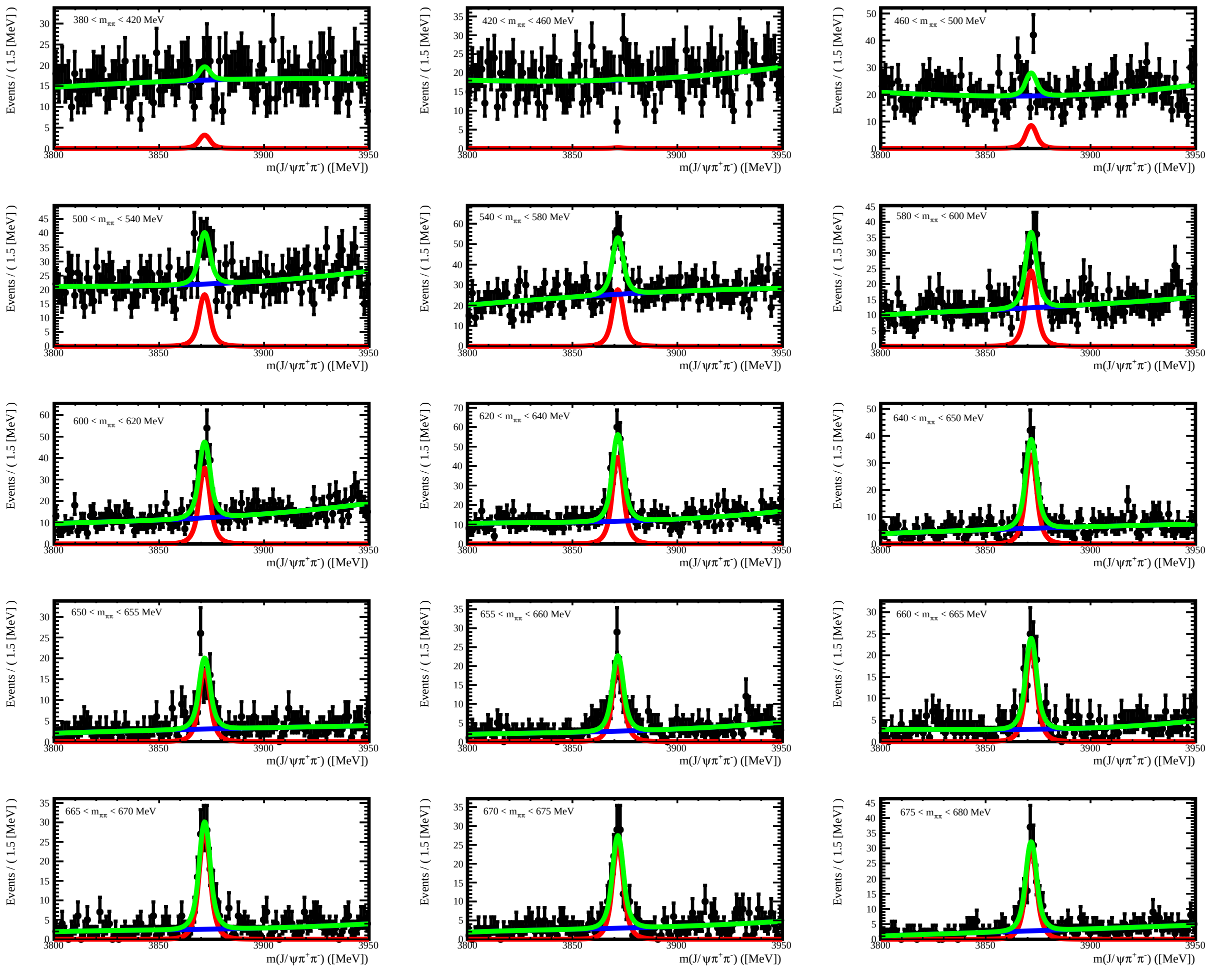

Figure 100: *Projections of unbinned fits to* $m_{J/\psi\pi\pi}$ *vs.* $m_{\pi\pi}$*, in different* $m_{\pi\pi}$ *bins, onto the* $m_{J/\psi\pi\pi}$ *axis. The total fit, the* $X(3872)$ *signal and the background components are shown by the green, red and blue lines, respectively.*

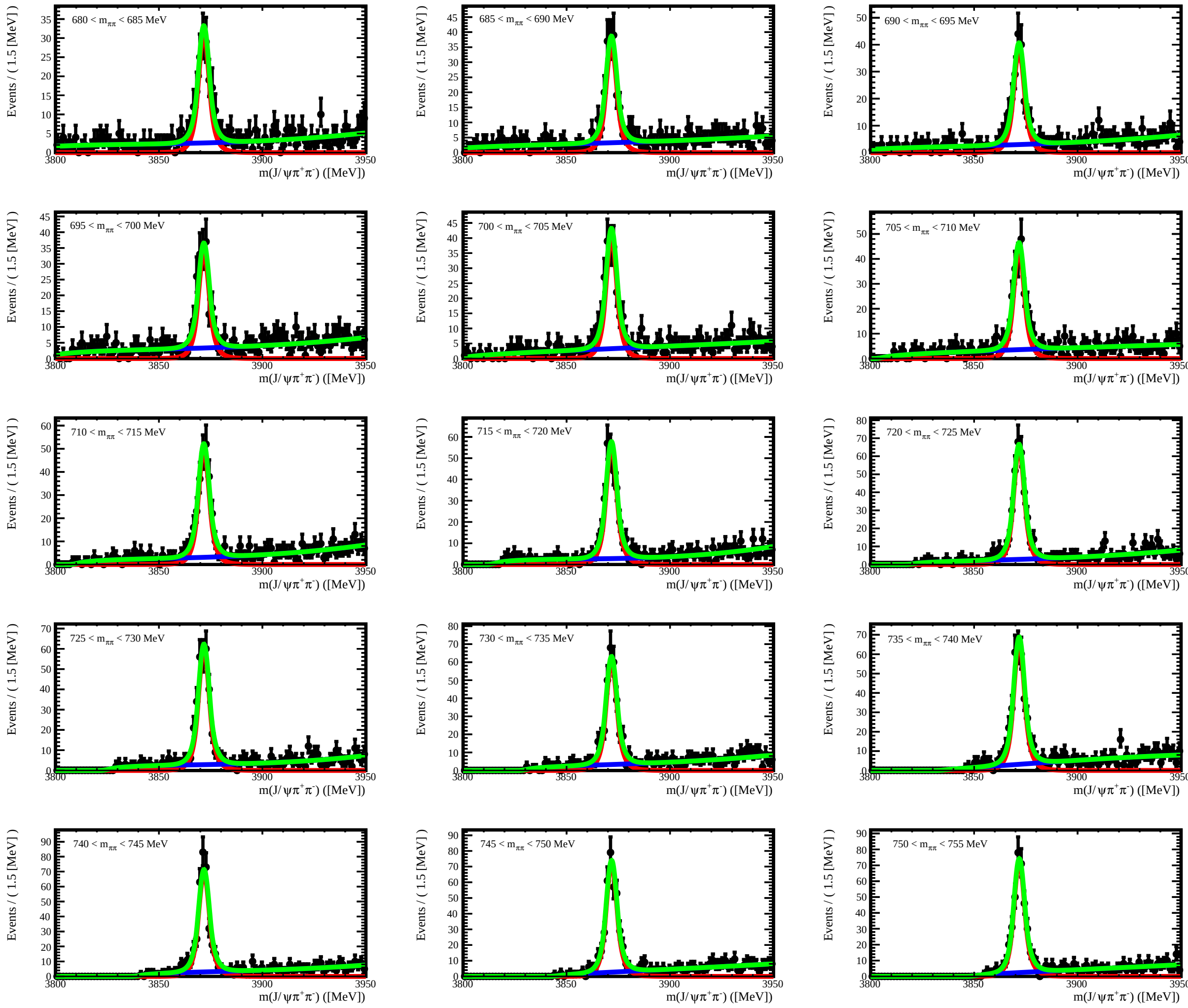

Figure 101: *Projections of unbinned fits to* $m_{J/\psi\pi\pi}$ *vs.* $m_{\pi\pi}$*, in different* $m_{\pi\pi}$ *bins, onto the* $m_{J/\psi\pi\pi}$ *axis. The total fit, the* $X(3872)$ *signal and the background components are shown by the green, red and blue lines, respectively.*

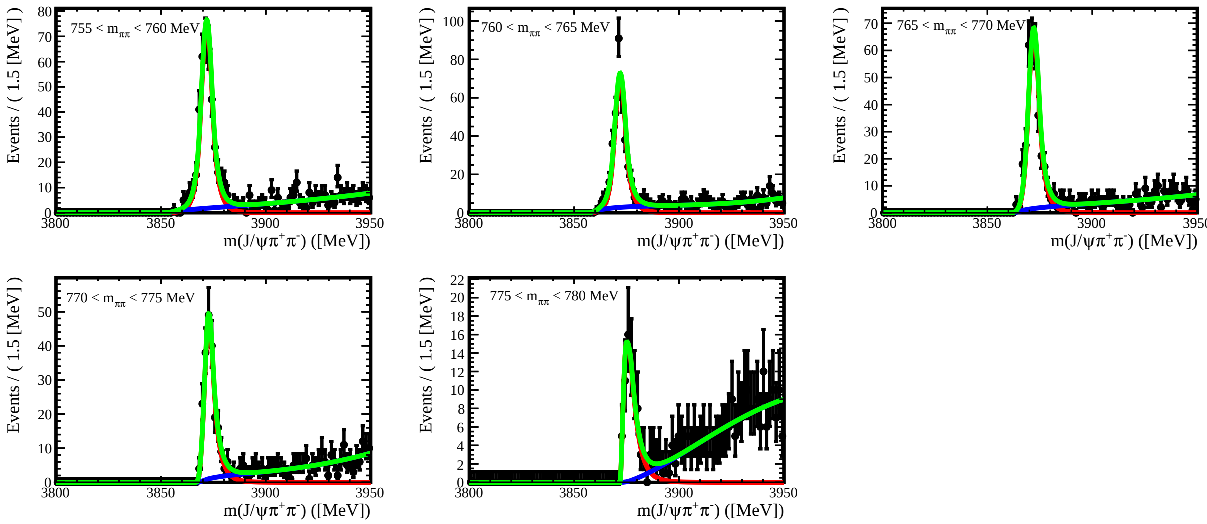

Figure 102: *Projections of unbinned fits to* $m_{J/\psi\pi\pi}$ *vs.* $m_{\pi\pi}$*, in different* $m_{\pi\pi}$ *bins, onto the* $m_{J/\psi\pi\pi}$ *axis. The total fit, the* $X(3872)$ *signal and the background components are shown by the green, red and blue lines, respectively.*

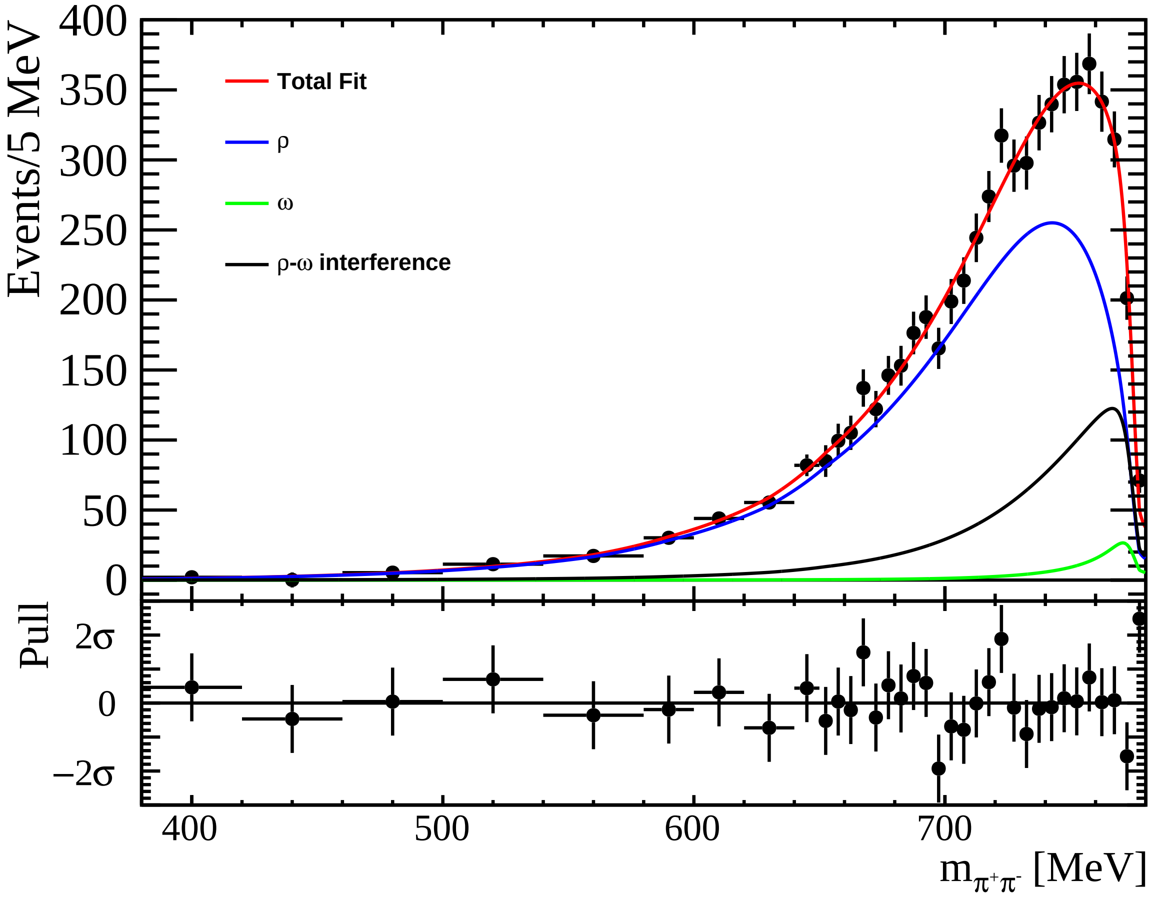

Figure 103: *The default fit as in Fig. 52 (the coupled-channel model with the ρ^0 and ω contributions and linear dependence of $\alpha_{2\pi}$ on $m^2_{\pi\pi}$) in which, in addition to ρ^0 and ω fit components, we also show their interference (the black line).*

Table 10: *Values of all parameters, floated (fit errors given) and fixed (no errors), used in the default fit. The efficiency parameterization given in the caption of Fig. 43 also enters the fit.*

Parameter	Value
S (Eq. 4)	$(269.6 \pm 9.7) \times 10^5$
$A/(m_\omega^2 - m_\rho^2)$ (Eq. 31)	0.208 ± 0.024
P_1 (Eq. 25)	0.226 ± 0.045
P_0 (Eq. 25)	1 (normalization conventions for S, A, and P_n)
$m_{X(3872)}$	3871.69 MeV
$m_{J/\psi}$	3096.92 MeV
m_π	139.57 MeV
m_ρ	775.26 MeV
Γ_ρ	147.4 MeV
m_ω	782.66 MeV
Γ_ω	8.68 MeV
$\mathcal{B}(\omega \to \pi^+\pi^-)$ (Eq. 23)	0.0153
$\mathcal{B}(\omega \to 3\pi)$ (Eq. 22)	0.892
R $(= R_{prod})$ (Eq. 8)	$1.45\,\mathrm{GeV}^{-1}$
Scale factor to Eq. 3	1.06

References

[1] R. García-Martín *et al.*, *Pion-pion scattering amplitude. IV. Improved analysis with once subtracted Roy-like equations up to 1100 MeV*, Physical Review D **83** (2011) , arXiv:1102.2183.

[2] G. J. Gounaris and J. J. Sakurai, *Finite width corrections to the vector meson dominance prediction for $\rho \to e^+e^-$*, Phys. Rev. Lett. **21** (1968) 244.

[3] LHCb collaboration, R. Aaij *et al.*, *Quantum numbers of the $X(3872)$ state and orbital angular momentum in its $\rho^0 J/\psi$ decays*, Phys. Rev. **D92** (2015) 011102(R), arXiv:1504.06339.

[4] BaBar, J. P. Lees *et al.*, *Precise Measurement of the $e^+e^- \to \pi^+\pi^-(\gamma)$ Cross Section with the Initial-State Radiation Method at BABAR*, Phys. Rev. D **86** (2012) 032013, arXiv:1205.2228.

[5] ATLAS, G. Aad *et al.*, *Observation of a new particle in the search for the Standard Model Higgs boson with the ATLAS detector at the LHC*, Phys. Lett. B **716** (2012) 1, arXiv:1207.7214.

[6] CMS, S. Chatrchyan *et al.*, *Observation of a New Boson at a Mass of 125 GeV with the CMS Experiment at the LHC*, Phys. Lett. B **716** (2012) 30, arXiv:1207.7235.

[7] Belle Collaboration, S. K. Choi *et al.*, *Observation of a Narrow Charmoniumlike State in Exclusive $B^\pm \to K^\pm\pi^+\pi^- J/\psi$ Decays*, Phys. Rev. Lett. **91** (2003) 262001.

[8] LHCb Collaboration, R. "Aaij and others", *Determination of the $x(3872)$ meson quantum numbers*, Phys. Rev. Lett. **110** (2013) 222001.

[9] L. Maiani, F. Piccinini, A. D. Polosa, and V. Riquer, *Diquark-antidiquark states with hidden or open charm and the nature of $x(3872)$*, Phys. Rev. D **71** (2005) 014028.

[10] Belle, S.-K. Choi *et al.*, *Bounds on the width, mass difference and other properties of $X(3872) \to \pi^+\pi^- J/\psi$ decays*, Phys. Rev. D **84** (2011) 052004, arXiv:1107.0163.

[11] BaBar, B. Aubert *et al.*, *Study of Resonances in Exclusive B Decays to anti-D(*) D(*) K*, Phys. Rev. D **77** (2008) 011102, arXiv:0708.1565.

[12] Belle Collaboration, T. Aushev and other. *Study of the* $b \to x(3872)(\to D^{*0}\overline{d}^{0})k$ *decay*, Phys. Rev. D **81** (2010) 031103.

[13] LHCb, A. A. Alves, Jr. *et al.*, *The LHCb Detector at the LHC*, JINST **3** (2008) S08005.

[14] Particle Data Group, J. Beringer *et al.*, *Review of Particle Physics (RPP)*, Phys. Rev. D **86** (2012) 010001.

[15] LHCb RICH Group, M. Adinolfi *et al.*, *Performance of the LHCb RICH detector at the LHC*, Eur. Phys. J. C **73** (2013) 2431, `arXiv:1211.6759`.

[16] LHCb, A. A. Alves, Jr. *et al.*, *The LHCb Detector at the LHC*, JINST **3** (2008) S08005.

[17] A. Arefev *et al.*, *Beam Test Results of the LHCb Electromagnetic Calorimeter.*, , CERN, Geneva, 2008. revised version submitted on 2008-05-15 09:09:53.

[18] CDF II Collaboration, D. "Acosta and others", *Observation of the Narrow State* $X(3872) \to J/\psi\pi^+\pi^-$ *in* $\overline{p}p$ *Collisions at* $\sqrt{s} = 1.96$ TeV, Phys. Rev. Lett. **93** (2004) 072001.

[19] D0 Collaboration, V. M. "Abazov and others", *Observation and Properties of the* $X(3872)$ *Decaying to* $J/\psi\pi^+\pi^-$ *in* $p\overline{p}$ *Collisions at* $\sqrt{s} = 1.96$ TeV, Phys. Rev. Lett. **93** (2004) 162002.

[20] BABAR Collaboration, B. "Aubert and others", *Study of the* $B^- \to J/\psi K^-\pi^+\pi^-$ *decay and measurement of the* $B^- \to X(3872)K^-$ *branching fraction*, Phys. Rev. D **71** (2005) 071103.

[21] LHCb collaboration, R. Aaij *et al.*, *Determination of the* $X(3872)$ *meson quantum numbers*, Phys. Rev. Lett. **110** (2013) 222001, `arXiv:1302.6269`.

[22] Particle Data Group, P. A. Zyla *et al.*, *Review of Particle Physics*, Progress of Theoretical and Experimental Physics **2020** (2020) , `arXiv:https://academic.oup.com/ptep/article-pdf/2020/8/083C01/33653179/ptaa104.pdf` 083C01.

[23] Belle, K. Abe *et al.*, *Evidence for $X(3872) \to \gamma J/\psi$ and the sub-threshold decay $X(3872) \to \omega J/\psi$,* in *Lepton and photon interactions at high energies. Proceedings, 22nd International Symposium, LP 2005, Uppsala, Sweden, June 30-July 5, 2005*, 2005, arXiv:hep-ex/0505037.

[24] BaBar, P. del Amo Sanchez *et al.*, *Evidence for the decay $X(3872) \to J/\psi\omega$*, Phys. Rev. **D82** (2010) 011101, arXiv:1005.5190.

[25] BESIII, M. Ablikim *et al.*, *Study of $e^+e^- \to \gamma\omega J/\psi$ and Observation of $X(3872) \to \omega J/\psi$*, Phys. Rev. Lett. **122** (2019) 232002, arXiv:1903.04695.

[26] E. Braaten and M. Kusunoki, *Decays of the X(3872) into J/psi and light hadrons*, Phys. Rev. D **72** (2005) 054022, arXiv:hep-ph/0507163.

[27] N. A. Tornqvist, *Comment on the narrow charmonium state of Belle at 3871.8-MeV as a deuson*, arXiv:hep-ph/0308277.

[28] N. A. Tornqvist, *Isospin breaking of the narrow charmonium state of Belle at 3872-MeV as a deuson*, Phys. Lett. B **590** (2004) 209, arXiv:hep-ph/0402237.

[29] E. S. Swanson, *Short range structure in the X(3872)*, Phys. Lett. B **588** (2004) 189, arXiv:hep-ph/0311229.

[30] M. Suzuki, *The X(3872) boson: Molecule or charmonium*, Phys. Rev. D **72** (2005) 114013, arXiv:hep-ph/0508258.

[31] K. Terasaki, *$\omega - \rho^0$ mixing as a possible origin of the hypothetical isospin non-conservation in the $X(3872) - -- > \pi^+\pi^- J/\psi$ decay*, Prog. Theor. Phys. **122** (2010) 1285, arXiv:0904.3368.

[32] M. Takizawa and S. Takeuchi, *Structure of the X(3872) and its isospin symmetry breaking*, EPJ Web Conf. **3** (2010) 03026.

[33] S. Coito, G. Rupp, and E. van Beveren, *Delicate interplay between the $D^0 D^{*0}$, $\rho^0 J/\psi$, and $\omega J/\psi$ channels in the $X(3872)$ resonance*, Eur. Phys. J. C **71** (2011) 1762, arXiv:1008.5100.

[34] C. Hanhart, Y. S. Kalashnikova, A. E. Kudryavtsev, and A. V. Nefediev, *Remarks on the quantum numbers of X(3872) from the invariant mass distributions of the rho J/ψ and omega J/ψ final states*, Phys. Rev. D **85** (2012) 011501, `arXiv:1111.6241`.

[35] N. Li and S.-L. Zhu, *Isospin breaking, Coupled-channel effects and Diagnosis of X(3872)*, Phys. Rev. D **86** (2012) 074022, `arXiv:1207.3954`.

[36] Z.-Y. Zhou and Z. Xiao, *Comprehending Isospin breaking effects of* $X(3872)$ *in a Friedrichs-model-like scheme*, Phys. Rev. D **97** (2018) 034011, `arXiv:1711.01930`.

[37] CDF Collaboration, A. "Abulencia and others", *Measurement of the Dipion Mass Spectrum in* $X(3872) \to J/\psi\pi^+\pi^-$ *Decays*, Phys. Rev. Lett. **96** (2006) 102002.

[38] Belle, S.-K. Choi *et al.*, *Bounds on the width, mass difference and other properties of* $X(3872) \to \pi^+\pi^- J/\psi$ *decays*, Phys. Rev. D **84** (2011) 052004, `arXiv:1107.0163`.

[39] LHCb collaboration, R. Aaij *et al.*, *Measurement of the b-quark production cross-section in 7 and 13 TeV pp collisions*, Phys. Rev. Lett. **118** (2017) 052002, Erratum ibid. **119** (2017) 169901, `arXiv:1612.05140`.

[40] S. S. Wilks, *The large-sample distribution of the likelihood ratio for testing composite hypotheses*, Ann. Math. Stat. **9** (1938) 60.

[41] LHCb collaboration, R. Aaij *et al.*, *Study of the line shape of the* $\chi_c(3872)$ *state*, Phys. Rev. **D102** (2020) 092005, `arXiv:2005.13419`.

[42] M. B. Voloshin, *Interference and binding effects in decays of possible molecular component of* $X(3872)$, Phys. Lett. B **579** (2004) 316, `arXiv:hep-ph/0309307`.

[43] S. Takeuchi, K. Shimizu, and M. Takizawa, *On the origin of the narrow peak and the isospin symmetry breaking of the X(3872)*, PTEP **2014** (2014) 123D01, `arXiv:1408.0973`, [Erratum: PTEP 2015, 079203 (2015)].

[44] Q. Wu, D.-Y. Chen, and T. Matsuki, *A phenomenological analysis on isospin-violating decay of* $X(3872)$, Eur. Phys. J. C **81** (2021) 193, `arXiv:2102.08637`.

[45] L. Meng, G.-J. Wang, B. Wang, and S.-L. Zhu, *Revisit the isospin violating decays of* $X(3872)$, `arXiv:2109.01333`.

[46] K. Terasaki, *A New tetra-quark interpretation of X(3872)*, Prog. Theor. Phys. **118** (2007) 821, arXiv:0706.3944.

[47] L. Maiani, A. D. Polosa, and V. Riquer, *A Theory of X and Z Multiquark Resonances*, Phys. Lett. B **778** (2018) 247, arXiv:1712.05296.

[48] L. Maiani, A. D. Polosa, and V. Riquer, $X(3872)$ *tetraquarks in* B *and* B_s *decays*, Phys. Rev. D **102** (2020) 034017, arXiv:2005.08764.

Vita

Author's Name: Baasansuren Batsukh

Place of Birth: Ulaanbaatar, Mongolia

Date of Birth: January 22, 1994

Degrees Awarded:

Bachelor of Science, National University of Mongolia, 2015

Professional Experience:

Teaching Assistant, Syracuse University Department of Physics, 2015-2017

Research Assistant, Syracuse University Department of Physics, 2017-2021

CERN User, Geneva, Switzerland, since 2017